ABSTRACT

Title of Thesis: Evaluation of Flexible Rotor Hover Performance in Extreme Ground Effect

Degree Candidate: Mor Gilad, Master of Science, 2011

Degree and Year: Master of Science, 2011

Thesis directed by: Professor Inderjit Chopra
and
Visiting Professor Omri Rand
Department of Aerospace Engineering

Motivated by the Sikorsky Human Powered Helicopter Challenge, an attempt to further study ground influence on a hovering rotor of highly elastic blades in extreme ground proximity has been carried out. This study presents two computational approaches for prediction of elastic blade behavior in ground effect, using finite element analysis (FEM) for deflections while modeling ground effect on a blade element level.The first approach is based on classical blade element momentum theory, correcting for ground effect based on empirical models.The second method uses a newly tailored rigid prescribed wake model alongside blade element analysis. As both methods account for local height off the ground at each blade element, they allow for more detailed insight regarding property distributions along the highly elastic blade in extreme ground effect conditions and thus improved performance prediction capabilities. This study includes experimental results from both a rigid blade sub-scale set-up and elastic blade full scale set-up, operating in extreme ground

effect, which are subsequently used to validate the proposed methods. This work concludes that careful consideration of blade deflections when modeling flexible rotor performance in extreme ground effect is key to a successful prediction capability, and thus design parameters which influence variation in thrust distribution will have an increased effect on performance in these conditions.

Evaluation of Flexible Rotor Hover Performance in Extreme Ground Effect

by

Mor Gilad

Thesis submitted to the Department of Aerospace Engineering
University of Maryland, College Park in partial fulfillment
of the requirements for the degree of
Master of Science
2011

Advisory Committee:
Professor Inderjit Chopra, Chair/Advisor
Visiting Professor Omri Rand, Advisor
Professor James D. Baeder
Assistant Professor Anya R. Jones

© Copyright by
Mor Gilad
2011

Dedication

This dissertation is dedicated to Chen Friedman. My rock.

Acknowledgments

This work would not been conceptually conceived had it not been for the University of Maryland Alfred Gessow rotorcraft center picking up the immense challenge of the Sikorsky Human Powered Helicopter prize. I would like to extend my gratitude to Dr. Darryl Pines and Dr. Inderjit Chopra for initiating this project, allowing us all to dream. I am also grateful for the opportunity to work with the HPH student research team, a team of creative, caring and invested engineers, unafraid to chase what has been deemed "impossible" - with out them the project would have remained solely an idea, and this work would not have come to life. I would especially like to thank the following team members, past and present: Joseph Schmaus, Tyler Fean, and Christopher McDermott, for their efforts in acquiring the experimental data presented in this work, Ben Berry for taking the product of this work to further levels I did not have the time to explore, and Graham Bowen-Davies for his honest friendship and constant soothing presence, and finally Brandon Bush - my partner in crime, for his always optimistic friendly smile and lending shoulder.

I would like to further extend my gratitude to Dr. Chopra for being my graduate advisor and the opportunity to join the Masters program at the University of Maryland, and Dr. Omri Rand from the Technion in Israel, for his valuable advice throughout the progress of my research.

Also, I would like to thank my family at home for their love, support, and always attentive ears, which although geographically distant always seemed close to heart.

And last, but not least, I am especially grateful to Chen Friedman, my love, best friend, and partner in this life's journey - for his patience, encouragement, endless support, and blazing fast page flipping skills. You inspire me to be a better me. I could have, and would have, never done this without you. Thank you.

Table of Contents

List of Figures

Nomenclature

$\tilde{(\ )}$	Property non-dimensionalized by R
$\bar{(\ )}$	Vector property
A	Rotor disk area, πR^2
c	Rotor blade chord
C_d	Section drag coefficient, $D/(\frac{1}{2}\rho U^2 c)$
C_l	Section lift coefficient, $L/(\frac{1}{2}\rho U^2 c)$
C_m	Section pitching moment coefficient, $M/(\frac{1}{2}\rho U^2 c)$
C_P	Rotor power coefficient, $P/(\rho A \Omega^3 R^3)$
C_Q	Rotor torque coefficient, $Q/(\rho A \Omega^3 R^2)$
C_T	Rotor thrust coefficient, $T//(\rho A \Omega^2 R^2)$
L	Lift of a blade element
N_b	Number of blades
N_e	Number of blade elements
N_{rev}	Number of far wake rotor revolutions
P	Dimensional power
r_c	Vortex core radius
$\tilde{r}$	Dimensionless radial coordinate along blade, r/R
$\tilde{r}_{tip}$	Tip vortex non-dimensional radial coordinate, r_{tip}/R
R	Rotor radius
T	Dimensional thrust
W	Helicopter weight
Z	Height above ground
Z/R	Non-dimensional height above ground
$\tilde{z}_{tip}$	Tip vortex non-dimensional axial coordinate, z_{tip}/R

Greek symbols

α	Effective Angle of attack
ϕ	Induced Angle of attack
Γ	2D Circulation per unit length
Γ_{tip}	Tip vortex strength (circulation)
λ	Non-dimensional inflow velocity
μ	Flow viscosity
ν	Kinematic viscosity coefficient, μ/ρ
ψ	Blade azimuthal angle
ψ_w	Wake age
ρ	Flow density
σ	Rotor solidity, $N_b c/(\pi R)$
θ	Collective pitch angle
θ_{tw}	Linear blade twist
Ω	Rotor rotational speed

Abbreviations

FW	Far Wake
HPH	Human Powered Helicopter
IGE	In Ground Effect
NW	Near Wake
OGE	Out of Ground Effect
RPM	Round Per Minute
TPP	Tip Path Plane

Chapter 1

Introduction

1.1 Motivation - The Human Powered Helicopter

The earliest and most famous design for a human powered vertical flight machine is found in late fifteenth century sketches of the Italian Renaissance polymath Leonardo da Vinci. The "Aerial Screw" machine shown in Fig. 1.1, though centuries ahead of it's time, demonstrated what is still the biggest hurdle in human powered hover - transmission of enough human power to create sufficient lift.

In 1980 the American Helicopter Society created the Igor I. Sikorsky Human Powered Helicopter competition, challenging the rotorcraft community to design, build, and fly a human powered helicopter. The competition requires hovering for at least 60 seconds, momentarily reaching a height of 3 meters, while remaining within a control area of 10 $m \times 10$ m [8]. This challenge is considered to be extremely difficult, as the human "pilot" must output enough power to allow the rotor to lift the weight of both the structure and his/her body. This requirement has been shown to lie on the verge of olympic athlete capability limits, and thus requires the designed vehicle to be highly efficient [1, 9] .

Since the creation of the competition, there have been over 20 attempts at this challenge by various teams around the globe. Although the challenge has yet to be met, as of 2010 official records, only two projects have succeeded in lifting off

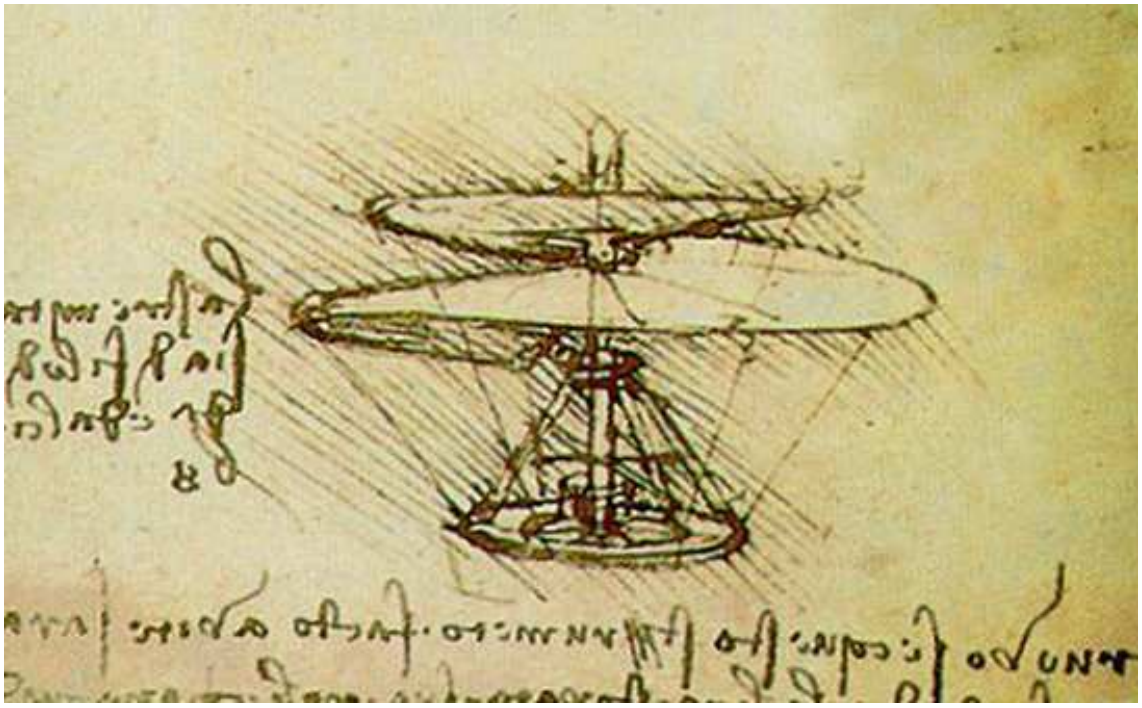

Figure 1.1: Leonardo da Vinci's Aerial Screw machine, dated to 1438

the ground under official witnessing. The first successful hover was achieved by the Cal-Poly State University's "Da Vinci III" [10] setting the record at 8 seconds¡ This record was raised to 19.4 seconds by Nihon University's "Yuri I", designed and built in Japan [11].

In 2009, the Alfred Gessow Rotorcraft Center began to vigorously pursue the Sikorsky Human Power Helicopter (HPH) challenge, and has since developed a quad-rotor system for this task. Each one of the 4 rotors consists of two blades, which are required to be as lightweight as possible while still providing the required lift. In order to minimize required power, a relatively large rotor radius is desirable, and as a result the long yet light-weight blades turn out to be extremely flexible.

Required to operate under the strict constraints of limited available human

power, the key to this challenge lies in reducing the power requirement to a minimum. Hovering close to the ground has been known to be beneficial for increased power loading, improving the effective lift capabilities of a rotor for a given power, or decreasing power requirements for a given thrust. The ground effect phenomena amplifies as the rotor approaches the ground, therefore, the HPH rotors are intended for operation as close to the ground as possible in an attempt to maximize ground effect benefits.

As in for all helicopters, the efficiency of this vehicle will be highly effected by it's weight, it's aerodynamic capabilities, and the effective transmission of power, in this case originating from the 'human engine'. This work will concentrate on studying the aerodynamic characteristics of such a rotor near the ground.

1.2 Hover Performance Prediction Methods

Understanding rotor performance relies on understanding the aerodynamic environment in which said rotor operates alongside its dynamic structural response to the resulting aerodynamic loads [1]. Due to the HPH challenge requirements, this work will concentrate on hovering rotor performance.

In hover, the rotor is not moving forward, nor is it in climb or descent. The purpose of the rotor in a hovering rotorcraft is to generate a steady upward vertical lifting force, equal in magnitude to the vehicle's weight (W) to overcome gravity, keeping the rotorcraft at a constant position. In this flight regime, the rotor flow field is generally considered as azimuthally axisymmetric (although wake methods do

portray some periodicity), passing through the rotor disk in a downwards direction, creating below it what is referred to as the rotor wake.

Analysis and prediction of the rotor behavior in this flight regime, lies in describing the physical flow about the rotor using a mathematical model and determining the induced flow velocity through the rotor. As computational capabilities developed throughout the 20^{th} century, the demand for more accurate predictions of helicopter performance increased, driving wake prediction models to evolve from the earliest, relatively simple, one dimensional momentum theory into the highly complex, computationally demanding, free-vortex wake models of today.

1.2.1 Momentum Theory Methods

Momentum theory models the rotor flow field problem via application of three basic conservation laws of fluid mechanics: mass, momentum, and energy. This method was originally proposed by Rankine in 1865 [12] for the analysis of marine propellers, further developed by Froude [13] and Betz [14, 15, 16], and formally generalized by Glauert in 1935 [17].

1.2.1.1 Actuator Disk Theory

The simplest mathematical model of a rotor is derived by replacing it with an actuator disk. The rotor is approximated by an infinitesimally thin disk, over which pressure differences exist, producing an instantaneous change in the momentum of the flow. Application of fluid conservation laws on a control volume surrounding

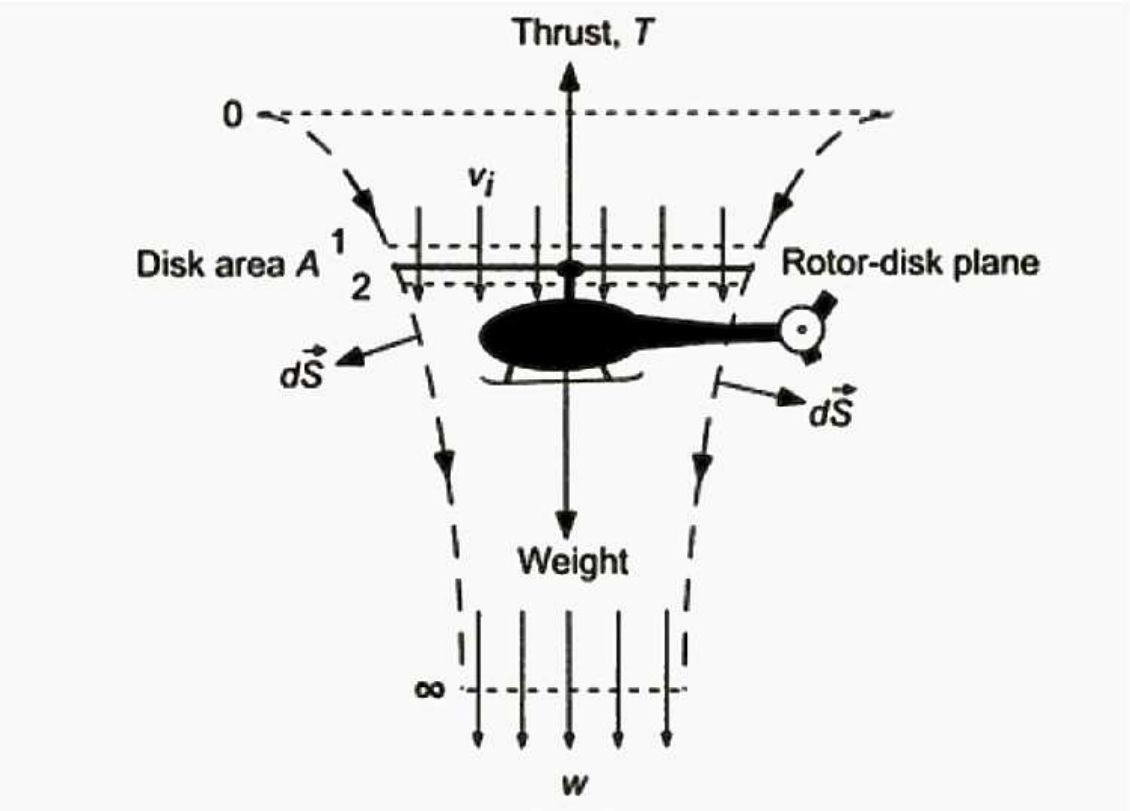

Figure 1.2: Flow Model for momentum theory analysis of a rotor in hovering flight, taken from Leishman [1].

the thrust carrying disk and it's wake, as illustrated in Fig. 1.2 from [1], results in a solution for the uniform induced velocity at the uniformly loaded rotor disk.

This early one-dimensional method does not account for details in rotor geometry, load distributions, and non-linearities in the flow environment (such as tip losses), and thus provides only a first order global estimation of the rotor thrust and power. Its principles do, however, provide an important foundation for a more elaborate approach to rotor aerodynamics.

1.2.1.2 Blade Element Momentum Theory

Blade Element Theory (BET), first proposed by Drzewiecki in 1892 [18, 19] for the analysis of airplane propellers, is also known as a Strip Theory. This method divides the blade into elements (strips) in the radial direction, assuming each to act as a two-dimensional airfoil, producing aerodynamic forces and moments. The wake influence on the rotor, and resulting non-uniform induced velocity distribution, is accounted for via an induced component of the angle of attack at each element [3]. Given a calculation of the wake induced velocities at the rotor, this method can be used to obtain performance predictions by integrating contributions from all elements along the blade radius.

Linking the induced velocity solution from momentum theory with the BET formulation was explored by Reissner [20, 21, 22], de Bothezat [23], and Glauert [17] in the early 20^{th} century, assuming a uniform inflow distribution over the rotor disk.

The combined **Blade Element Momentum Theory** (BEMT) was later proposed for helicopter analysis in 1946-1948 by Gustafson and Gessow [24] and Gessow [25], allowing for non-uniform inflow distributions along the rotor radius (a much more realistic solution). Similarly to the strip theory, BEMT divides the rotor disk into a finite number of annuli along the radial coordinate, applying momentum theory principles (conservation laws) at each annulus. Thus, a solution for induced velocity distribution can be obtained, under the two-dimensional assumption that the blade elements, or rather rotor annuli, do not interact with each other. Assuming 2-D behavior limits the method from capturing more complex 3-D effects such as

tip losses, swirl effects, and compressible effects. However, those can be corrected for using semi-empirical means [1].

Blade element momentum theory provides a good basic analytical tool for examination of rotor design parameters. This method is widely adopted in the aerospace, wind energy and maritime communities, for primary rotor performance analysis (such as by Tangler and Kocurek [26], Crawford [27], and Tenguria et al. [28]), design applications (such as by Bohorquez, Pines and Samuel [29]), and as basis for corrected methodologies using further enhancements and modifications (such as by Madsen [30] and Masters et al. [31]).

The blade element momentum theory provides a fast, accurate, convenient means of predicting global performance for initial design studies. It does not, however, model the rotor wake in detail, deeming it insufficient for studies of more complex flight conditions.

1.2.2 Vortex Wake Methods

The wake of a hovering rotor, illustrated in Fig. 1.3 by Gray [2] for a single blade, is comprised of two main flow components. The first component is the shear layer, shed from the inboard section of the blade, formed by merging of the boundary layers from the upper and lower blade surfaces [1]. This feature is often referred to as a vortex sheet. The second and most dominant component is created as shed vorticity from the blade rolls up into a discrete, concentrated tip vortex trailing from the tip of the blade [32]. Both the vortex sheet and the tip vortex are convected

below the rotor disk in a contracting helical trajectory, combining the rotational motion of the blades and the axial velocity of the flow through the rotor disk.

The wake of a hovering rotor, prominently the tip vortices, remains close to the rotor, inducing local variations in the airflow about the blades, and interacting with themselves as the downstream wake evolves. Constant influence of shed vorticity produces a complex induced velocity field that has a primary influence on blade loads and performance capabilities. Therefore, careful modeling of the rotor wake allows for more detailed predictive capabilities, providing a solution that is influenced by wake contraction, 3-D effects, and interaction between wake components.

The complex nature of the hovering helicopter wake, and its sensitivity to changes in blade geometry as well as operational environment, makes studying this intricate vortical flow a complicated task, both experimentally and computationally (by means of mathematical models). Leishman and Bagai [33] described and summarized the unique challenges involved with experimental studies of helicopter rotor wakes, while giving an overview of flow visualization methods used to measure rotor wakes. A review of rotor wake modeling capabilities is given by Landgrebe in 1988 [34], followed by McCroskey in 1995 [35], demonstrating the development over the past decades of higher level computational methods for aerodynamic analysis. The reviewed methods evolved into the advanced vortex methods available today, which allow more detailed studies as computational capabilities increase considerably over time.

Vortex Theory is a rotor analysis approach that calculates the flow field of the rotor wake, using a wake model representation of the vorticity shed from the

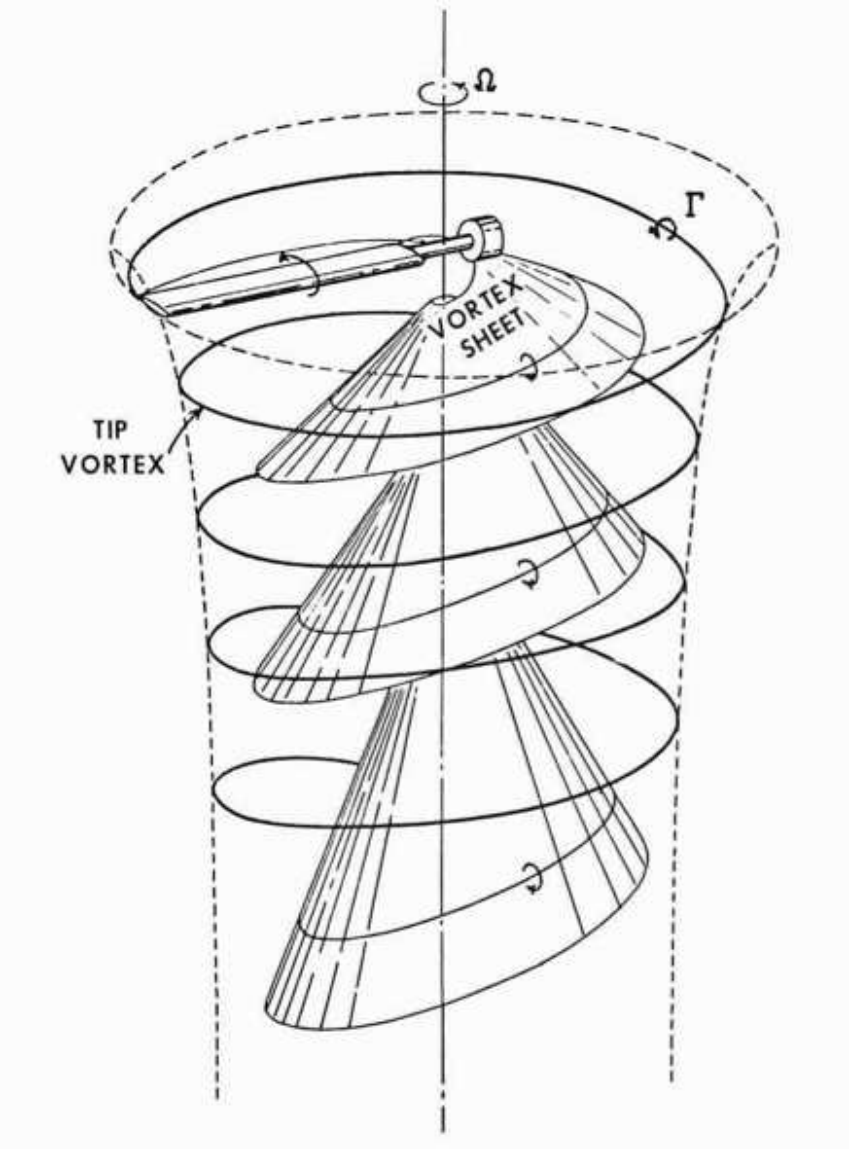

Figure 1.3: Traditional schematic of hovering rotor wake structure, taken from Grey [2].

rotor blades, to solve for the induced velocities over the rotor disk, utilizing the fluid dynamic laws governing vorticity transport - Helmholtz's theorem [36]. When using a vortex method, the rotor wake is modeled by discrete vortex lines in the form of a lattice with either straight elements (such as in the work by Clark [37], Sadler [38, 39], and Scully [40], an illustrated example from Johnson [3] shown in Fig. 1.4) or continuos curved vortex segments (used by Quackenbush, Bliss, and Wachspress [41, 42]), and the convection of the trailing vortices is explicitly and individually tracked. The circulation strength for the shed wake segments relies on the lift distribution and resulting circulation along the blade, usually obtained using a lifting-line or lifting-surface representation of the blade.

A main advantage in vortex methods is that given a wake model, the strength and position of each wake elements is known. Thus, the induced velocity field on the blade can be calculated using the Biot-Savart Law, which provides a solution for a single vortex filaments' contribution to induced velocity at a given point [43]. Integrating for said contributions along all vortices and over the rotor radius will provide the induced velocity distribution along the blade.

Once the induced velocity distributions over the rotor disk have been determined, vortex wake methods are usually combined with the blade element theory (see Section 1.2.1.2) to determine rotor performance.

Vortex wake models are distinguished by the assumptions made for wake geometry. Earlier methods modeled "Undistorted" wake geometries, assuming the location of the wake as known, and are considered simpler and less computationally intense. Such models for hover include purely helical wake, placing the vortex

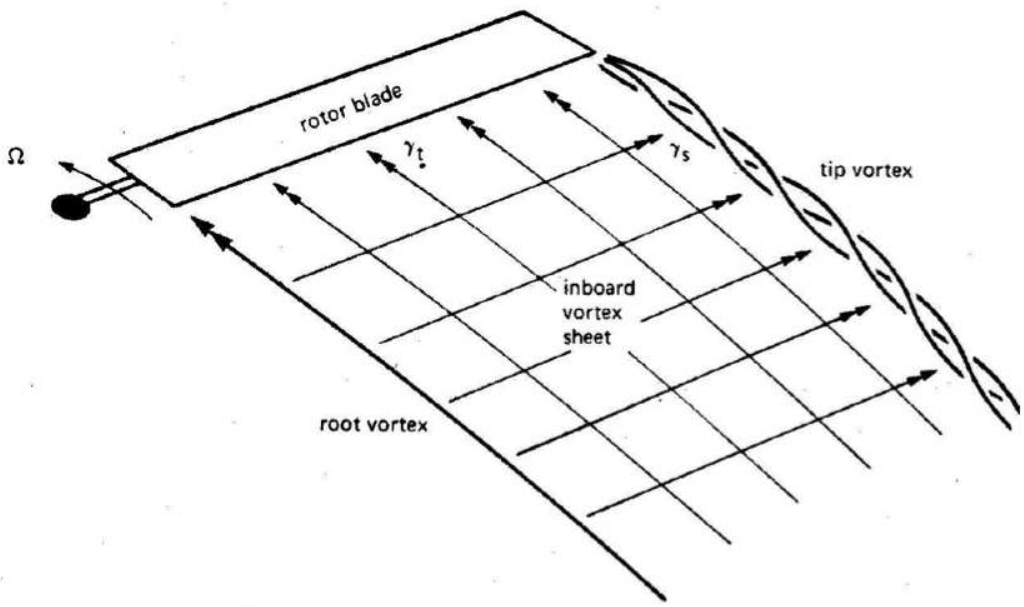

Figure 1.4: Trailed and shed vorticity in rotor wake, taken from [3].

components along the trace of the blade tip paths, and "prescribed" wake models, which define the wake geometry based on empirical information. Nonlinear vortex-lattice methods, known as "free wake" methods, allow each discrete vortex element trajectory to be influenced by all others, deforming the wake system accordingly. Solving for the strength and position of the wake in this manner is substantially more computationally involved, yet generally results in a more accurate solution.

1.2.2.1 Rigid Wake Models

The classical rigid wake model implies an undisturbed helical geometry, in which all wake elements are convected with the same mean axial velocity (such as the models used by Goldstein [44] and Lock [45]). These methods use average constant

velocity solutions obtained from momentum considerations for the transport velocity of the wake, moving helical vortex sheets as rigid surfaces with uniform velocity and no distortion [3]. This wake model is the simplest, least computationally demanding, vortex method, yet is also the the least physically detailed, as rotor wake geometries are known to contract and distort under various operational conditions.

1.2.2.2 Prescribed Wake Models

The prescribed wake models overcome some of the classical rigid wake disadvantages by basing the wake geometry on experimental data, thus taking into account wake contraction and nonuniform inflow distributions along the rotor blades. A generalized prescribed wake model was first developed by Landgrebe in 1971 [46, 32]. Based on a wide range of test data, semi-empirical functions were formulated, relating wake geometry and operational conditions. Following this work, additional prescribed wake models, such as Gilmore and Gartshore [47], Kocurek and Tangler [6], and Kocurek and Berkowitz [48] became popular at a time when computational capabilities were relatively limited . This method has been shown to give good consistent results. However, though somewhat generalized, the semi-empirical nature of these models meant they were limited to experimentally studied flight regimes, and cannot be applied to maneuvering conditions, or new multi-rotor configurations.

1.2.2.3 Free-Vortex Wake Models

Free-vortex wake models, or "deformable" wake models, allow for distortion of the wake geometry from the basic helical shape. This is done by including the velocities induced by the wake on itself, while tracking each wake element as it is convected with the local flow. The development of such computationally intense methods increased with the availability of computational power over the last few decades.

In 1970, Clark and Lieper [37] presented one of the earliest works using a free-vortex method, iteratively solving for vortex strengths and rotor wake geometry, starting from a prescribed geometry as an initial assumption, and allowing the wake to deform under the influence of all flow field components until convergence. This type of free-wake calculation is referred to as a **relaxation based** or **iteration based** free-wake method. Due to the limited computational capabilities of their time, Clark and Lieper modeled only the first two revolutions of tip vortices as free-vortices, understanding that it is this part of the rotor wake that is the most influential.

Sadler (1971) [38, 39] and Scully (1975) [40] followed closely with their own developments of the free vortex method, creating schemes that were more stable numerically, allowing to increase the simulations to account for 6 and 12 rotor revolutions for the hover condition. A similar scheme was later adapted by Johnson [49] in his code CAMRAD.

Although relaxation free vortex methods properly account for the self-induced

velocity effects of the wake, they impose a steady state periodicity to the rotor wake solution as a boundary condition, making them more numerically efficient [1]. This limits these methods from being used for analysis of transient maneuvering and other non-periodic flight conditions. However, relaxation based free-wake models remain widely used when possible (as reviewed by Ananthan in [50]), due to their general advantage of numerical stability and efficiency.

Another general type of free-wake solution methodology is the **Time Marching** free-wake scheme, an approach that appears more attractive for unsteady flight regimes. In this approach no initial wake geometry is required, and the solution can be developed by an impulsive start of the rotor. Ananthan [50] also offers an overview of the development of time marching free wake methods, which are considered to have the fewest restrictions on application to rotor wake problems.

Since it's early days, the free-vortex method has become widely adopted by both industry and academia. Aside from computational fluid dynamics (CFD), free wake methods are considered to provide the detailed solutions for rotor performance. However, various numerical issues associated with solving the governing equations still cause the complexity level of these methodologies to be quite high. Moreover, the still relatively long computational process makes these methods unfavorable for parametric studies.

1.2.3 CFD methods for Wakes

Rapid advances in computer performance (in particular speed and memory) over the past few decades have allowed application of Computational Fluid Dynamics (CFD) methods to helicopter aerodynamics, which are considered to be more computationally-intensive and more numerically complex.

These methods use finite-difference, finite-volume, or finite-element approximations to solve the governing flow equations (either Euler or Navier-Stokes equations), around the entire helicopter rotor flow field. No wake shapes are assumed, and the results are in the form of a set of flow variables (density, momentum, and energy), which can be post processed to generate quantitative and qualitative flow analysis, including loads distribution over the blades.

Past progress in the field of CFD application to rotorcraft problems is reviewed and widely referenced in works by Caradonna [51] and Conlisk [52]. CFD wake modeling generally provides a more detailed view of the rotor wake physics than vortex methods, yet requires enormous computer resources to provide accurate results. One major difficulty in rotor CFD simulations is the moving computation grid that is involved. In most cases the computational grid for the rotor itself is moved through a stationary "world" grid, and thus the computational requirements increase further.

For the case of elastic rotors, the CFD computational grid also needs to be deformed every several numerical iterations, in order to account for blade deformations. After each elastic deformation the flow field requires several more iterations

to reach the new steady state. The process for an elastic rotor is usually done uncoupled (i.e. running a flow simulation until reaching a steady state, applying deformation based on a finite model, and then running flow simulations again, and so on, until both converge).

For the case of ground effect, the CFD grid needs to accurately model the ground and the boundary layer region associated with it. This imposes yet additional requirements on the computational grid (in terms of sufficient resolution near the ground). A typical CFD numerical simulation of a rotor in ground can be found in the work by Kalra et al. [53] for a micro hovering rotor in ground effect.

1.3 Hover in Ground Effect

1.3.1 Effect of the Ground on Hovering Rotor Wake

The flow pattern around a rotor hovering close to the ground is substantially different than in free air. Complexities in the rotor wake that arise in this environment, as illustrated in Fig. 1.5 taken from Prouty [4], result from the ground deflecting the downwards flow induced by the rotor, forcing outwards radial expansion of the wake alongside substantial reduction in vertical velocity due to the ground constraint in the vertical direction (no penetration at the ground dictates zero vertical velocity). This major influence of the ground, increasing as the rotor height off the ground decreases, can be viewed as a source of upwash, reducing the induced velocity at the rotor disk. This, in turn, changes the aerodynamic characteristics of the rotor and it's wake, including force and moment distributions along

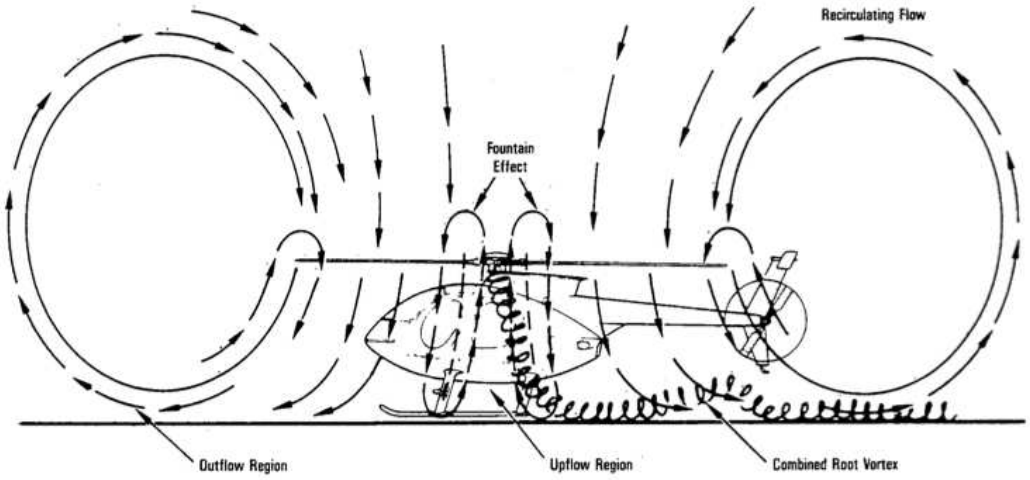

Figure 1.5: Flow pattern around a helicopter hovering close to the ground, taken from [4].

the blades, alongside trailing vorticity strengths and of course differences in wake geometry.

1.3.2 Previous work

Influences of ground proximity on helicopter performance have been extensively studied since the 1940's through experimental and theoretical work, suggesting ground effect to be vital in understanding early helicopters, many of which were inadequately powered for hovering to be possible except close to the ground [54]. The direct influence of ground vicinity, resulting in a decrease in inflow, is typically reflected in experimental work by reduction in power required in-ground-effect relative to power required out-of-ground-effect (P_{IGE}/P_{OGE}) for constant thrust or a corresponding augmentation in thrust for given power, both driven by dimensionless height Z/R. The earliest documented experimental efforts studying ground effect on

the performance of a lifting propeller, conducted by Küssner [55, 56] and Betz [57] in 1937, showed that the effect of ground presence on performance is minimal for propeller heights greater than one radius. Below this height, the power required quickly decreased. Figure 1.6 shows P_{IGE}/P_{OGE} vs normalized rotor height, for a collection of past experimental work, by Knight and Hefner [58], Zbrozek [59], Fradenburgh [60], Koo and Oka [61], Bellinger [62], Hayden [63], and Lee and Leishman [64]. The figure displays said reductions could be as high as $30\% - 60\%$ in total power requirements when hovering very close to the ground.

Earlier theoretical efforts included the work by Knight and Hefner who developed an analytical vortex-cylinder model of the ground effect problem [58], Lighthill's adaptation of actuator disk theory to account for ground effect conditions via fluid-flow mechanics [54], and the work by Cheeseman and Bennet using the method of imaging [65], all resulting in semi-empirical formulas for ground effect benefits. Similarly, simplified empirical models were developed, such as the one proposed by Hayden [63] based on a large set of flight tests data, correcting the induced power due to the presence of the ground. Modern research techniques offered more computationally advanced approaches such as numerical wake computations based on free-vortex theory coupled with mirror images - such as work by Griffiths, Ananthan and Leishman [66, 67, 68], Computational Fluid Dynamics (CFD) work - for example Kalra et. al. [53], and phenomena-based models - such as the work by Khromov and Rand [69], modeling the upwash induced by the ground at the rotor disk to account for ground effect.

However, since helicopter rotors do not generally hover lower than approxi-

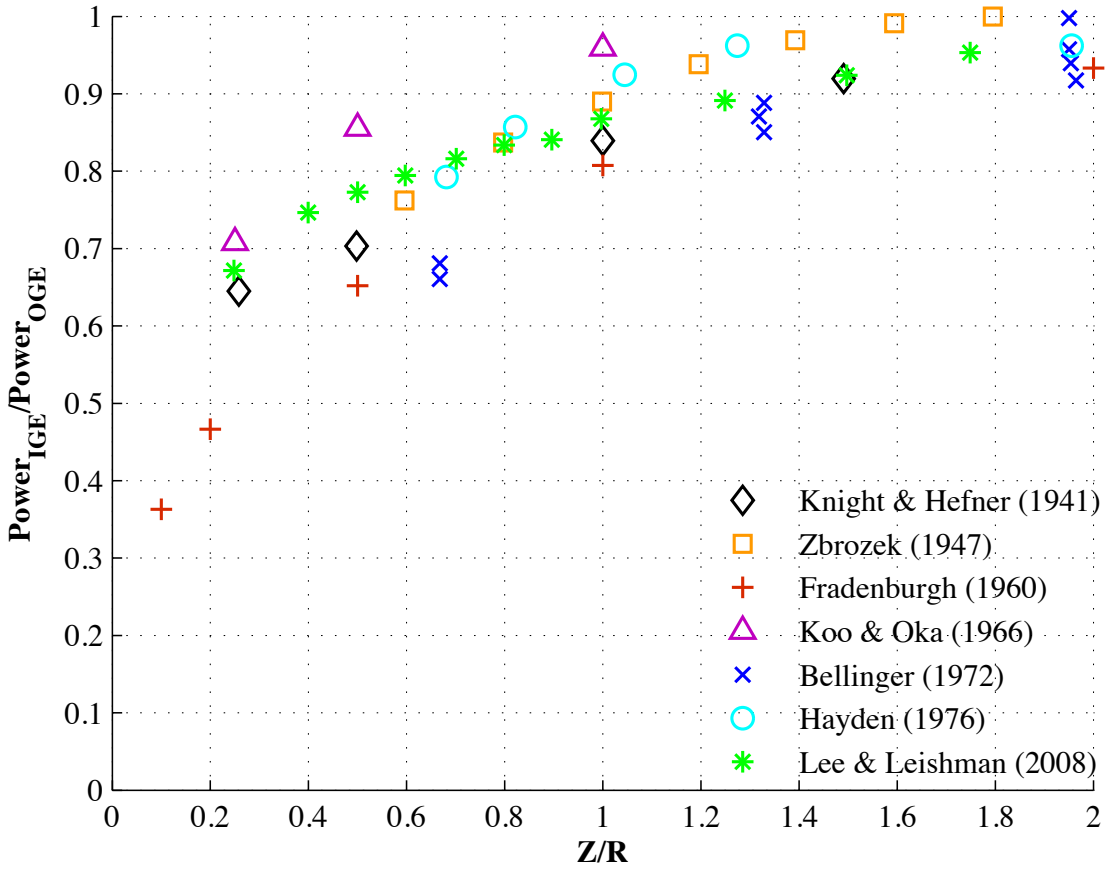

Figure 1.6: Ground effect influence on total power requirements for constant thrust, available results from literature

mately $Z/R = 0.5$ due to fuselage height [60], experimental data for the extreme ground effect regime of $0.05 < Z/R < 0.5$ are scarce. Thus, extracted empirical ground effect models and most of these analytic approaches are of low fidelity in this regime.

Previous works suggest application of ground effect performance trends mostly by multiplying global OGE predicted thrust or power values with some factor $f(\mathrm{Z/R})$ derived from experiments or models [1, 10, 9, 70, 71] at a fixed Z/R value, thus

ignoring the influence of elasticity in ground effect. Since the human powered helicopter rotors are characterized by high flexibility, causing significant changes in the height off ground along the blade, earlier implementation appear to be insufficient for performance prediction and design of a large HPH rotor.

1.4 Current Work

The goal of the present effort is to develop a predictive tool for performance evaluation of a highly elastic rotor in extreme ground effect, which captures the effect of variation in $Z(\tilde{r})/R$ along a substantially deflected blade. For this analysis, classical blade element theory is used in conjunction with a finite element model accounting for blade bending and torsion. The analysis employs and compares two separate approaches towards calculating induced velocities for a rotor in ground effect. An enhanced Blade Element Momentum Theory (BEMT) calculation is initially used, modeling the effect of ground vicinity by employing empirical ground effect trends on each blade element according to it's own height off ground. A more detailed prescribed wake calculation is then implemented, based on a newly developed wake geometry model for a rotor hovering in ground effect.

Additionally, two new sets of experimental data are presented, providing results in the scope of interest (where previous results are scarce). These results are used for a detailed validation of the proposed models for rotor performance in extreme ground effect. The first experiment is of a sub-scale rigid rotor, while the second is a full scale test set-up of a flexible HPH rotor.

Chapter 2

Formulation

The methodology for the analysis in this work is based on the classical blade element theory, introduced in Section 1.2.1, coupled with a rigid wake model (two different approaches considered). Additionally, a Finite Element Method (FEM) is used to incorporate blade bending and torsion into the solution (uncoupled analyses). 2-D airfoil wind-tunnel data tables are used for lift, drag, and pitching moment characteristics at different angles of attack throughout the blade.

2.1 Blade Element Theory Formulation

The formulation for the blade element theory (BET) detailed hereafter, is an iterative process, converging for a required thrust value, as described in it's basic form in Fig. 2.1.

This method requires knowledge of the following rotor parameters: number of blades (N_b), rotor radius (R), blade chord distribution ($c(\tilde{r})$), blade bending and torsional stiffness distributions ($EI(\tilde{r})$ and $GJ(\tilde{r})$), pre-twist ($\theta_{twist}(\tilde{r})$), rotor RPM, and airfoil characteristics in the form of 2D aerodynamic tables.

Following Leishman [1], the process described in the attached scheme (Fig. 2.1) is initiated by defining a required thrust value (T_{req}), and an initial guess for blade pitch (θ_{ref}) and inflow (λ_{ref}) based on said required thrust, using the following

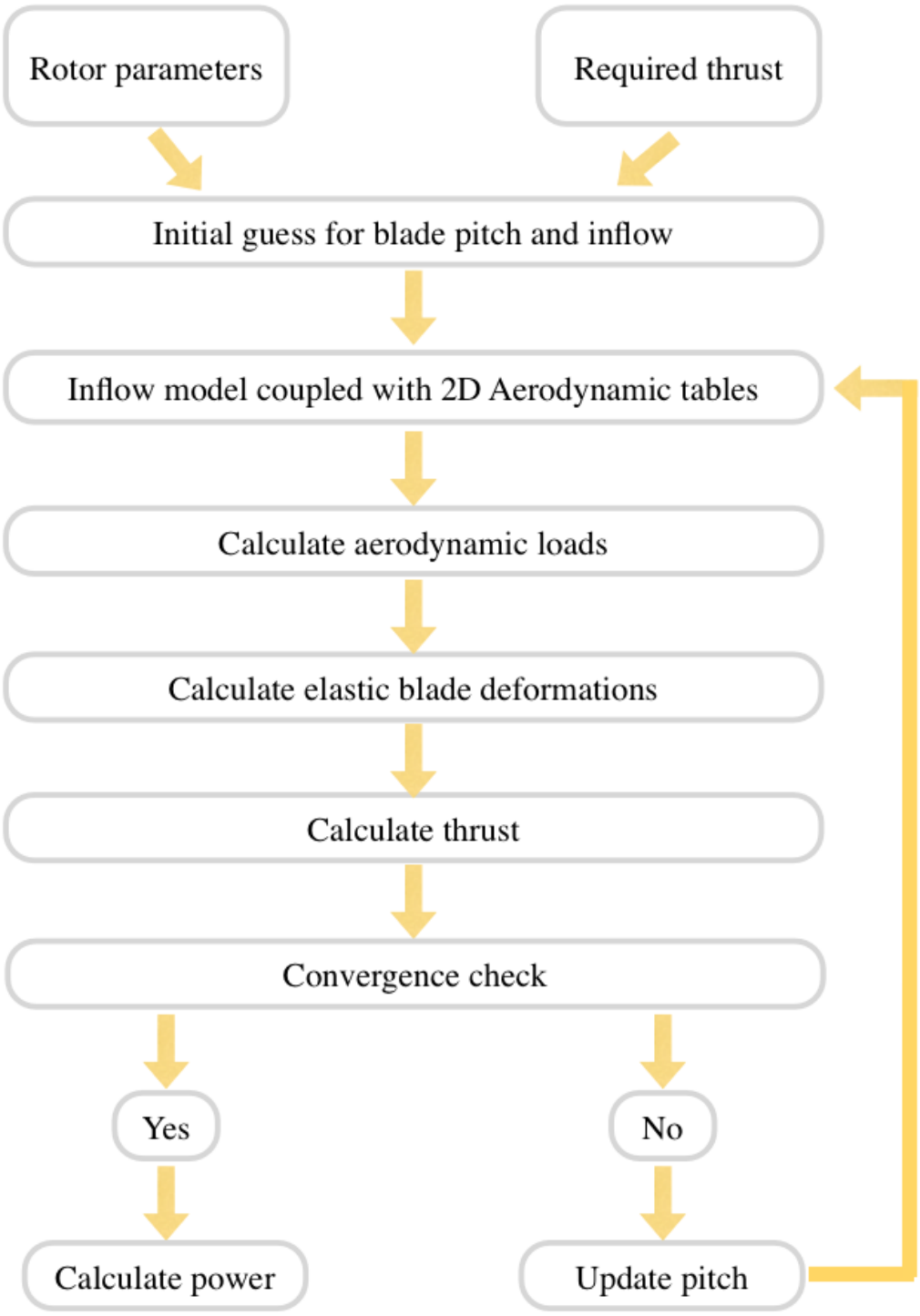

Figure 2.1: Block diagram for basic blade element theory iterative methodology

simplified equations:

$$\theta_{ref} = \frac{6C_{T_{req}}}{\sigma C_{l_\alpha}} + \frac{3}{2}\sqrt{\frac{C_{T_{req}}}{2}} \tag{2.1}$$

$$\lambda_{ref} = \sqrt{\frac{C_{T_{req}}}{2}} \tag{2.2}$$

The process then calculates induced velocities, aerodynamic angles of attack and aerodynamic forces and moments using the chosen inflow model (see Sections 2.2 and 2.3). Once the loads on the rotor blade are determined, the resultant thrust can be calculated by integrating the loads along the blade, and compared to the required thrust. The process iterates on blade pitch θ_{ref}, until the calculated thrust produced by an assigned rotor converges to the required thrust value, using the convergence criterion given by:

$$\left| \frac{C_{T_{req}} - C_T}{C_{T_{req}}} \right| \leq \epsilon \tag{2.3}$$

where ϵ is typically of the order of 0.1% .

Classical blade element theory divides the rotor blade into infinitesimally small, uniformly distributed, blade elements, as demonstrated in Fig. 2.2 (a) for a representative element of width dr. The figure also demonstrates the velocity components, U_T and U_R, influencing the blade element at the rotor disk plane. However, classical BET hover analysis considers the blade elements as quasi 2-D airfoil sections producing aerodynamic forces and moments, and so the effects of radial velocity component U_R are usually neglected in this flight condition [1] and thus:

$$U_T = \Omega r \qquad U_R \approx 0 \tag{2.4}$$

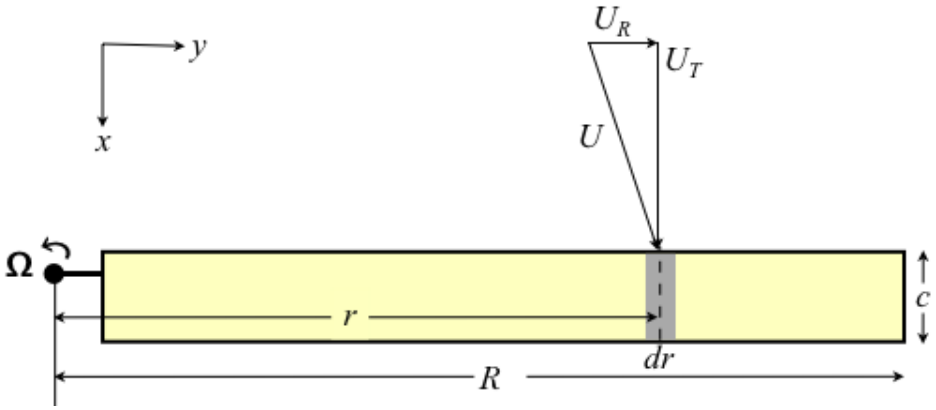

(a) Top view of blade element

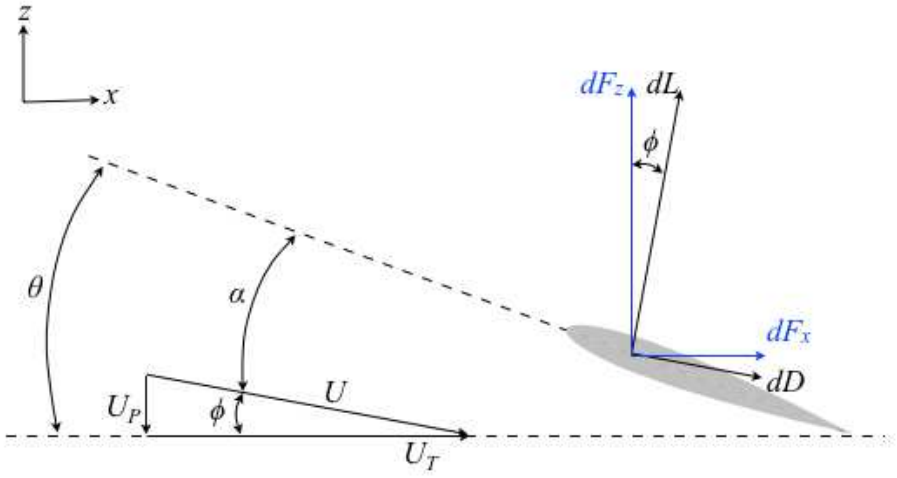

(b) Section view of blade element

Figure 2.2: Forces and Velocities at a typical blade element.

Figure 2.2 (b) further demonstrates the geometry, velocities and forces of the blade element at the airfoil section plane, for an undeformed rigid blade. This figure shows the vertical velocity component U_P which is defined as:

$$U_P = \lambda \Omega R \tag{2.5}$$

where λ is the inflow at the blade element, calculated using the chosen inflow model, and is time-invariant in hover. The resultant velocity at the blade element can therefore be defined as:

$$U = \sqrt{U_T^2 + U_R^2 + U_P^2} \approx \sqrt{U_T^2 + U_P^2} \tag{2.6}$$

The figure also defines the induced angle of attack ϕ, a product of said vertical velocity:

$$\phi = \tan^{-1}\left(\frac{U_P}{U_T}\right) \tag{2.7}$$

Thus defining the effective/aerodynamic angle of attack α, via blade element pitch angle θ as:

$$\alpha = \theta - \phi = \theta - \tan^{-1}\left(\frac{U_P}{U_T}\right) \tag{2.8}$$

The elemental aerodynamic forces, dL and dD, are defined as normal and parallel to the velocity vector, respectively, and formulated as:

$$dL = \tfrac{1}{2}\rho U^2 c\, C_l dr \qquad dD = \tfrac{1}{2}\rho U^2 c\, C_d dr \tag{2.9}$$

where c is the local blade chord, and C_l and C_d are the aerodynamic lift and drag coefficients, extracted per blade section from the 2-D airfoil tables. Lastly, elemental

components of the total rotor aerodynamic forces normal and parallel to the disk plane, are noted as dF_z and dF_x, and can be extracted using the local lift and drag forces (Eq. (2.9)) using simple geometric transformation:

$$dF_z = dL\cos(\phi) - dD\sin(\phi) \qquad dF_x = dL\sin(\phi) + dD\cos(\phi) \tag{2.10}$$

Using calculated forcing terms, the thrust, torque, and power contribution from a blade element at a radial station r can be calculated as:

$$dT \;\; = N_b dF_z \;\; = N_b(dL\cos(\phi) - dD\sin(\phi)) \tag{2.11}$$

$$dQ \;\; = N_b dF_x\, r \;\; = N_b(dL\sin(\phi) + dD\cos(\phi))\, r \tag{2.12}$$

$$dP \;\; = N_b dF_x\, \Omega r \;\; = N_b(dL\sin(\phi) + dD\cos(\phi))\, \Omega r \tag{2.13}$$

This work adopts the standard conventional dimensionless form normalizing length properties by rotor radius R and velocities by blade tip speed ΩR. Using equations (2.11), (2.12), (2.13), and the expressions for elemental lift and drag given in Eq. (2.9) - thrust, torque, and power can be non-dimensionalized as follows:

$$dC_T = \frac{dT}{\rho A(\Omega R)^2} = \frac{1}{2}\sigma(C_l\cos(\phi) - C_d\sin(\phi))\tilde{r}^2 d\tilde{r} \tag{2.14}$$

$$dC_Q = \frac{dQ}{\rho A(\Omega R)^2 R} = \frac{1}{2}\sigma(C_l\sin(\phi) + C_d\cos(\phi))\tilde{r}^3 d\tilde{r} \tag{2.15}$$

$$dC_P = \frac{dP}{\rho A(\Omega R)^3} = dC_Q \tag{2.16}$$

where σ is the local solidity (using the local blade chord c) given by:

$$\sigma = \frac{N_b c}{\pi R} \tag{2.17}$$

A back view of the rotating flexible blade is given in Fig. 2.3, mainly for the purpose of defining a local bending slope angle $\frac{dw}{dy}$ at each blade element (where w is

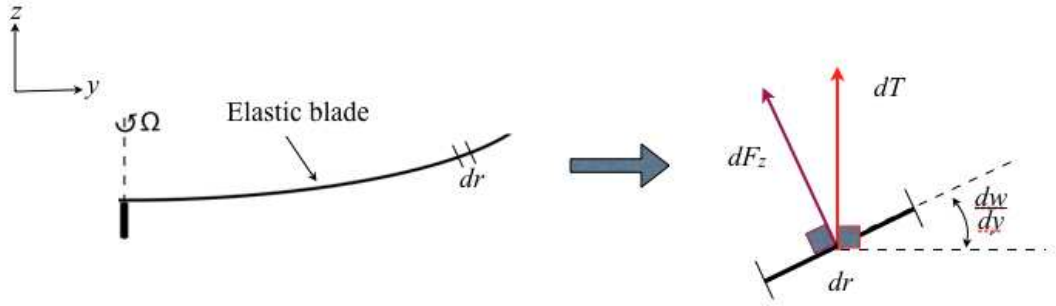

Figure 2.3: Back view of an elastic blade

the local deflection). As seen in the figure, bending of the blade induces additional rotation of the thrust vector. Accounting for said additional rotation:

$$dC_T = \frac{1}{2}\sigma(C_l\cos(\phi) - C_d\sin(\phi))\cos\left(\frac{dw}{dy}\right)\tilde{r}^2 d\tilde{r} \tag{2.18}$$

Torsional deflection of the blade is accounted for within the distributed pitch angle:

$$\theta(\tilde{r}) = \theta_0 + \theta_{twist}(\tilde{r}) + \theta_{torsion}(\tilde{r}) \tag{2.19}$$

Finally, to calculate total thrust and power, the elemental contributions are integrated for over the blade span as such:

$$C_T = \int_0^1 dC_T \qquad \text{and} \qquad C_P = \int_0^1 dC_P \tag{2.20}$$

For a numerical implementation of the blade element theory, this work divides the rotor blade into a finite number of uniformly distributed blade elements, while integration along the blade span is approximated numerically using summation.

The key component in blade element analysis lies in modeling the induced velocity

on the rotor disk, a problem even more complex when studying the behavior of a highly flexible rotor hovering in extreme ground effect. Once the basis of the analysis has been explained, the means in which the author chose to approach modeling the inflow are discussed later in Section 2.2 and Section 2.3 below .

2.2 Inflow Model Using BEMT

This work initially approaches the matter of providing an inflow model using Blade Element Momentum Theory (BEMT), a basic tool for rotor analysis and design. As result of its simplicity, BEMT is a widely used theory for this task, allowing relatively easy implementation for various condition of axial flight, including hover, climd, descent, and operation in ground effect. In this case, the ground effect is implemented on an elemental level, through empirical based reduction of inflow as a function of distance from the ground.

Idealizing the blade elements as 2-D airfoils, in consistency with BET, classical BEMT does not model 3-D effects embodying influences of the blade annuli on each other.

2.2.1 General BEMT Formulation Out of Ground Effect

The BEMT formulation yields an expression for the time-averaged inflow over each elemental annulus out of ground effect $\lambda_{OGE}(\tilde{r})$. The main equation driving this formulation is said inflow expression, derived from equating the expressions for incremental thrust coefficient dC_T from momentum theory and blade element theory

(see Eq. (2.14)), assuming a rigid blade.

$$4\lambda\lambda_i\tilde{r}d\tilde{r} = \frac{1}{2}\sigma C_{F_z}\tilde{r}^2 d\tilde{r} \tag{2.21}$$

For this work, which obtains lift and drag coefficients as a function of calculated aerodynamic angle of attack from experimentally based aerodynamic tables, it was important to leave C_l as such and not break it into the quite common representation of $C_{l_\alpha}\alpha$ as used in the reference formulation. For higher accuracy simulation of power losses, induced tip losses were accounted for using the Prandtl tip-loss factors (see Eq. (2.22), as detailed in Leishman [1]).

$$f = \frac{N_b}{2}\frac{1-\tilde{r}}{\lambda}; \qquad F = \frac{2}{\pi}\cos^{-1}(e^{-f}); \tag{2.22}$$

When combined, equations 2.21 and 2.22 result in the expression for elemental inflow, as shown in Eq. (2.23).

$$\lambda = \sqrt{\frac{1}{8F}\sigma C_{F_z}\tilde{r}} \tag{2.23}$$

Once the inflow distribution is obtained, an updated value of the local angle of attack can be calculated using equation Eq. (2.24)).

$$\alpha = \theta - \tan^{-1}\left(\frac{\lambda}{\tilde{r}}\right) \tag{2.24}$$

Determining the aerodynamic angle of attack allows retrieving C_l, C_d, and C_m from the 2-D airfoil tables. Forcing terms can now be calculated as demonstrated in Eq. (2.10), leading to thrust distribution as in Eq. (2.18), which is integrated over the blade for total thrust coefficient.

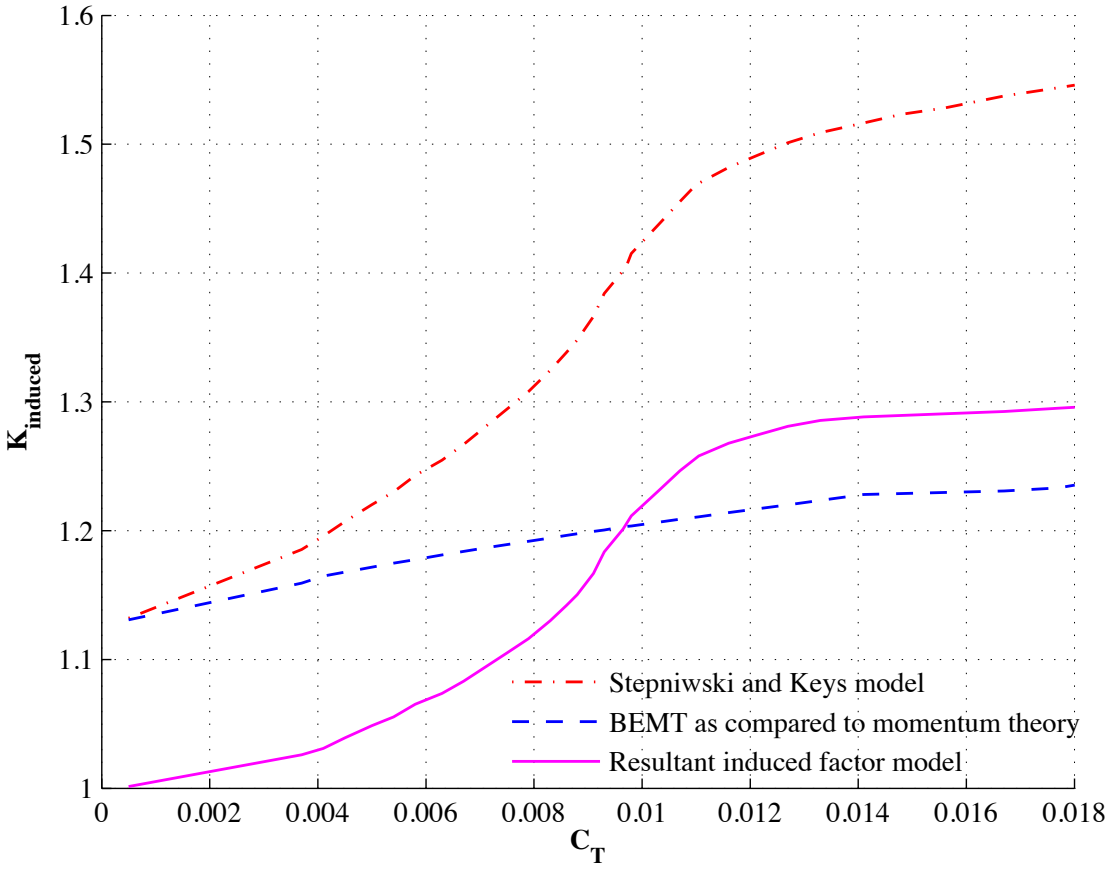

Figure 2.4: Induced power factor as a function of operational C_T, for $N_b = 2$ and $\theta_{twist} = 0$. Based on a study from Stepniewski and Keys [5]

This process is iterated until $C_T = C_{T_{req}}$ (as schematically demonstrated in Fig. 2.1), and finally, power coefficient distribution is calculated as described above (see Eq. (2.16)), and integrated for a final solution.

One of the unique characteristics of HPH rotors, is a relatively slow rotation speed resulting in relatively high operational C_T values. For example, the Yuri I rotors rotated at 22 RPM, operating at roughly $C_T = 0.018$ [11], a value substantially higher compared to a typical rotor ($C_T \approx 0.005 - 0.008$). A study by

Stepniewski and Keys [5] shows that for C_T values this high the induced power factor $k_{induced}$, typically valued at 1.15 when comparing to uniform inflow - momentum theory calculations, increases substantially to values surpassing 1.5 for an untwisted two-bladed rotor. The original study attributes this trend to losses not modeled in ideal power calculations such as non uniform inflow distribution, compressibility effect, increased drag at higher lift coefficients, and tip losses. However, the BEMT formulation in this study partially accounts for non uniform inflow distributions (solving for inflow at each blade element), compressibility effects (by means of 2-D aerodynamic tables), and tip losses (using Prandtl's correction model). As presented in Fig. 2.4, additional losses were isolated by subtraction of the BEMT predicted losses from the model proposed in by Stepniewski and Keys. The residual $k_{induced}$ trend line, accounts more accurately for said losses, and was used to correct for increased induced power coefficient at high C_T values. This additional correction to the BEMT solution will be shown as necessary for successful validation of the BEMT method, in and out of ground effect (see Sections 3.1.2 and 3.2.2, respectively).

2.2.2 BEMT Formulation IGE

As with most corrections for BEMT modeling, in this work, ground effect was empirically implemented in the BEMT formulation as a local factoring of the inflow on a blade-element level. This was carried out under two common assumptions:

- In hover, induced power dominates the power requirement, i.e. $P_i >> P_0$, and

so:

$$\left(\frac{P_{IGE}}{P_{OGE}}\right)_{induced} \approx \left(\frac{P_{IGE}}{P_{OGE}}\right)_{total} \tag{2.25}$$

- Due to inflow reduction, most of the power benefit is in induced power.

For each nominal rotor hub height $(Z/R)_{hub}$, the code interpolates for P_{IGE}/P_{OGE} within an empirical model such as the ones presented in Section 1.3.2 (Fig. 1.6). As blade deflections are taken into consideration using FEM, the height of each blade element off the ground is defined, creating the $Z(\tilde{r})/R$ distribution along the blade. Implementing the ground effect inflow correction allows accounting for the variation in height above ground via $k_{_G}(\tilde{r}) = k_{_G}(Z(\tilde{r})/R)$. This becomes substantial in performance prediction of HPH rotors in extreme ground effect, where the blades are highly flexible, and the Z/R variation can vary as much as $(Z/R)_{tip} \approx 4(Z/R)_{hub}$.

And so, once the OGE inflow distribution is calculated as described above, IGE inflow distribution $\lambda_{IGE}(\tilde{r})$ can be subsequently calculated as:

$$\lambda_{IGE}(\tilde{r}) = \frac{P_{IGE}}{P_{OGE}}(\tilde{r}) \cdot \lambda_{OGE}(\tilde{r}) \tag{2.26}$$

Once the IGE inflow distribution is obtained, angle of attack, force, and moment distributions in ground effect are calculated as previously demonstrated in Section 2.2.1. Finally, thrust and power solutions in ground effect are acquired.

2.3 Inflow Model Using Prescribed Wake Theory

For a more detailed representation of the physical flow environment, vortex theory was employed towards obtaining induced velocity distributions, as introduced

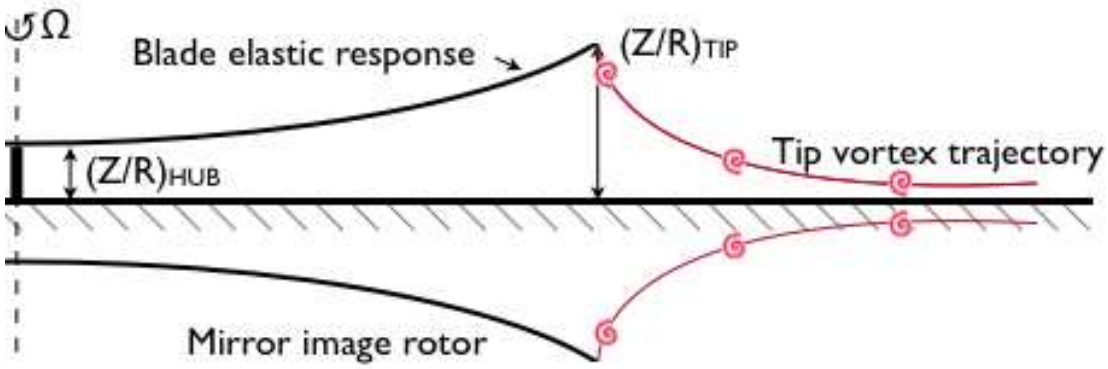

Figure 2.5: Illustration of a highly elastic rotor blade in extreme ground effect with its mirror image

in Section 1.2.2. The prescribed wake methodology is implemented within the BET formulation, using an existing and widely known wake trajectory model, proposed by Kocurek and Tangler in 1976 [6], for the general hover case. To further model the specific problem approached in this work, characterized by operation in extreme ground effect, a newly configured rigid - prescribed wake trajectory model was tailored for these unique conditions. The IGE prescribed wake model is then coupled with a mirror-image wake satisfying a no penetration condition at the ground. This approach is loosely illustrated in Fig. 2.5, demonstrating a highly elastic rotor, it's wake, and the mirror image wake representing the ground condition.

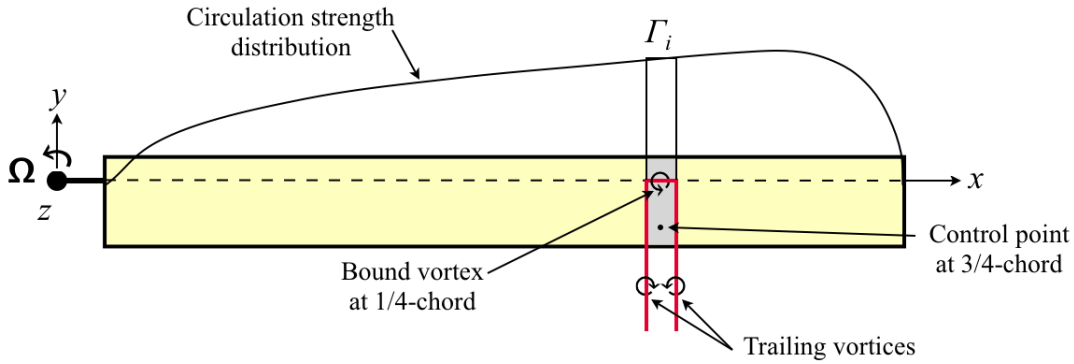

Figure 2.6: Illustration of the lifting line model used to represent the rotor blades, at a typical blade element.

2.3.1 General Vortex Theory Formulation Out of Ground Effect

Wake Representation and Application of Lifting Line Theory

In correlation with BET, and as proposed by Landgrebe [46], each rotor blade is divided into a finite number of elements N_e. Following classical lifting line theory [1], each lifting line element is modeled by a single horseshoe vortex. Each horseshoe vortex is comprised of a bound segment at the blade element quarter-chord and two trailing vortices located at the element boundaries comprising of the same circulation strength Γ. Figure 2.6 illustrates said employment of the lifting line model on the rotor blade.

The rotor wake is then represented by two regions, near-wake and far-wake. The near wake, modeling the first part of the shed wake - closest to the blade, (ex-

tending 15°-45° behind the blade [3]), is comprised of the trailing vortices from each blade element, illustrated for representative number of 5 blade elements, for clarity, in Fig. 2.7 (actual formulation uses a larger number of blade elements, defined via sensitivity studies discussed ahead in Section 3.1.3) . Each trailing vortex is modeled by a finite number of straight vortex filaments of the same circulation strengths extending from the blade trailing edge and defined by wake azimuth intervals, $\Delta\psi$. The far wake is represented by a single tip vortex of constant circulation strength (one tip vortex for each blade), determined by the maximum circulation along the blade span [3]. Each tip vortex is considered for a finite number of N_{rev} rotor revolutions (typically $N_{rev} = 10$ was found to be sufficient) and is divided into a finite number of straight vortex filaments.

The prescribed tip vortex trajectory, as introduced in Section 1.2.2.2, describes the locations of each rotor tip vortex in radial and axial coordinates as functions of wake age, $\tilde{r}(\psi_w)$ and $\tilde{z}(\psi_w)$, respectfully (plotted one versus the other in Fig. 2.9 to illustrate the trajectory). The chosen tip vortex trajectory model provides coordinates, axial and radial, for the start and end points of each straight line tip vortex segment, based on the segment start and end azimuthal locations as demonstrated in Fig. 2.8 (which correlates with Fig. 2.7). The coordinates for the near-wake segments, distributed along the blade, are obtained via interpolation based on the tip vortex trajectory at the correlating azimuthal location. The radial and axial coordinates for each point, can then be transformed to the global, static, coordinate system centered at the rotor hub (Fig. 2.6):

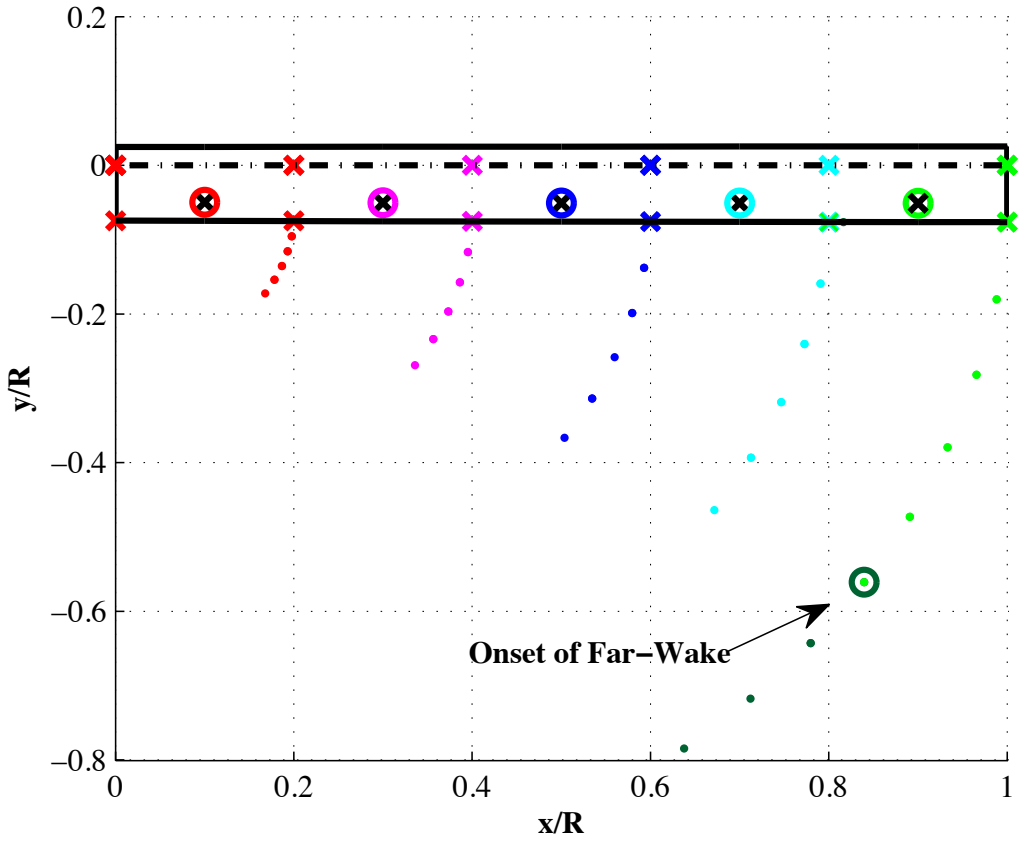

Figure 2.7: Illustration of Near-Wake modeling for 5 representative blade elements

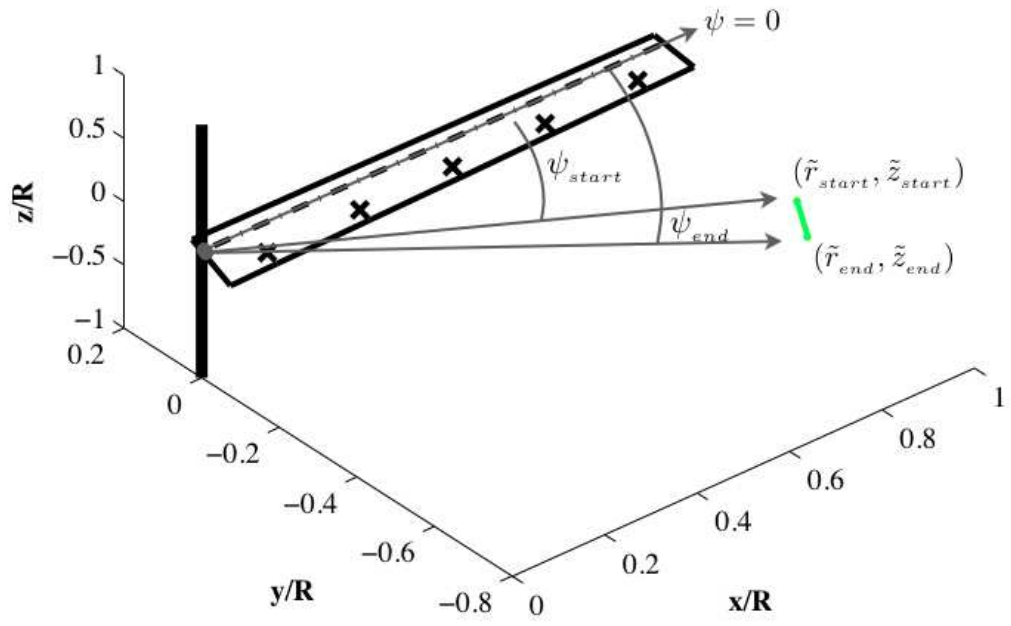

Figure 2.8: Illustration of single tip vortex segment coordinates

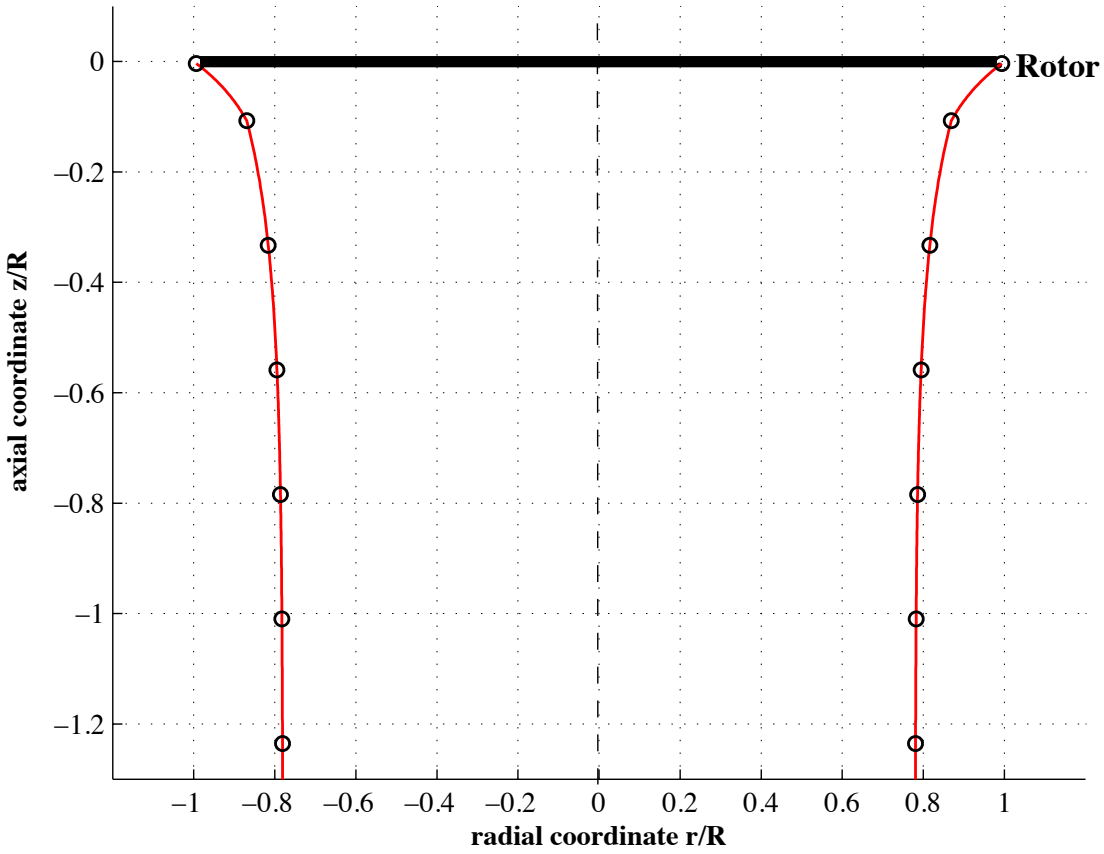

Figure 2.9: Kocurek and Tangler [6] OGE tip vortex trajectory for - $C_T = 0.00516$ (markers represent shed tip vortices from two blades)

$$\begin{cases} x_{start} = \tilde{r}(\psi_{start})\cos(\psi_{start}) \\ y_{start} = -\tilde{r}(\psi_{start})\sin(\psi_{start}) \\ z_{start} = \tilde{z}(\psi_{start}) \end{cases} \qquad \begin{cases} x_{end} = \tilde{r}(\psi_{end})\cos(\psi_{end}) \\ y_{end} = -\tilde{r}(\psi_{end})\sin(\psi_{end}) \\ z_{end} = \tilde{z}(\psi_{end}) \end{cases} \tag{2.27}$$

For general OGE calculations, a prescribed wake model given in Kocurek and Tan-

gler [6] was used, describing the tip vortex geometry using the following equations:

$$\tilde{r}_{tip} = \frac{r_{tip}}{R} = A + (1 - A)\exp\left(-\Lambda\psi_w\right) \tag{2.28}$$

where the radial contraction ratio and radial contraction rate parameter are given by $A = 0.78$ and $\Lambda = 4\sqrt{C_T}$.

And -

$$\tilde{z}_{tip} = \frac{z_{tip}}{R} = \begin{cases} k_1\psi_w & \text{for} \quad 0 \leq \psi_w \leq \frac{2\pi}{N_b} \\ k_1\frac{2\pi}{N_b} + k_2(\psi_w - \frac{2\pi}{N_b}) & \text{for} \quad \frac{2\pi}{N_b} \leq \psi_w \end{cases} \tag{2.29}$$

where the generalized equation for the initial axial settling rate k_1 is:

$$k_1 = B + C\frac{(C_T)^m}{(N_b)^n} = -0.000729\theta_{tw} + (-2.3 + 0.206\theta_{tw})\frac{(C_T)^m}{(N_b)^n} \tag{2.30}$$

while the axial settling rate after the second blade passage, k_2 is given by:

$$k_2 = -\left(C_T - C_{T_0}\right)^{1/2} = -\left(C_T - N_b^n(-B/C)^{1/m}\right)^{1/2} \tag{2.31}$$

and the empirical fit coefficients are:

$$\begin{aligned} B &= -0.000729\theta_{tw} & C &= -2.3 + 0.206\theta_{tw} \\ m &= 1 - 0.25\exp\left(0.04\theta_{tw}\right) & n &= 0.5 - 0.0172\theta_{tw} \end{aligned} \tag{2.32}$$

Utilization of the Biot-Savart Law

Utilization of the lifting line blade model detailed above towards the required inflow distribution makes wide use of the Biot-Savart law. Biot-Savart law is used to calculate the velocity induced by a vortex segment on a control point, using the segments start and end coordinates, its circulation strength, and the control point coordinates. Formulation of the Biot-Savart law in this work is based on the one

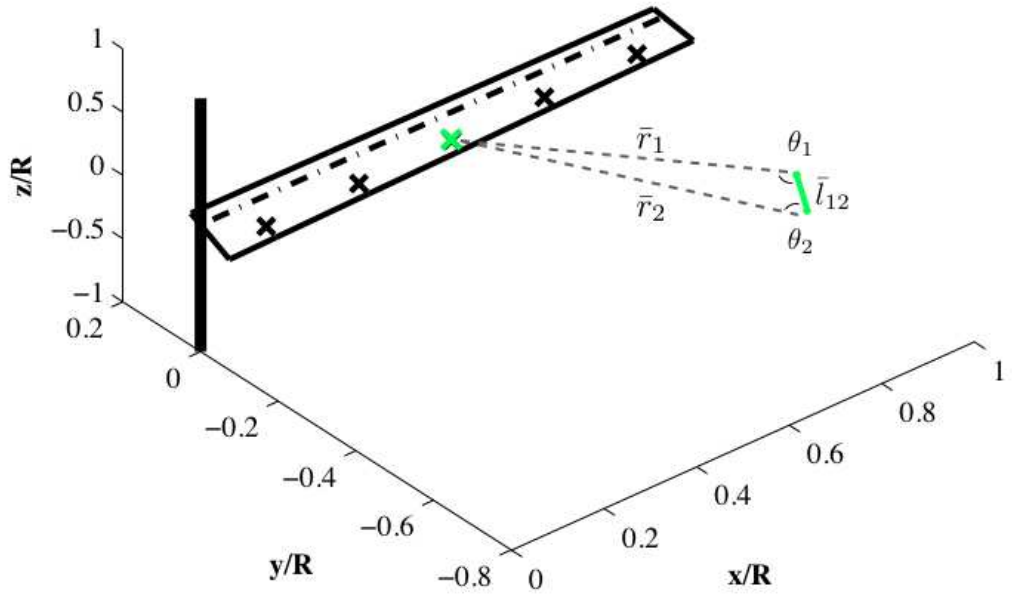

Figure 2.10: Illustration of single tip vortex straight line segment, definition of components used in Biot-Savart calculation

proposed by Leishman [1] and is requires definition of 3 vectors and two angles for each calculation, as illustrated in Fig. 2.10 and specified below:

- $\bar{\mathbf{l}}_{\mathbf{12}}$ - representing the straight line vortex segment, $\bar{\mathbf{r}}_{\mathbf{1}}$ - connecting the control point and the segment start point, and $\bar{\mathbf{r}}_{\mathbf{2}}$ - connecting the control point and the segment end point.

- $\theta_{\mathbf{1}}$ - representing the angle between $\bar{r}_1$ and $\bar{l}_{12}$, and $\theta_{\mathbf{2}}$ - between $\bar{r}_2$ and $\bar{l}_{12}$

Once all geometric components are well defined, Biot-Savart law calculates for

the velocities induced on the control point by said vortex segment of circulation strength Γ_i:

$$\begin{Bmatrix} Vx \\ Vy \\ Vz \end{Bmatrix} = \frac{\Gamma_i}{4\pi} \frac{h}{r_c^2 + h^2} \left(\cos(\theta_1) - \cos(\theta_2)\right) \frac{\bar{l}_{12} \times \bar{r}_1}{|\bar{l}_{12} \times \bar{r}_2|} \tag{2.33}$$

The formulation, presented in Eq. (2.33), notes h as the perpendicular distance between the control point and the vortex segment, and r_c as the vortex "core" dimension. The vortex core radius initial value r_{c_0} is set at $\psi_w = 0$ as a function of the operational C_T, as studied and modeled by Young [72]. Accounting for dissipation, the viscous vortex core is then diffused as a function of circulation strength and vortex age, according to the relation from Bhagwat [73] (using a typical value of $a_1 = 10^{-4}$):

$$r_c(t) = 1.12\sqrt{4\nu\delta t} = 1.12\sqrt{4\nu \left(1 + a_1 \frac{\Gamma_{ave}}{\nu}\right) t} \tag{2.34}$$

Biot-Savart law is thus repeatedly used, calculating the influence of each vortex segment on each blade element. Summation of total influences per blade element will result in the complete induced velocity vector at that control point, providing the inflow distribution along the blade.

Solution for Circulation Strength Distribution

For a given wake trajectory, the circulation strength distribution $\overline{\Gamma}(\tilde{r})$ can be itera-

tively solved for, using an initial guess, via the following steps:

i. Defining tip vortex circulation strength $\Gamma_{tip} = max(\overline{\Gamma})$.

ii. Calculating far-wake induced velocities using Biot-Savart law and Γ_{tip}, so that for each blade element:

$$\bar{v}_{_{FW}} = \begin{Bmatrix} v_x \\ v_y \\ v_z \end{Bmatrix}_{_{FW}} \tag{2.35}$$

iii. Obtaining expressions for near-wake induced velocities, in the form of coefficient matrices $\left[A_{_{NW}}\right]$ calculated using Biot-Savart law and an unknown distribution $\overline{\Gamma}(\tilde{r})$, so that for each blade element :

$$\bar{v}_{_{NW}} = \begin{Bmatrix} v_x \\ v_y \\ v_z \end{Bmatrix}_{_{NW}} = \begin{Bmatrix} \left[A_{_{NW}}\right]_x \\ \left[A_{_{NW}}\right]_y \\ \left[A_{_{NW}}\right]_z \end{Bmatrix} \cdot \overline{\Gamma} \tag{2.36}$$

iv. Using both vectors of wake induced velocities and the local blade element velocity $\Omega\tilde{r}$, employ a no-penetration condition at the 3/4 chord and mid span of each blade element, solving a system of N_e equations for $\overline{\Gamma}(\tilde{r})$ - circulation strength distribution, so that in the direction normal to chord:

$$\left[A_{_{NW}}(\tilde{r})\right] \cdot \overline{\Gamma}(\tilde{r}) + v_{_{FW}}(\tilde{r}) - \Omega\tilde{r}\sin(\theta(\tilde{r})) = 0 \tag{2.37}$$

Or when accounting for bending deflections using the bending slope defined in Fig. 2.2 (c):

$$\left[A_{_{NW}}(\tilde{r})\right] \cdot \overline{\Gamma}(\tilde{r})\cos(\phi_{elastic}) + v_{_{FW}}(\tilde{r})\cos(\phi_{elastic}) - \Omega\tilde{r}\sin(\theta(\tilde{r})) = 0 \tag{2.38}$$

The initial guess for Γ_{tip} is based on the following approximation, assuming on a constant Γ along the blade:

$$T = N_b \cdot \int_0^R \rho U \Gamma dr = N_b \cdot \int_0^R \rho \Omega r \Gamma dr = \frac{N_b}{2} \rho \Omega R^2 \Gamma \tag{2.39}$$

And so:

$$\Gamma_{tip} = \frac{C_T \cdot 2\pi \Omega R^2}{N_b} \tag{2.40}$$

Solution for Blade loads and Inflow Distribution

Once the strengths of the wake vorticity have converged (defined when the maximum change in $\overline{\Gamma}(\tilde{r})$ does not exceed 0.01%), this distribution is used to calculate the corresponding aerodynamic lift coefficient using the relation:

$$L(\tilde{r}) = \rho U \overline{\Gamma}(\tilde{r}) = \frac{1}{2} \rho U^2 c \cdot C_l(\tilde{r}) \tag{2.41}$$

The angle of attack distribution can then be extracted via 2D aerodynamic tables using the C_l distribution, subsequently providing C_d and C_m distributions through the 2D tables. Forces and moments are integrated along the blade yielding thrust, torque, and power values using BET formulation as detailed above in Section 2.1. FEM is then carried out using the distributed loads to obtain blade deflections, defining the height and pitch of each blade element creating the $Z(\tilde{r})/R$ distribution along the blade, and updating the geometry and control points of the modeled shed vortices.

2.3.2 Vortex Theory Formulation, Using a Prescribed Wake IGE

An implementation of the above formulation in extreme ground effect required a new prescribed trajectory representing the wake behavior in this environment. Setting out to create an empirically based wake trajectory required detailed experimental wake measurements at varying IGE heights and loading conditions. The work by Light [74] presents experimental result for rotor tip vortex geometry, in an out of ground effect, collected using the wide field shadowgraph method. However, the IGE wake trajectories in this work are presented for the limited wake age of $250° - 450°$, and thus were considered insufficient for this task as the vortex method required modeling multiple revolutions for good representation of the physical induced velocities (discussed in [46] and demonstrated via a sensitivity study shown ahead in Section 3.1.3)

The work by Griffiths and Leishman [66] demonstrated comparison of a free-vortex wake method, modeling rotor behavior IGE, with Lights' experimental results, resulting in good agreement. The work further presents rotor tip vortex geometry IGE, at $Z/R = 0.62$, for 12 rotor revolutions. This is done in the form of axial and radial displacements of the tip vortex, similarly to the OGE models of Landgrebe [46] and Kocurek and Tangler [6] discussed in Section 2.3.1. Providing a sufficient number of modeled rotor revolutions, the results of [66] were tailored with a curve-fit to provide analytical functions for $\tilde{z}(\psi)$ and $\tilde{r}(\psi)$, and used as a basis for a new IGE wake trajectory shown (solid line) in Fig. 2.11 and Fig. 2.12.

Generalization of this trajectory was carried out employing the reference case

where $C_T = 0.008$, $Z/R = 0.62$ as a baseline, focusing on the range of interest $Z/R \leq 0.6$ and under two main assumptions for this regime:

i. The wake trajectory shape depends on variation in Z/R alone.

ii. The advancement rate along said trajectory (the tangential velocity) depends on C_T alone.

Implementation of varying rotor height above ground was carried out assuming similarities in trajectory shapes. This assumption presumably breaks down at higher Z/R values, where the radial coordinates are observed to contract more substantially before the ground induced wake expansion initiates [64]. A simple normalization of the reference case $\tilde{z}_{tip}(\psi)$ by its rotor hub height off ground allowed scaling the axial coordinates per Z/R case, while maintaining the same radial coordinates. An example for $Z/R = 0.3$ is compared to the reference case of $Z/R = 0.62$ in Fig. 2.11.

To include the effect of C_T in the proposed wake model, experimental results for rotor wakes IGE from the works of Light [74] and Lee and Leishman [64] were carefully examined, showing that the velocity at the rotor plane, scales with $\sqrt{C_T}$, a result which is consistent with classical momentum theory [1, 3]. This was done by comparing non-dimensional distances (normalized by R) between the first and second tip vortices, varying from each other by $\psi = \pi$, yielding velocities. These comparisons are shown in Table 2.1. Using this result in conjunction with the fact that close to the rotor plane, the tangential velocity is dominated by axial (vertical) velocity, and the fact that vortex elements at the early wake ages also have the

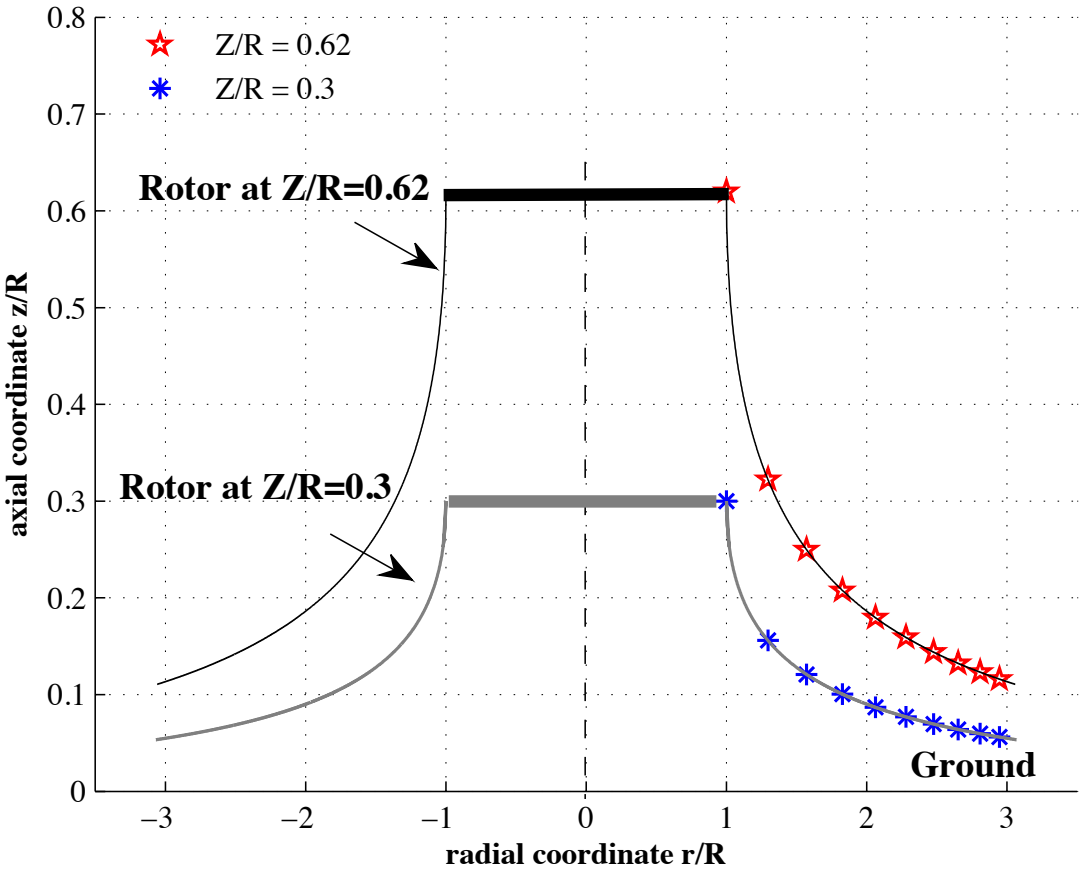

Figure 2.11: Effect of Z/R on prescribed trajectory at $C_{T_{ref}} = 0.008$
Markers represent tip vortices of 1 blade (spacing of $\Delta\psi = 360°$)

$C_{T_{ref}} = 0.008$	$C_{T_1} = 0.0154$	$C_{T_2} = 0.0161$	$C_{T_3} = 0.0196$
$\sqrt{C_T/C_{T_{ref}}}$	1.39	1.42	1.56
$(V/R)_{ref} = 0.055$	$(V/R)_1 = 0.0772$	$(V/R)_2 = 0.0779$	$(V/R)_3 = 0.088$
$(V/R)/(V/R)_{ref}$	1.40	1.41	1.59

Table 2.1: Vertical velocities at the rotor disk for different C_T cases

largest effect on performance calculations, the tangential velocities of the vortices along the prescribed trajectory are scaled with $\sqrt{C_T}$. This is carried out by using the reference case shape functions $\tilde{z}_{ref}(\psi)$, $\tilde{r}_{ref}(\psi)$, and scaling the 'time' coordinate ψ to move 'faster' or 'slower' along the trajectory following the process described below:

i. For $C_{T_{req}} = C_{T_{ref}}$, for every azimuth in the reference case, ψ_{ref}, the tip vortex has traveled a certain distance. For relatively small wake ages, close to the rotor, this distance is traveled mainly in the axial direction, and is approximated as $\Delta\tilde{z}_{ref}$.

ii. For a different case $C_{T_{req}} = C_{T_2} \neq C_{T_{ref}}$, that same distance would be traveled at different time and thus reached at a different ψ_2 which can be calculated as follows:

$$\Delta\tilde{z} = \Delta\tilde{z}_{ref} = \text{constant} \qquad \Rightarrow \frac{V_2}{\psi_2} = \frac{V_{ref}}{\psi_{ref}} = \text{constant}$$

$$\Rightarrow \frac{\psi_2}{\psi_{ref}} = \frac{V_2}{V_{ref}} = \sqrt{\frac{C_{T_2}}{C_{T_{ref}}}} \tag{2.42}$$

iii. We may now generalize for any ψ_{ref}, using the reference point: $C_{T_{ref}} = 0.008$, to get the factored time step ψ_* :

$$\psi_* = \sqrt{\frac{C_{T_*}}{C_{T_{ref}}}} \cdot \psi = \sqrt{\frac{C_{T_{req}}}{0.008}} \cdot \psi \tag{2.43}$$

Fig. 2.12 portrays a representation of this practice, showing faster advancement of tip vortices along the prescribed trajectory (represented by the points) for a higher C_T case *i.e.* higher downwards velocity at the rotor plane and as such the gaps between the points grow larger.

Finally, the equations describing tip vortex geometry in ground effect for $Z/R \leq 0.6$ can be written as:

$$\tilde{r}_{tip}(\psi_*) = \frac{r_{tip}(\psi_*)}{R} = (-0.00025\psi_*^2 + 0.0485\psi_* + 1) \tag{2.44}$$

and

$$\begin{aligned} \tilde{z}_{tip}(\psi_*) = \tilde{z}_{tip}\left(\tilde{r}_{tip}(\psi_*)\right) \quad &= \frac{z_{tip}(\tilde{r}_{tip}(\psi_*))}{R} \\ &= Z/R[-1 + e^{(-1.2035\sqrt{\tilde{r}_{tip}(\psi_*)-1})}] \end{aligned} \tag{2.45}$$

To complete the formulation for the proposed prescribed wake method in ground effect, a mirror image rotor wake is implemented, causing a no-penetration condition at the ground plane. The illustration in Fig. 2.13 presents a single tip

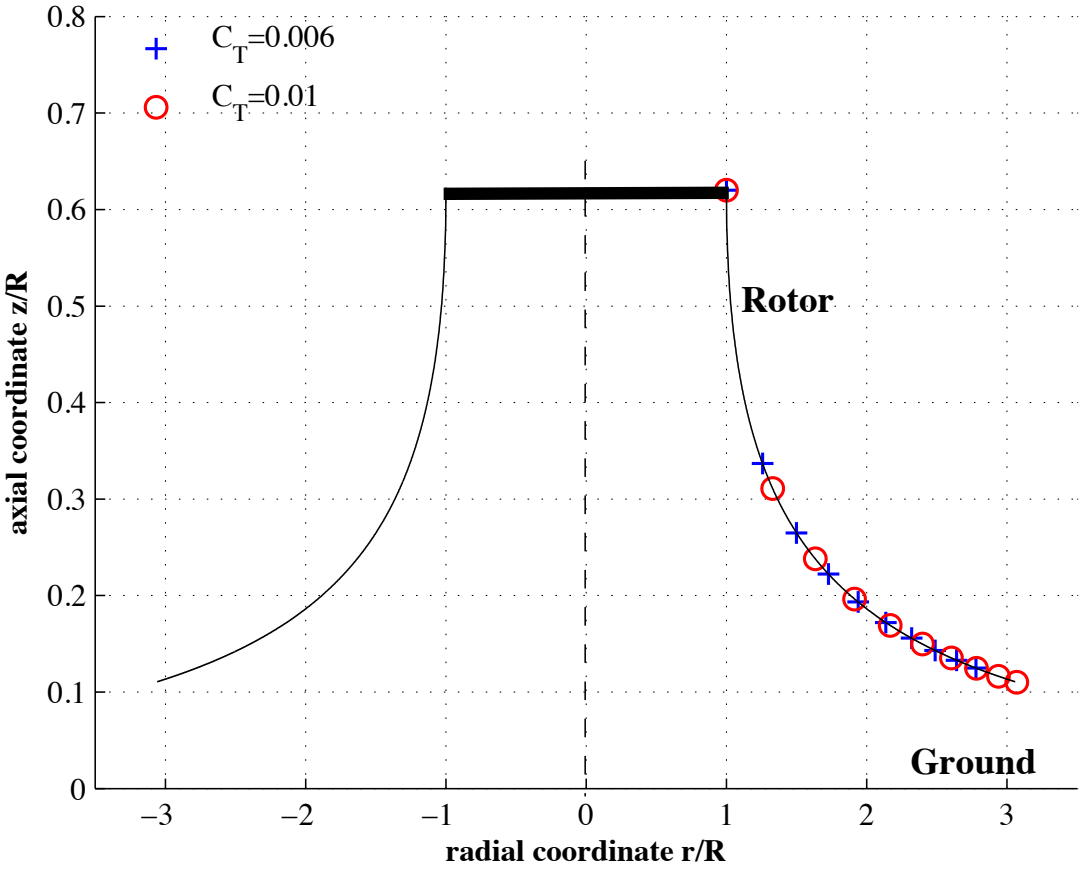

Figure 2.12: Effect of C_T on prescribed trajectory at $Z/R = 0.62$
Markers represent tip vortices of 1 blade (spacing of $\Delta\psi = 360°$)

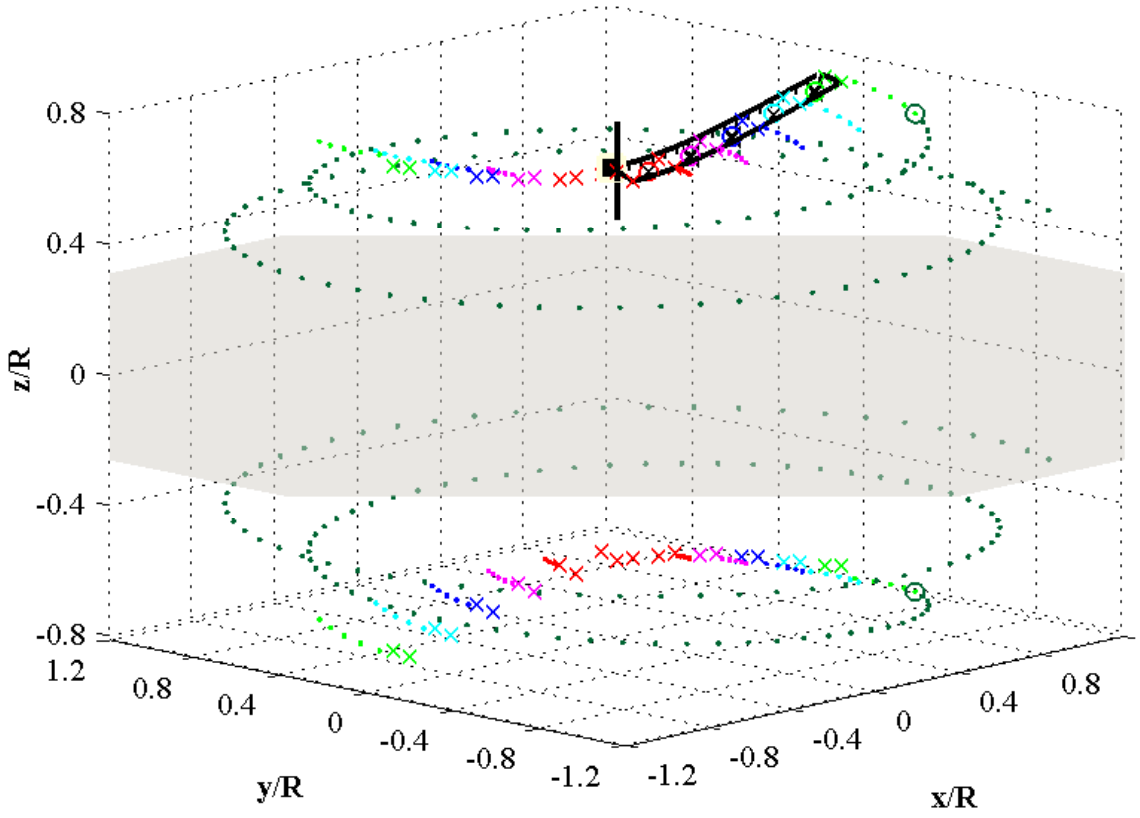

Figure 2.13: Illustrated prescribed wake of an elastic rotor at $Z/R = 0.62$ and its mirror image. Ground plane shown as shaded area

vortex trajectory for both the primary and mirror rotors, as well as a 30° near-wake for 5 representative blade elements (reduced for image clarity), where each pair of points defines one straight vortex filament.

Chapter 3

Validations

To justify the proposed approaches and validate their predictive capabilities, both rotor performance calculation methods proposed in Chapter 2 were compared to experimental results. Validation was carried out for out of ground effect cases as well as in ground effect cases. Initial validation of the process in free air, i.e. out of ground effect, is done using available rotor test data (from literature). Two in-house experiments, designated for the study of extreme ground effect are used for further validation in ground effect.

3.1 Validation Out of Ground Effect and Sensitivity Studies

Initial validation of the code formulation out of ground effect was carried out for both modeling approaches, using experimental data for rotor performance from the literature. Using the same rotor geometries, the sensitivity of each method to driving parameters such as N_e - number of blade elements, N_ψ - number of wake azimuthal elements, and N_{rev} - number of considered wake revolutions, was studied.

3.1.1 FEM Sensitivity Study

Prior to validations of the inflow models, the sensitivity of the uncoupled structural model to the number of structural blade elements was examined, to establish

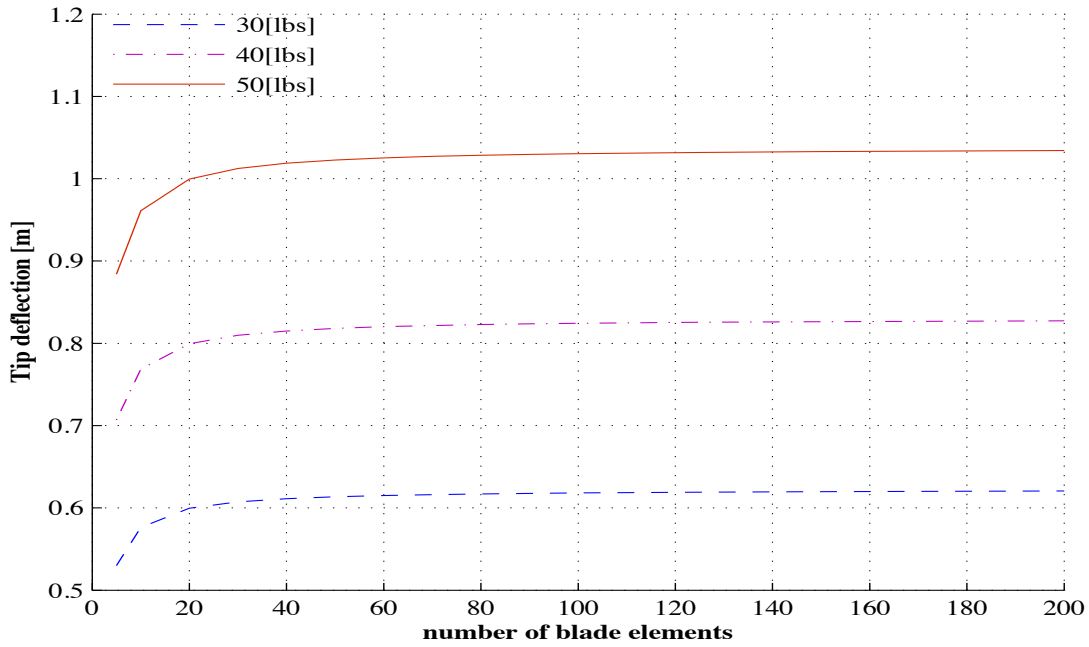

(a) Tip deflection sensitivity to N_e

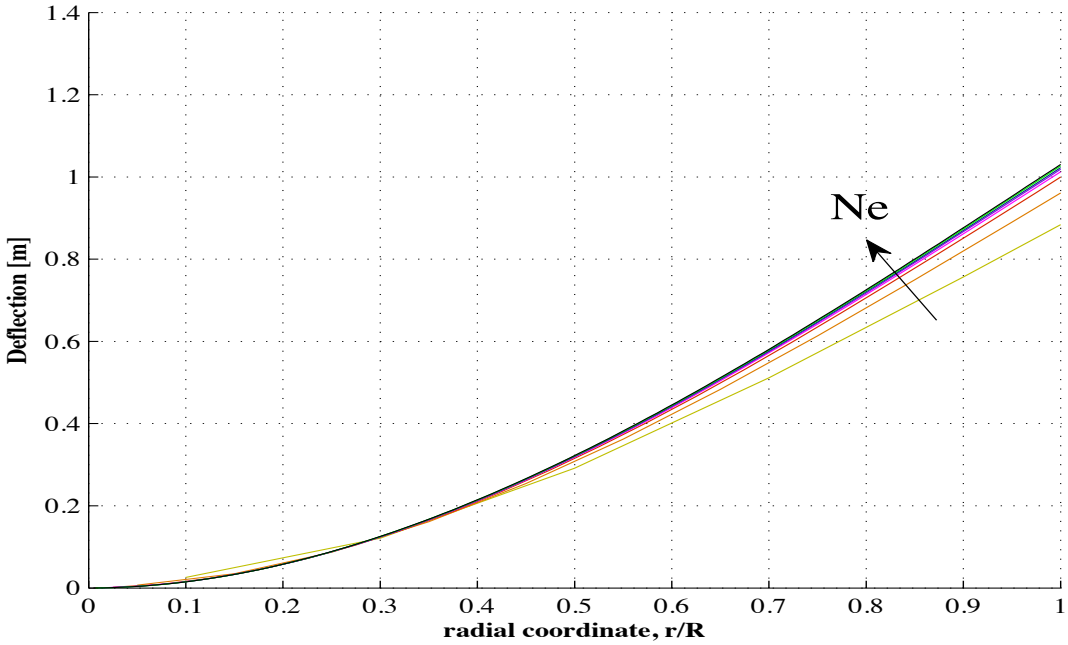

(b) Deflection distribution for 50[lbs], $5 \leq N_e \leq 100$

Figure 3.1: FEM sensitivity to number of blade elements

convergence characteristics of the structural model. Bending of a rotating beam / blade was examined under 3 different tip loads for increasing numbers of uniformly distributed beam / blade elements.

Fig. 3.1(a) shows convergence of tip deflection results for the 3 load cases, all portraying variation of 2% or less for $N_e \geq 30$ when compared to the result for $N_e = 200$. Furthermore, the results present a variation of 1% and less for $N_e \geq 50$. In addition, as can be seen in Fig. 3.1(b), the deflection distribution is well converged for said values of N_e.

3.1.2 BEMT Method Out of Ground Effect

For initial validation of the BEMT formulation detailed in Section 2.2.1, experimental test data from work by Harrington [75] was used. The referenced experiment measures global performance of a rotor consisting of two untwisted, untapered, fairly rigid blades of symmetric NACA airfoils. The reference rotor blades measure 25 ft in diameter and 18 in in chord, and rotate at 200 RPM. To ensure sufficient convergence, a sensitivity study was carried out on the BEMT inflow formulation with respect to number of uniformly distributed blade elements (N_e). Shown in Fig. 3.2(a) for both rigid and elastic blade models, this study concludes that, for both cases, using a blade division of $N_e \geq 30$ converges to inflow results varying by less than 2.5% from the result for $N_e = 200$. Furthermore, using $N_e \geq 50$ would ensure inflow precision within a 1% variation with respect to the same reference value. To further verify FEM convergence, ensuring proper convergence for the highly elastic

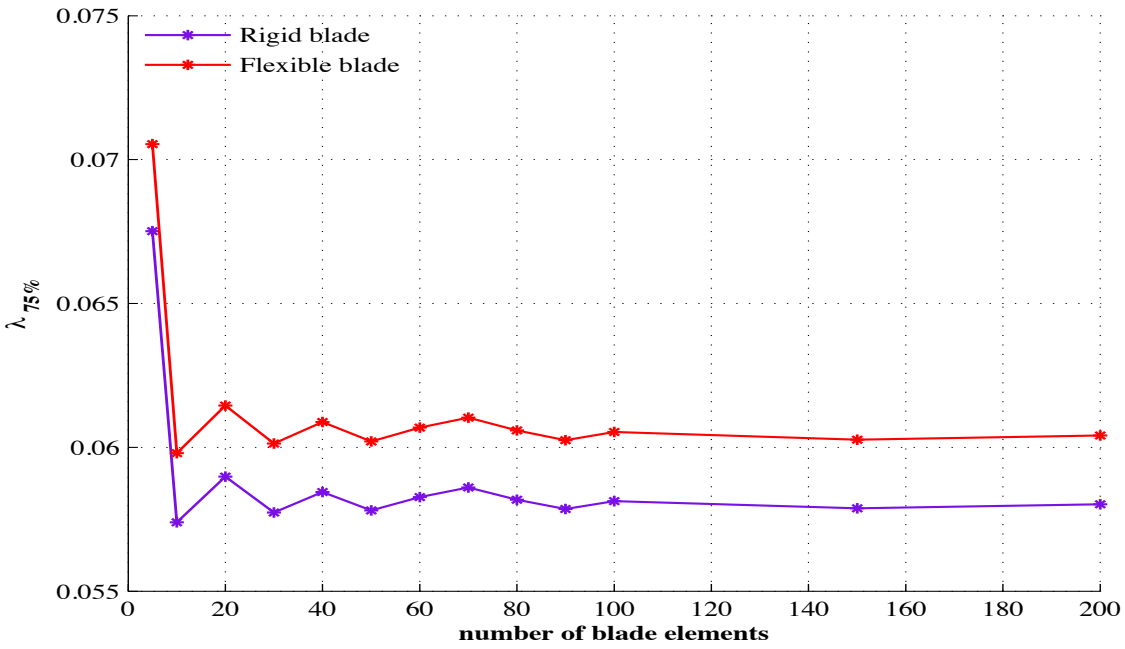

(a) Sensitivity of BEMT to N_e

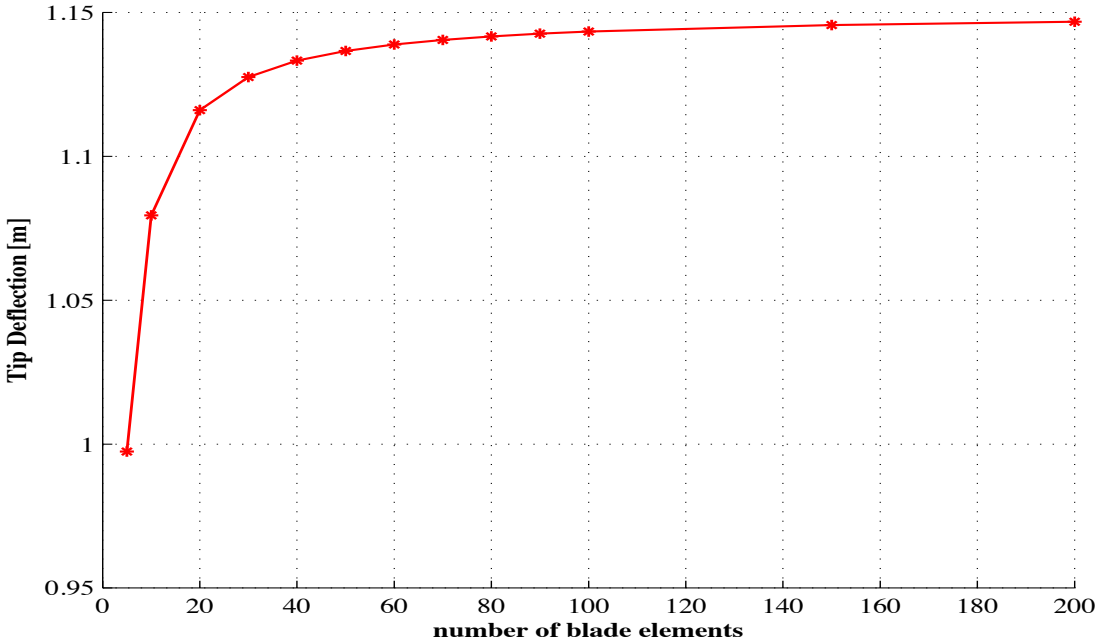

(b) Sensitivity of FEM coupled with BEMT to N_e

Figure 3.2: BEMT sensitivity to number of blade elements at $C_T = 0.005$

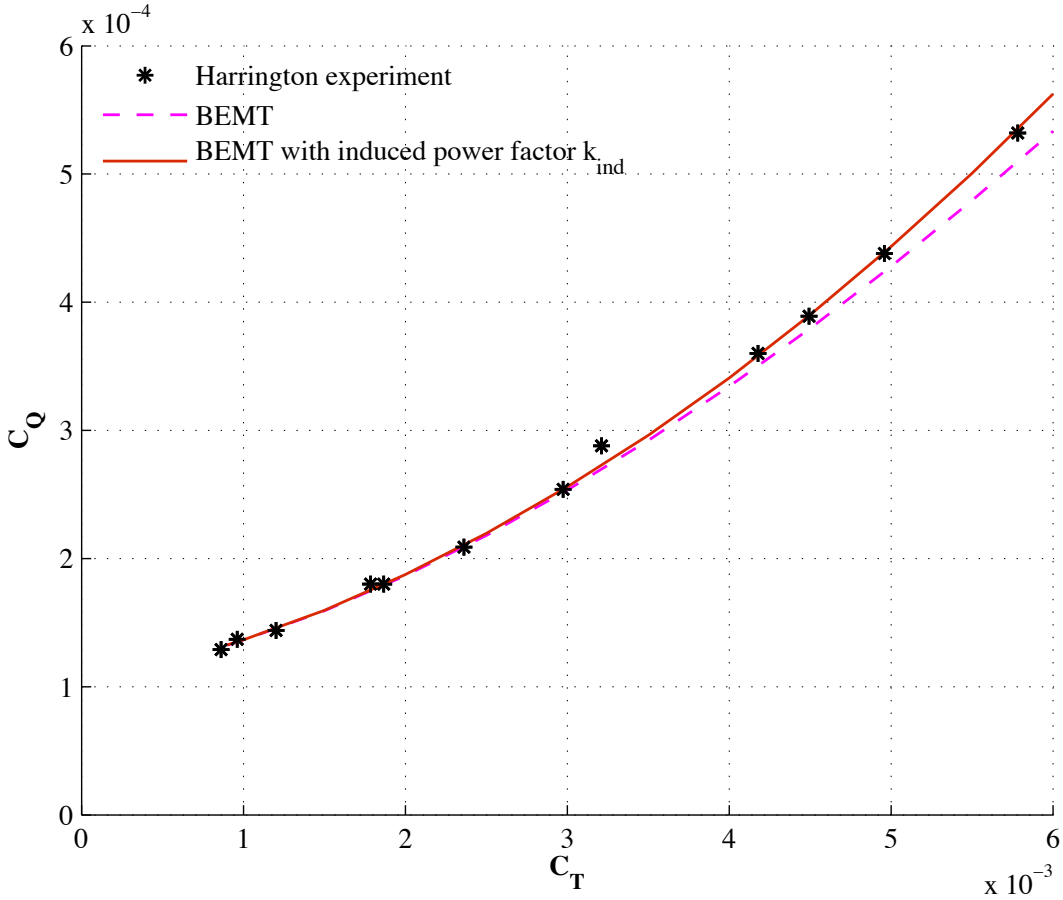

Figure 3.3: OGE validation - BEMT vs experimental results for a rotor with a symmetric NACA airfoil

blade model, variations in tip deflection results for increasing N_e was examined. Shown in Fig. 3.2(b), the tip deflection result was found to vary by less than 1% for $N_e \geq 50$, as compared to the result for $N_e = 200$. Therefore, it was chosen to use 50 blade elements for both BEMT calculations and the structural model.

The code comparison to experimental data, shown in Fig. 3.3, includes calculated results for BEMT with and without the additional induced power factor model shown in Fig. 2.4 and explained in Section 2.2.1, used to better represent

induced power losses at relatively high C_T values. As shown, the calculated BEMT results closely follow the experimental results. It is also apparent that the validation quality is better when including the empirical induced power factor, which accounts for high C_T effects. This improvement will become more apparent for even higher C_T values as to be seen in Figures 3.14 and 3.21.

3.1.3 Prescribed Wake Vortex Method Out of Ground Effect

Initial validation of the prescribed wake formulation, out of ground effect, ensuring correct implementation of the vortex method, was carried out using test data for performance of an AH-1G main rotor as presented in the work by Kocurek and Tangler [6]. The AH-1G rotor, as described by Talbot et al. in [76] has two practically rigid blades, measuring 22 ft in radius and 2.25 ft in chord, featuring a negative linear pre-twist of $-10°$, and rotating at 314 RPM.

Using this rotor geometry, and the wake model given by Kocurek and Tangler in the same body of work [6] (detailed in Equations (2.28) - (2.32)), the prescribed wake formulation was also studied for sensitivity to various driving parameters. As solving for circulation strength is the main driving process in this implementation of the vortex method, it is critical that Γ be well converged (in this model inflow is a mathematical result of the solution for Γ). Therefore, the sensitivity of $\Gamma(\tilde{r})$, and namely Γ_{max} - the tip vortex strength (calculated as $max(\Gamma(\tilde{r}))$, as explained in Section 2.3.1), was studied with respect to N_e - number of blade elements, N_ψ - number of azimuthal segments per revolution dictating the azimuthal step $\Delta\psi$, and

N_{rev} - number of modeled tip vortex revolutions.

Figure 3.4(a) shows sensitivity to the number of blade elements, demonstrating that for $N_e \geq 50$ the tip vortex circulation strength varies by less than 1% at a thrust requirement of $C_T = 0.005$, for both rigid and elastic blade models. Similarly, Fig. 3.5(b) shows the FEM blade tip deflection converging within a 2% error for the same number of blade elements. The formulation sensitivity to the discretization of the wake into straight line segments is shown in Fig. 3.5, where Γ_{max} is solved for using various numbers of segments per wake revolution, which in turn define the segment 'size' $\Delta\psi$. The figure shows mild sensitivity to this parameter, demonstrating variations of 0.25% and less for $N_\psi \geq 36$, correlating with $\Delta\psi \leq 10°$. Once sufficient N_e and $\Delta\psi$ values were determined, the process sensitivity to the number of calculated or 'followed' rotor wake revolutions, N_{rev}, was examined for various thrust cases. An example for this study, shown in Fig. 3.6 for a mid-range C_T of 0.005, demonstrates in that calculating for 6 revolutions or more results in well converging solutions within a 1% variation, a value concluded as sufficient throughout the thrust range.

According to the demonstrated sensitivity studies, prescribed wake vortex method results shown from here on use the following combination of parameters:

$$N_e = 50 \qquad \Delta\psi = 5° \qquad N_{rev} = 10 \tag{3.1}$$

Finally, sensitivity to the 'length' of the near wake ψ_{nw} was also looked into. Based on this study, which as seen in Fig. 3.7 shows only slight variations (1.5%) for $15° \leq \psi_{nw} \leq 45°$, the near wake was chosen to represent the first 30° of the rotor

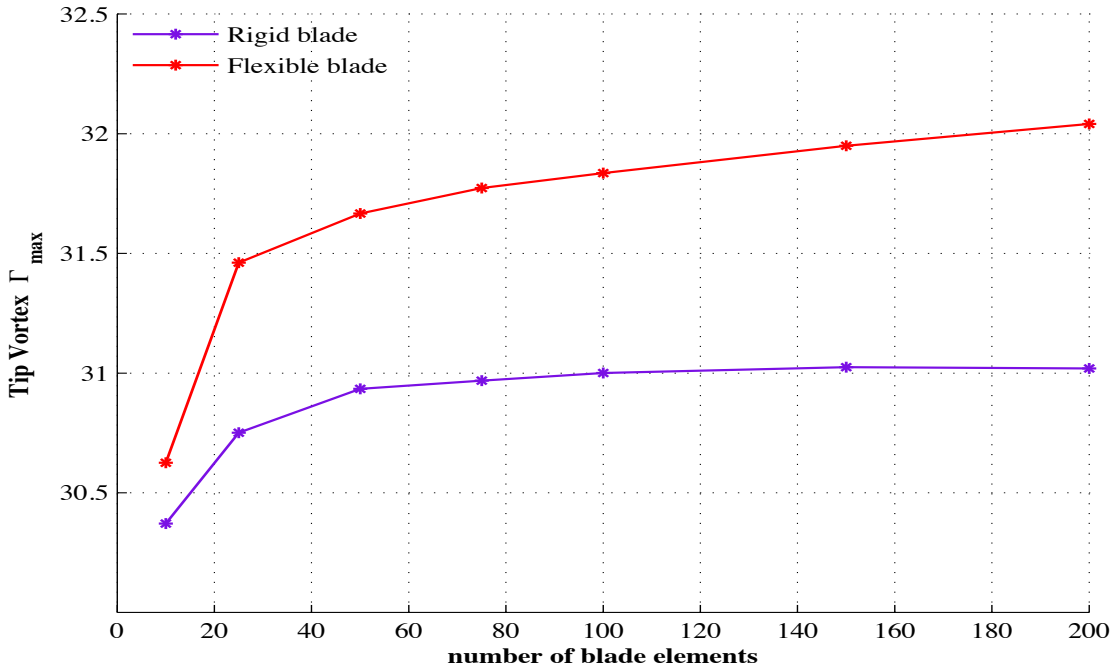

(a) Sensitivity of tip vortex circulation to N_e, using prescribed wake vortex method

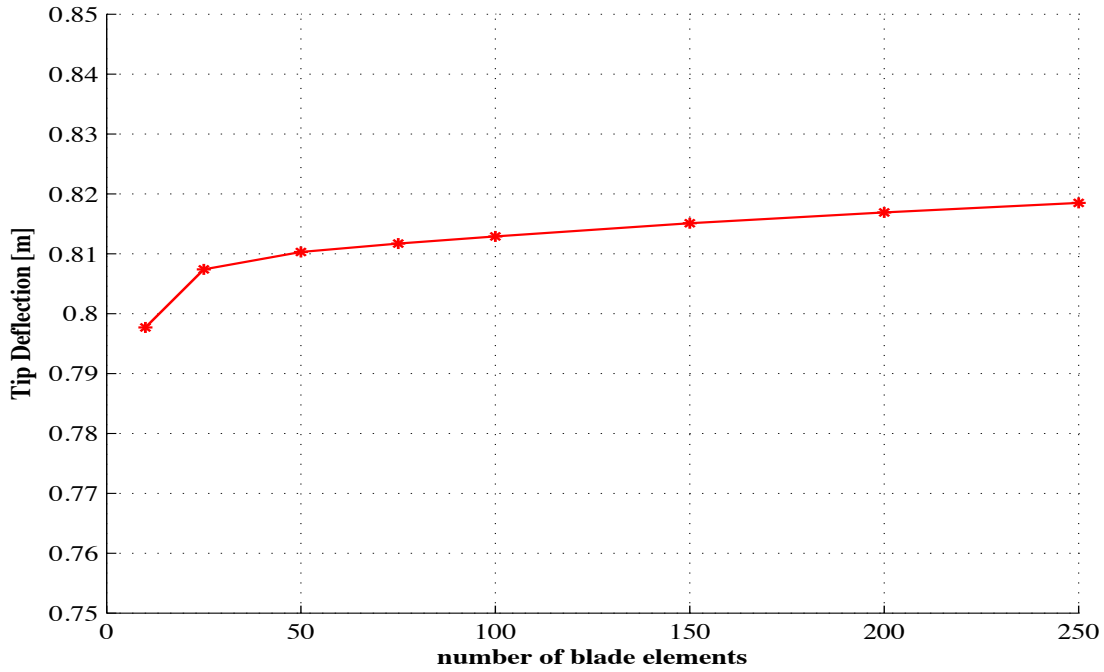

(b) Sensitivity of tip deflection to N_e, using prescribed wake vortex method blade loads

Figure 3.4: Prescribed wake vortex method sensitivity to number of blade elements at $C_T = 0.005$

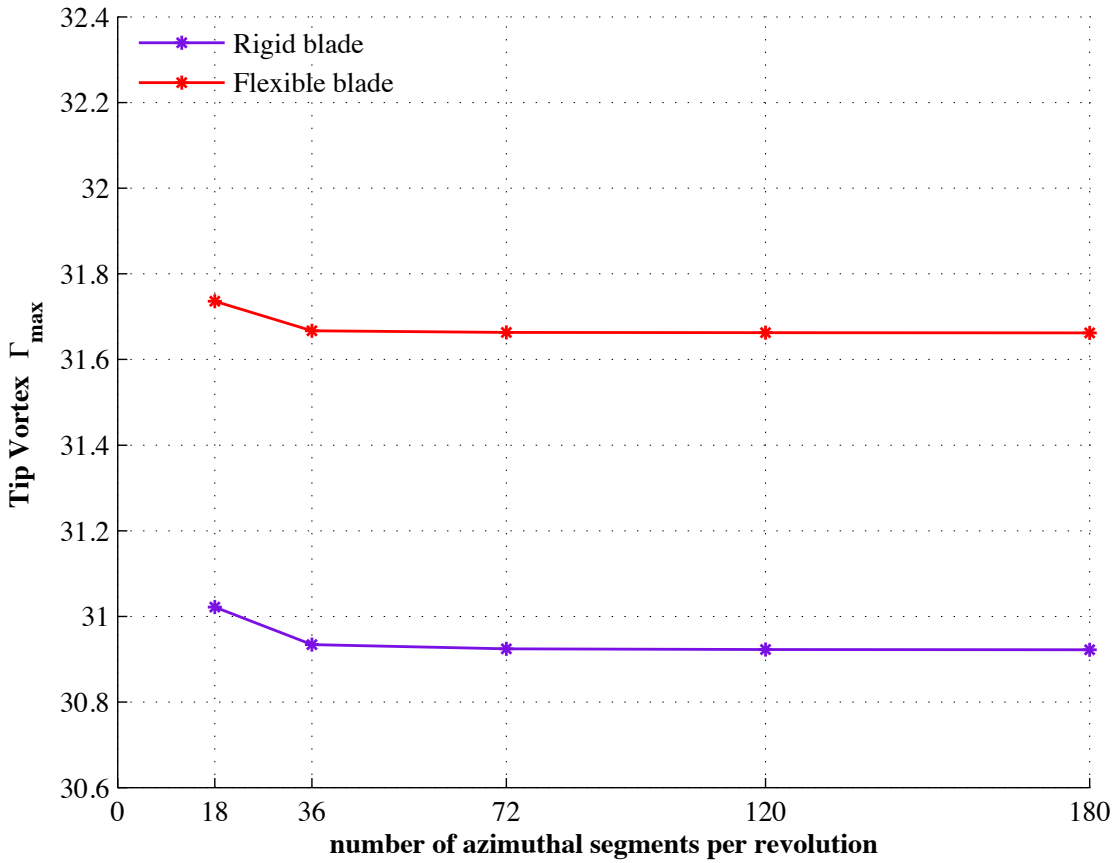

Figure 3.5: Vortex method sensitivity to number of straight line vortex segments per revolution at $C_T = 0.005$

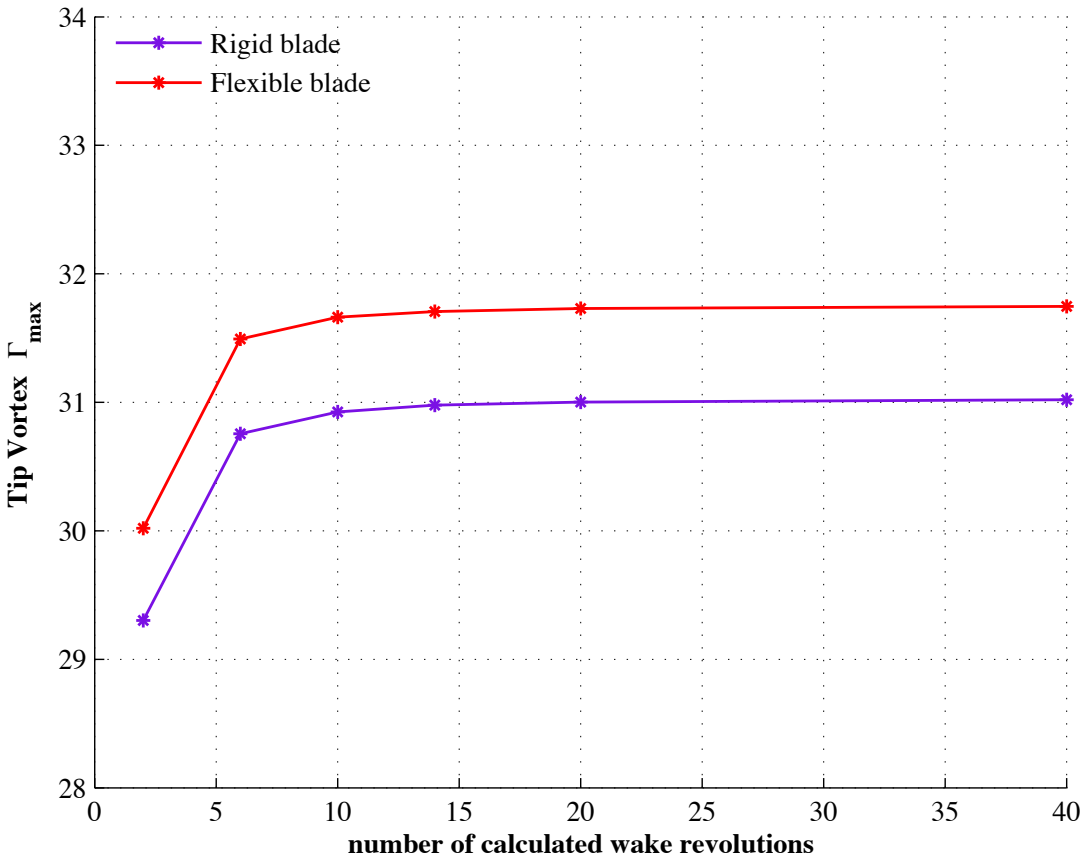

Figure 3.6: Vortex method sensitivity to number of calculated rotor revolutions at $C_T = 0.005$

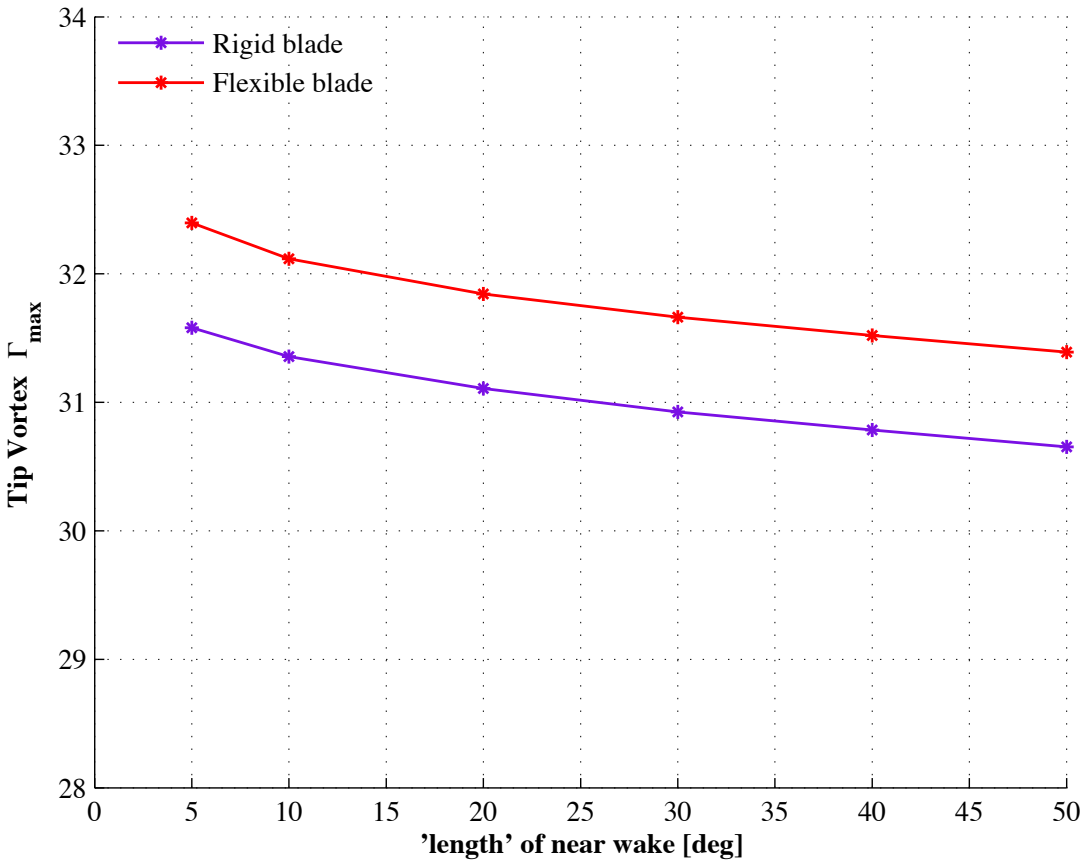

Figure 3.7: Vortex method sensitivity to 'lenght; of shed near wake at $C_T = 0.005$

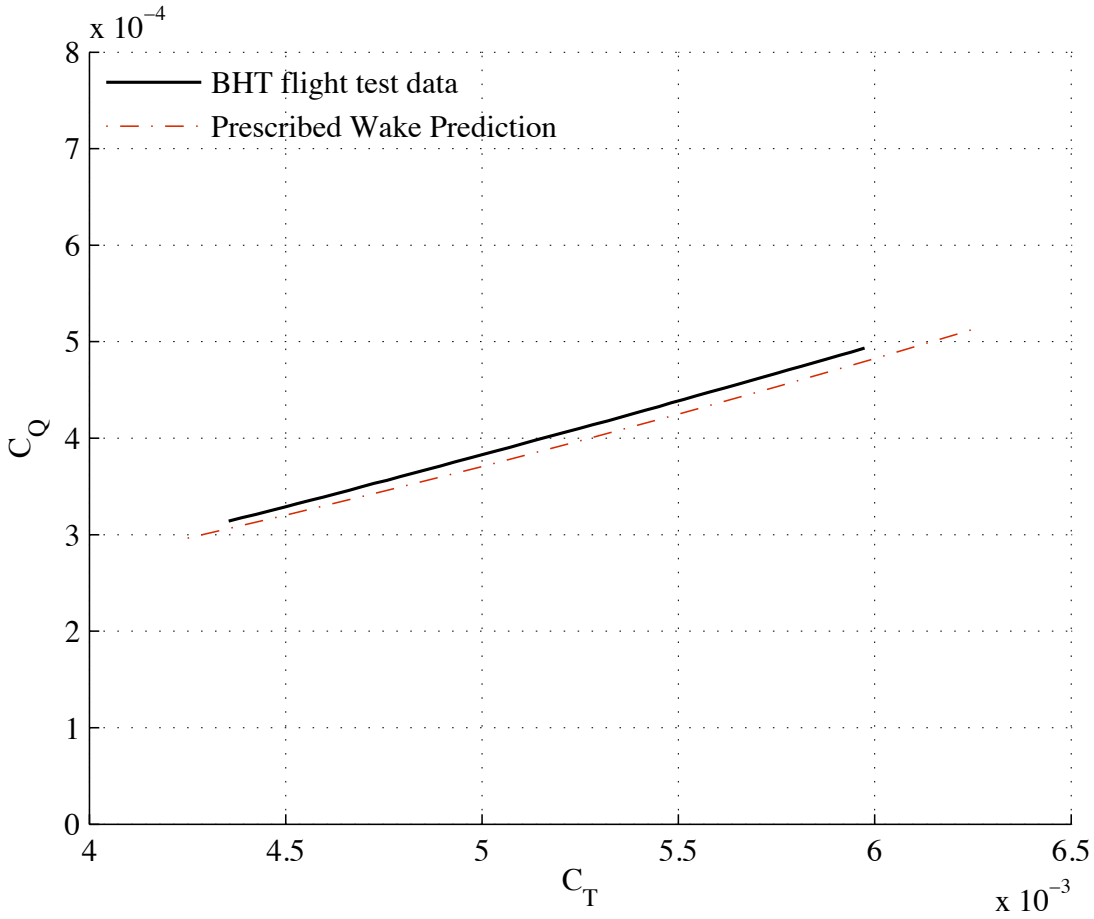

Figure 3.8: Prescribed wake vs experimental results for hover performance for an AH-1G Main rotor OGE

wake.

Once all required parameters were defined for sufficient convergence, validation out of ground effect for the prescribed wake method was carried out using the AH-1G rotor. Shown in Fig. 3.8, the comparison of power vs thrust results displays very good correlation between the current formulation and the experimental data.

3.2 Validation Using In-House Extreme Ground Effect Experiments

Two test set-ups were designed and carried out in-house as part of the HPH design study in extreme ground effect. Results from said experiments, detailed below, were used in carrying out the validations of the methods proposed in this work.

3.2.1 Ground Effect Experiments

Ground Effect Test Rig

The first experimental set-up used in this study (shown in Fig. 3.9) is a sub-scale rotor consisting of two fairly rigid, untwisted, untapered, uniform NACA0012 blades, 1.37 m in radius and 0.27 m in chord. Blade pitch and RPM were varied throughout testing, providing different thrust conditions, alongside variance of rotor height from the ground, focusing on the extremely low Z/R regime. Thrust and torque were measured for each setting using load and torque sensors respectively. For these settings, the rotor produces relatively low thrust values involving operational tip Reynolds numbers up to 200,000 at 80 RPM.

Resulting P_{IGE}/P_{OGE} ratios for constant thrust are shown in Fig. 3.10 for various height cases of this experimental set up. P_{IGE} and P_{OGE} respectively define rotor power in ground effect and out of ground effect. Significant power reductions, consistent with previous experiments (Fig. 1.6), are evident at low heights ($Z/R < 0.4$) in this plot. An averaged trend-line based on the newly generated test data from the rigid sub-scaled rotor was then compared to past results, in Fig. 3.11, and

(a) Full experimental set-up

(b) Sub-scale rigid test rotor

Figure 3.9: Sub scale ground effect test rig

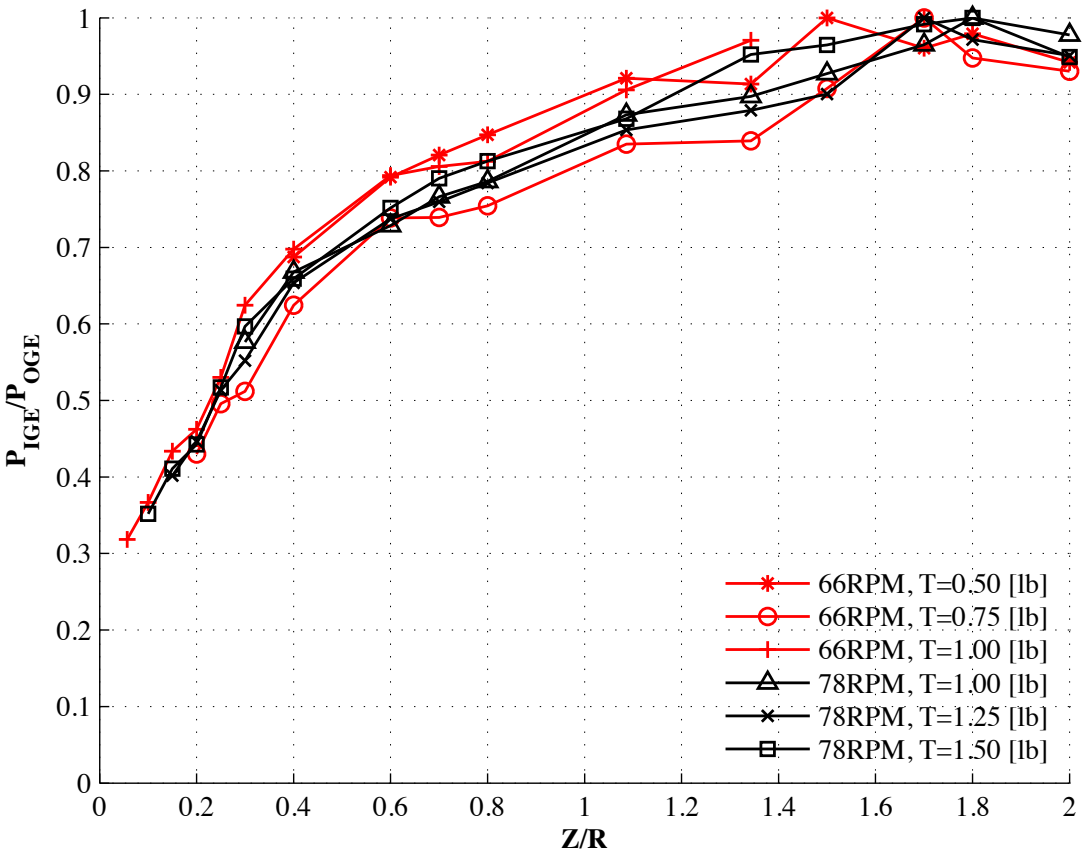

Figure 3.10: Sub scale test results showing total power ratio in ground effect for constant thrust

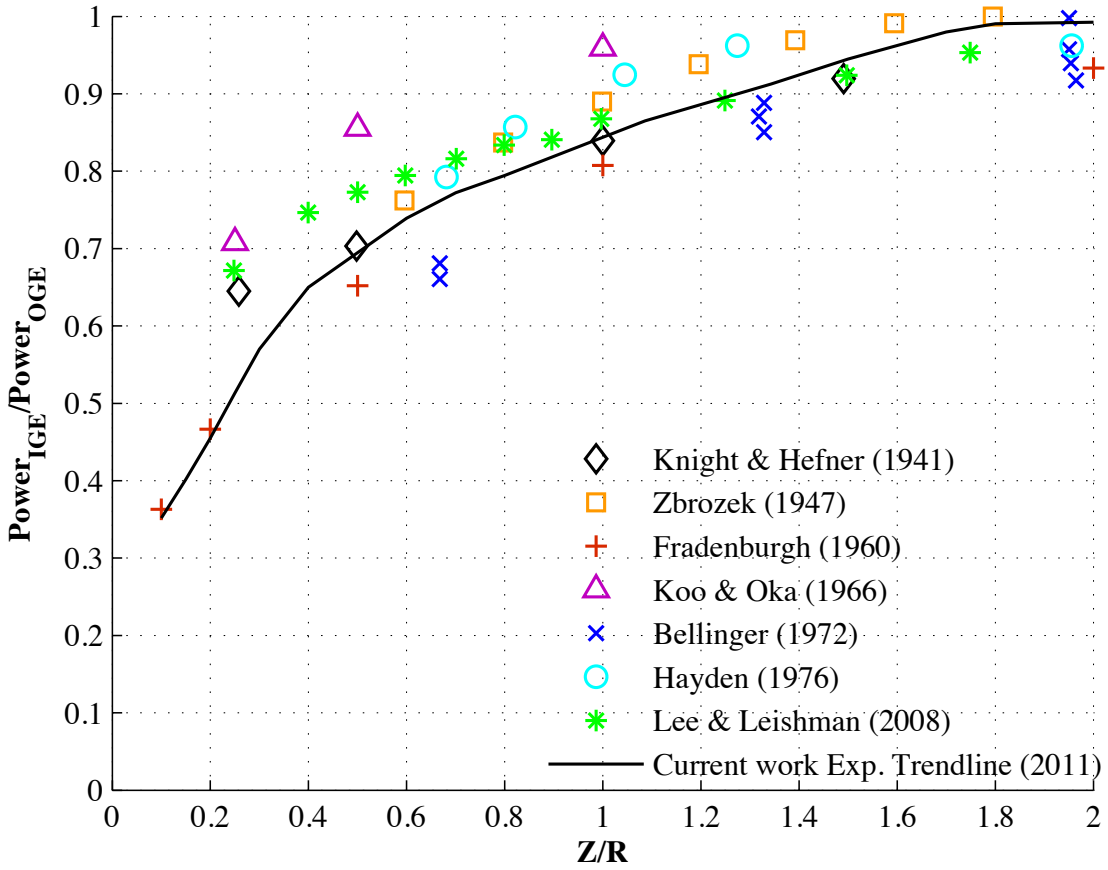

Figure 3.11: Sub-scale test ground effect trend-line vs previous experimental results

showed a good overall agreement. This new trend line, extracted from data ranging to the Z/R regime of interest, is later used as the BEMT ground effect model as formulated in Eq. (2.26).

HPH Blade Test Rig

A second in-house experiment featured a large rotor designed towards the full-scale quad-rotor configuration HPH mentioned in Section 1.1. In this design each rotor

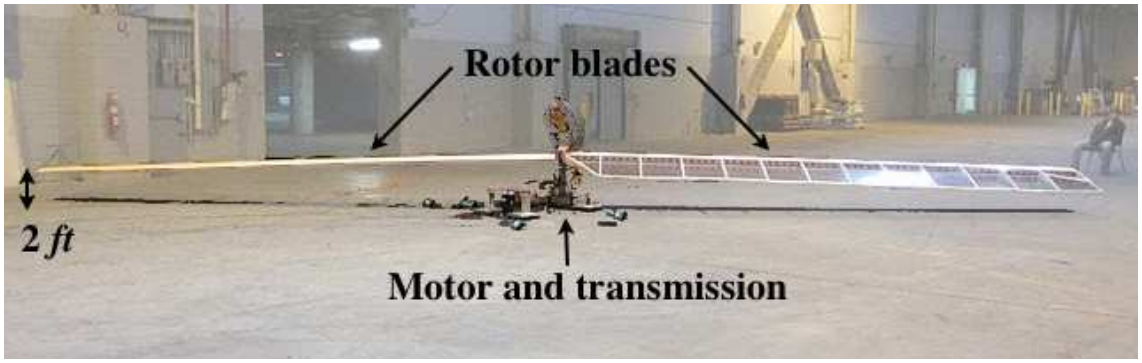

Figure 3.12: Full scale ground effect test rotor

consists of two ultra-lightweight, substantially flexible blades. The blade planform is untwisted and untapered, measuring 6.5 m in radius and 1.0 m in chord. These rotors were designed to operate in extremely low RPM ($10 \leq RPM \leq 20$) resulting in a tip Reynolds number range of $Re = 500,000 - 900,000$. The Eppler387 airfoil, designed for relatively low Reynolds number conditions [7], was selected for these blades. The test set-up was poised with the rotor hub at 0.6 m off the ground (seen in Fig. 3.12) as thrust and torque were measured for various settings of pitch and RPM. Tests were also carried out at 1.3 m for an evaluation of performance reduction due to height off ground for flexible blades. Representative results of data collected using this set-up at both heights are shown in Fig. 3.13.

While testing the flexible HPH blades high blade deflections were observed, approaching 1 m at the tip for the maximum tested load. These deflections represent $(Z/R)_{tip} to (Z/R)_{hub}$ ratios corresponding to Fig. 2.5 as such: With careful modeling, consideration of these deflections will prove to be key in successful prediction of this rotor's performance.

$$Z_{hub} = 130\ cm \quad \Rightarrow \quad (Z/R)_{hub} = 0.2 \quad \Rightarrow \quad (Z/R)_{tip} \approx 1.8(Z/R)_{hub}$$

$$Z_{hub} = 60\ cm \quad \Rightarrow \quad (Z/R)_{hub} = 0.1 \quad \Rightarrow \quad (Z/R)_{tip} \approx 2.5(Z/R)_{hub}$$

$$Z_{hub} = 30\ cm \quad \Rightarrow \quad (Z/R)_{hub} \approx 0.05 \quad \Rightarrow \quad (Z/R)_{tip} \approx 4(Z/R)_{hub}$$

Table 3.1: $(Z/R)_{tip}$ to $(Z/R)_{hub}$ ratios at various hub heights accounting for a 1 m tip deflection.

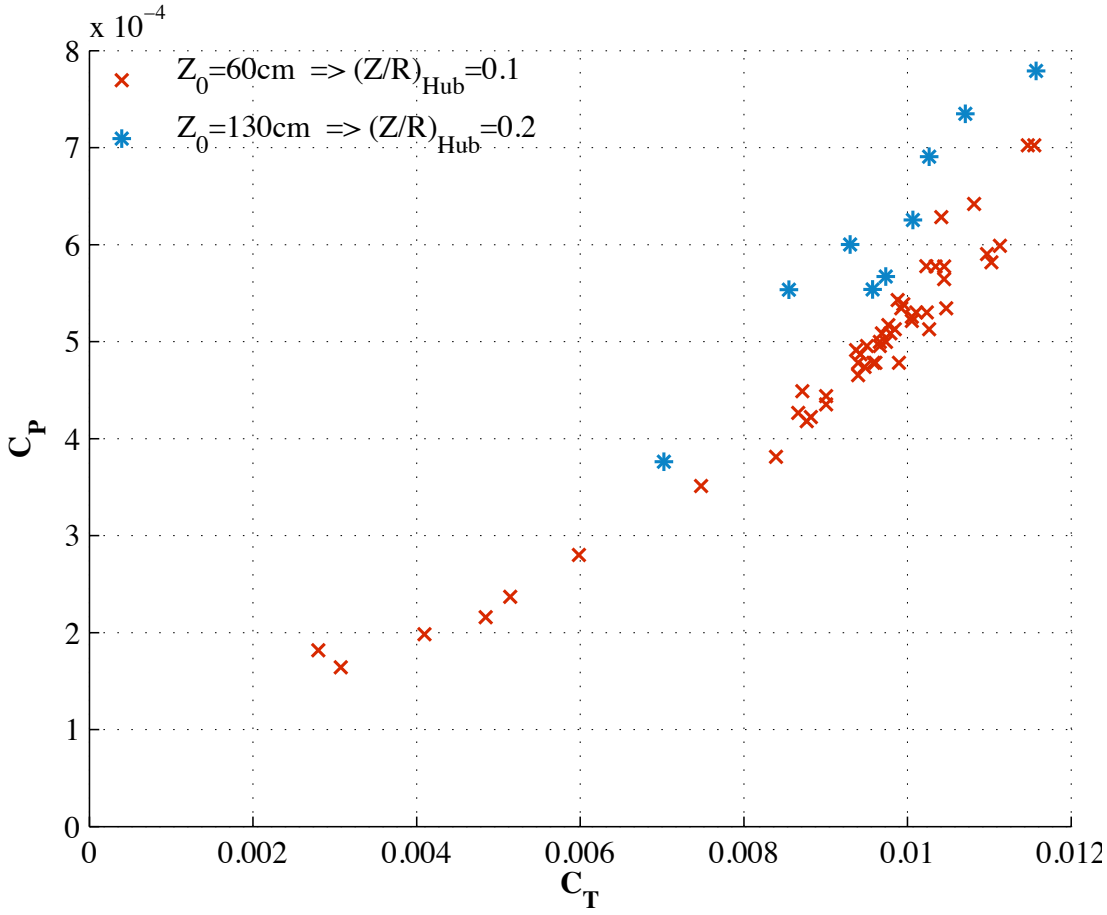

Figure 3.13: Total power coefficient variation with thrust coefficient, for a highly elastic rotor in ground effect, $14 \leq RPM \leq 18$.

3.2.2 BEMT Method In Ground Effect

Initial comparison of the BEMT formulation with the in-house test results was carried out using the rigid sub-scale rotor data at $Z/R = 2$, it's highest distance from the ground, simulating out of ground effect conditions. The test rig performance data was compared to calculations for 4 different operational RPM values. As seen in Fig. 3.14 the predictions correlate very well with the experimental results. Also demonstrated in this comparison is the importance of the empirical induced power factor at high thrust coefficients in obtaining good validation.

For the validation of this approach in extreme ground effect, the same experimental set up was used, this time comparing calculations to acquired data at $Z/R = 0.1$ in Fig. 3.15. The results, compared for the same four RPM values, present a decent agreement between calculation and measured power vs thrust. This comparison is expected to be of some discrepancy as the ground effect model, applied to inflow - **an induced effect** within BEMT, was extracted from these very experiments as a total power ratio - **a global effect**. Additional validation of the BEMT approach in ground effect using the sub-scale experimental set up is given in Figures 3.16 and 3.17 for the rotor non dimensional heights of $Z/R = 0.2$ and $Z/R = 0.5$ respectively.

For validation of the BEMT formulation in extreme ground effect for a flexible rotor, calculated results were compared to experimental data from the full scale UMD HPH rotor at $(Z/R)_{hub} = 0.1$ and 18 RPM. This comparison, shown in Fig. 3.18, includes BEMT predictions for performance of said rotor using a rigid

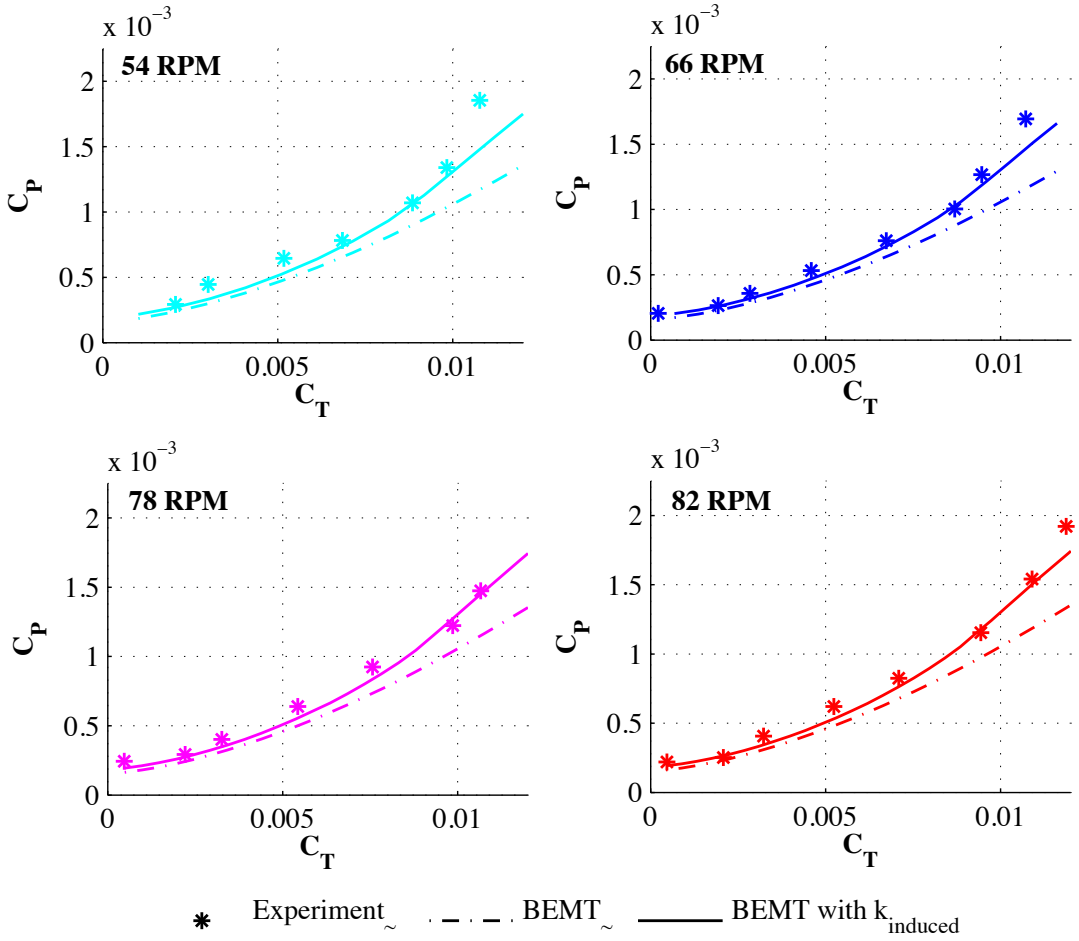

Figure 3.14: BEMT vs experimental results for the UMD sub-scale test at $Z/R = 2$

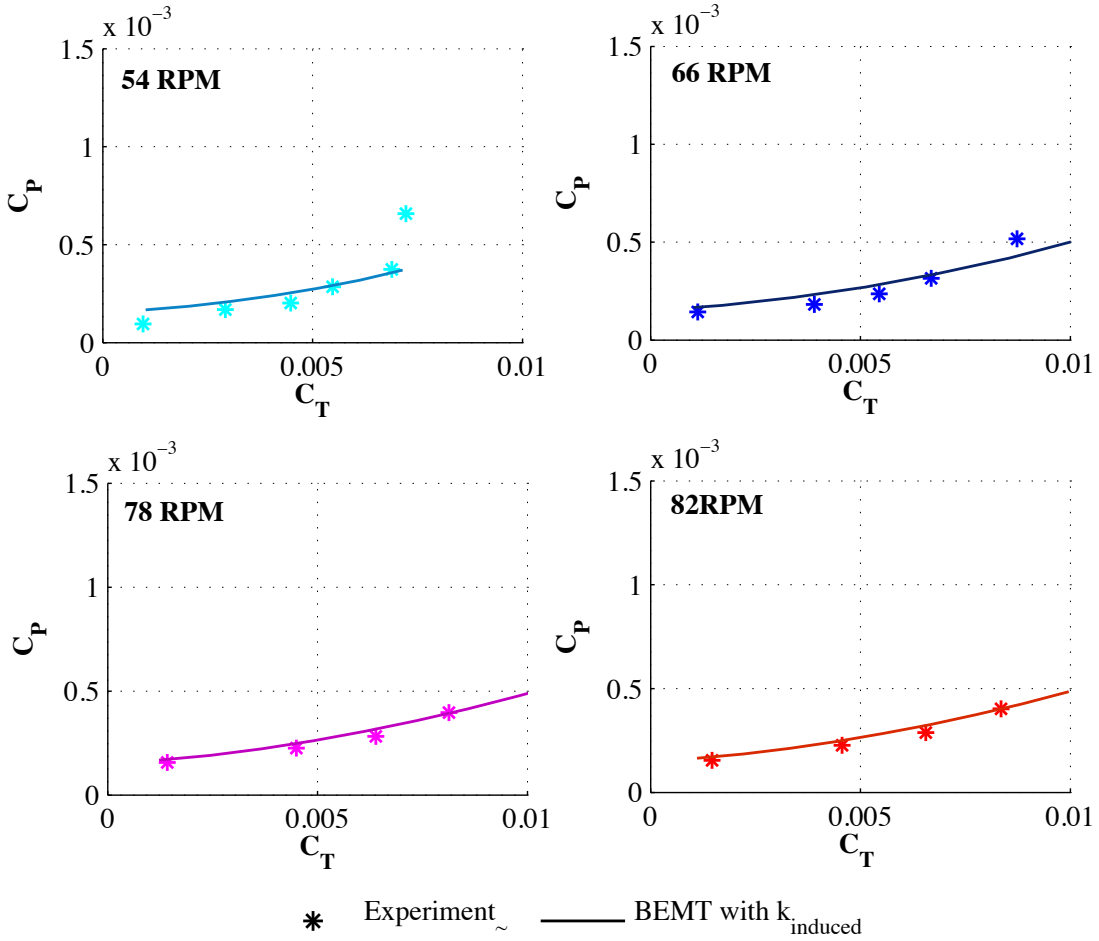

Figure 3.15: BEMT vs experimental results for the UMD sub-scale test at $Z/R = 0.1$

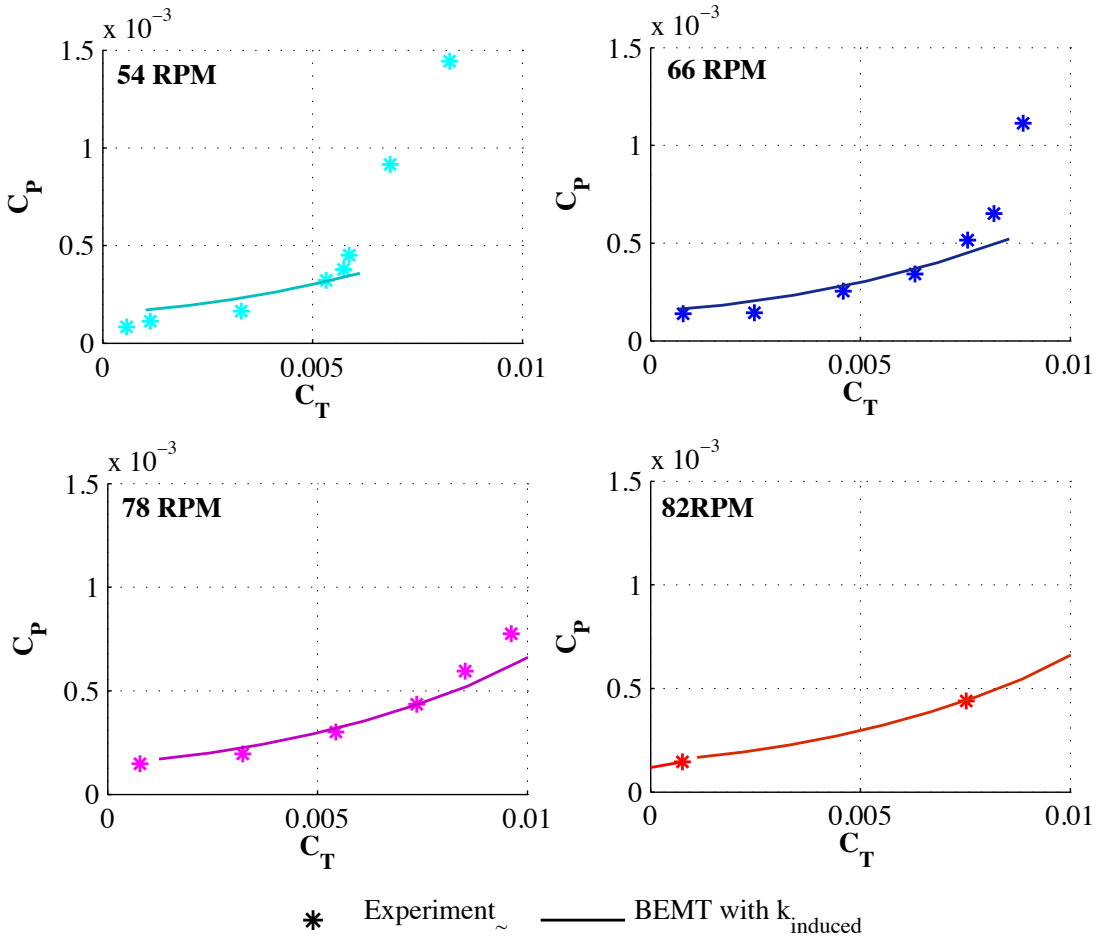

Figure 3.16: BEMT vs experimental results for the UMD sub-scale test at $Z/R = 0.2$

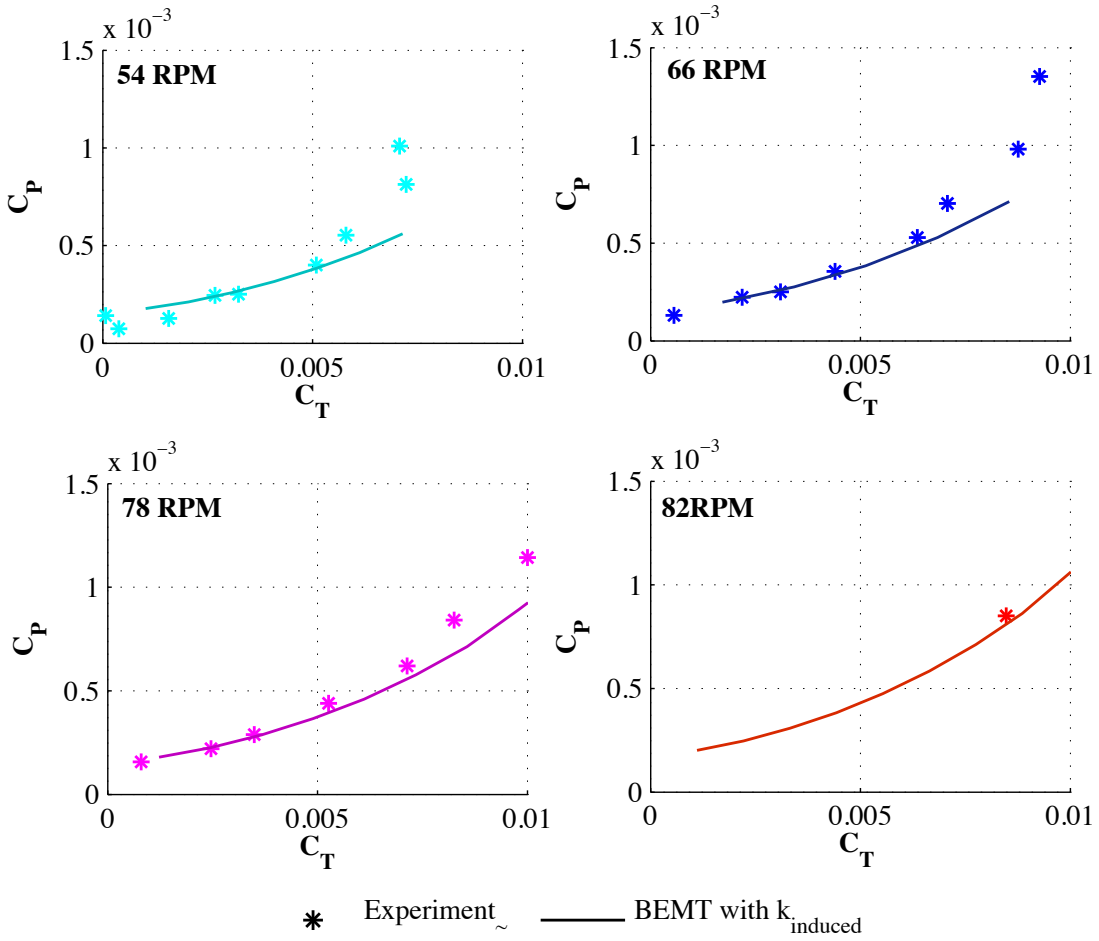

Figure 3.17: BEMT vs experimental results for the UMD sub-scale test at $Z/R = 0.5$

blade model and a flexible blade model (obtaining stiffnesses from static tests), with and without implementation of the induced power factor.

Results using global IGE modeling were also compared to the experimental results, where the OGE power results are factored for ground effect using the global P_{IGE}/P_{OGE} ratio (see Fig. 3.11) at a single height position for the whole rotor. Fig. 3.19 shows said results at the height points correlating with $(Z/R)_{hub} = 0.1$, as well as $(Z/R)_{75\%R}$ representing the elastic - deflected blade, alongside BEMT results. The global ground effect modeling method shows considerable under-prediction of the experimental power data, even when blade deflections are considered, thus supporting the approach of modeling ground effect on an elemental level. Figures 3.18 - 3.19 clearly show that accounting for elasticity, modeling the effect of ground vicinity on an elemental level, and the induced power factor implementation substantially improve the performance prediction under these conditions through out the C_T range. Similar results for the same rotor at a higher placement of $(Z/R)_{hub} = 0.2$ are also shown, in Fig. 3.20, for both BEMT IGE formulation and global IGE modeling, yielding similar conclusions.

3.2.3 Prescribed Wake Vortex Method In Ground Effect

Similarly to the BEMT validation, the prescribed wake model was also initially compared to the sub-scale experimental data at $Z/R = 2$. As this rotor height off the ground is still considered to be out of ground effect, this validation was done using the Kocurek and Tangler wake trajectory model [6] detailed in Equations (2.28) -

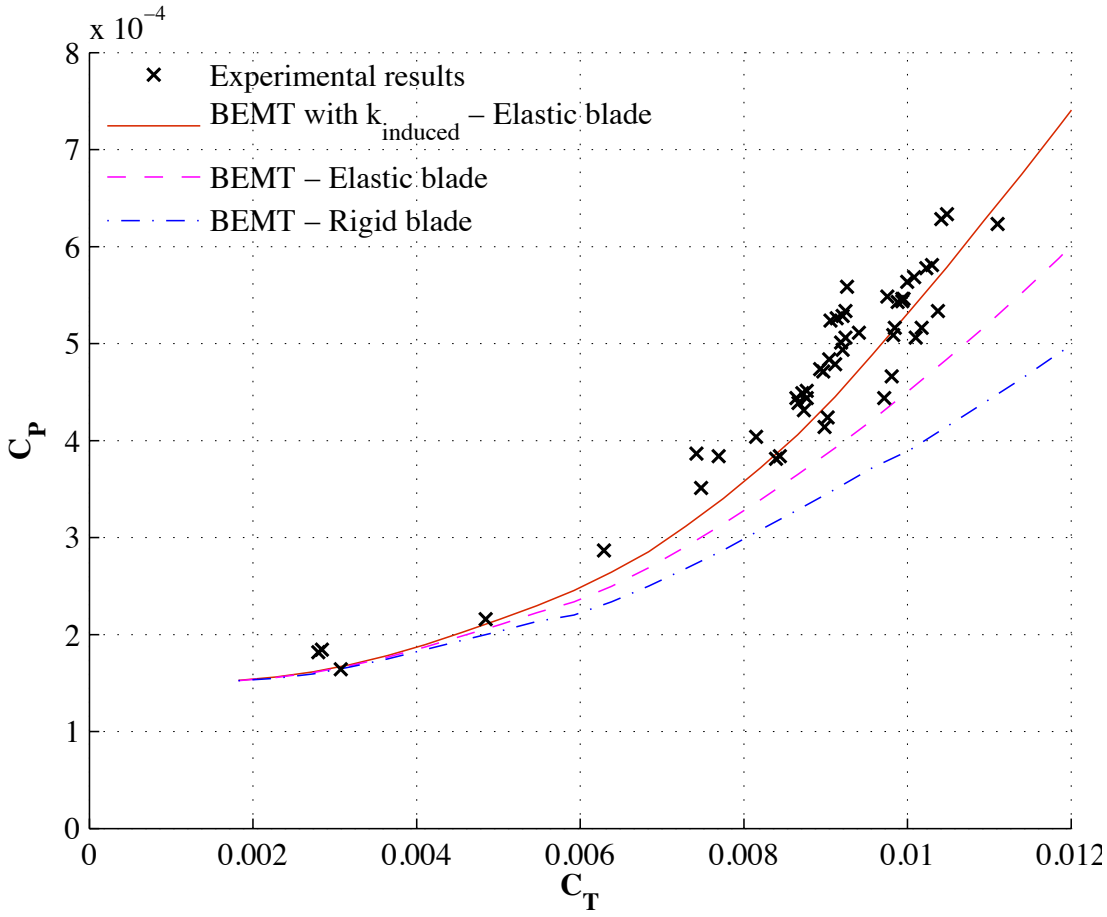

Figure 3.18: BEMT vs experimental results for the highly elastic full scale HPH rotor at $18RPM$ and $(Z/R)_{Hub} = 0.1$

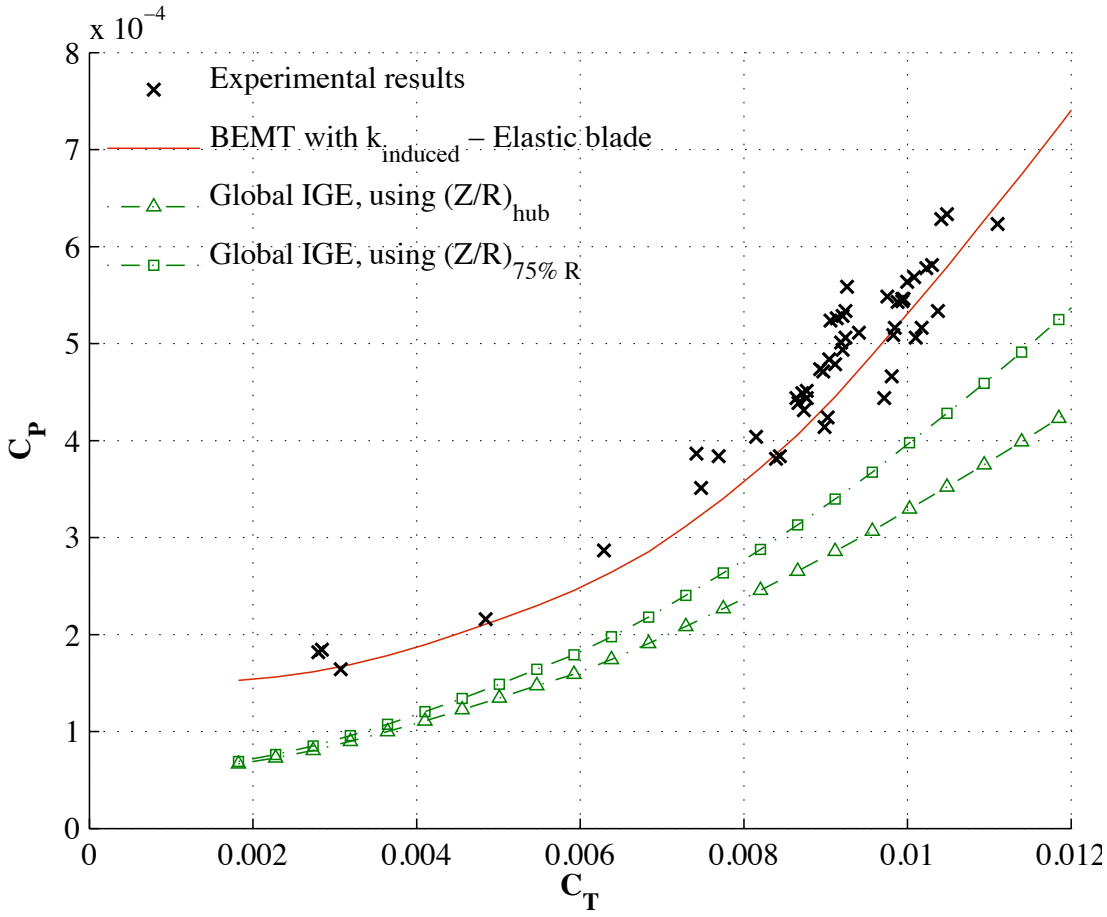

Figure 3.19: Global IGE vs experimental results for the highly elastic full scale HPH rotor at $18RPM$ and $(Z/R)_{Hub} = 0.1$

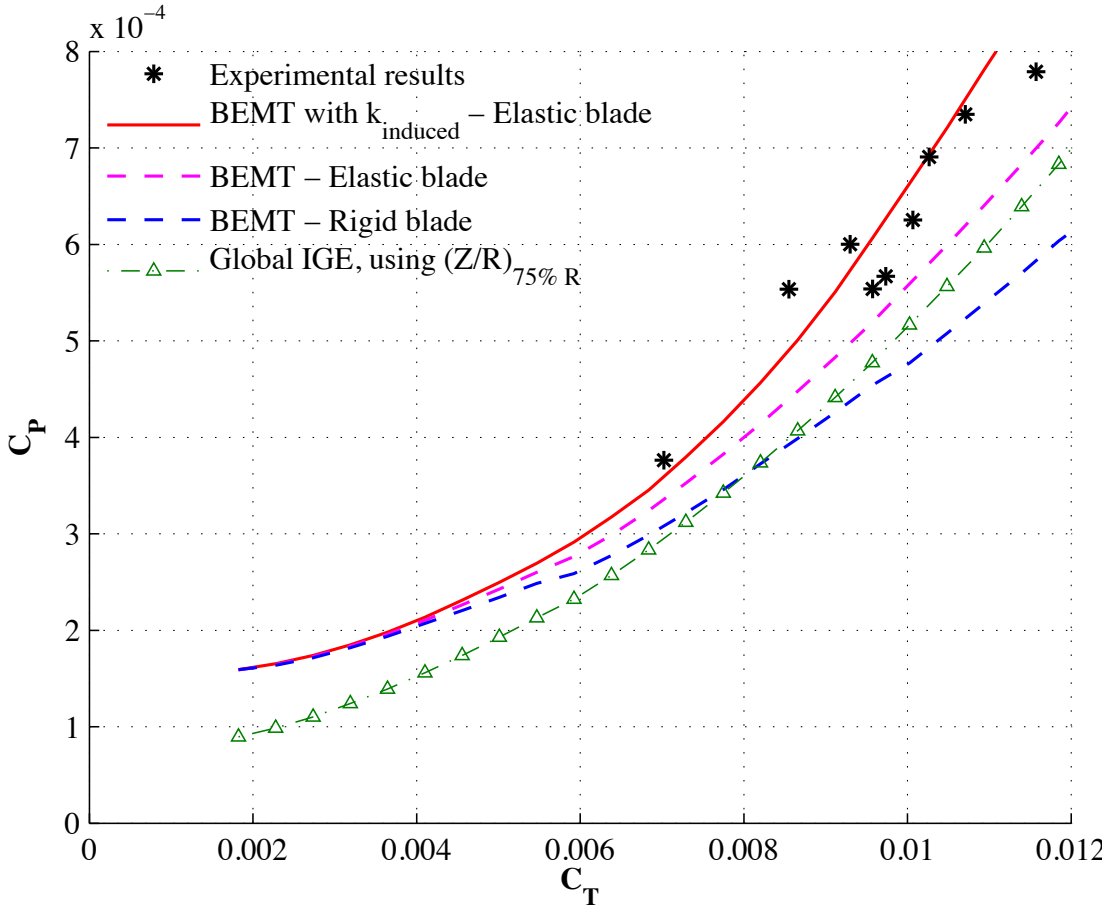

Figure 3.20: BEMT vs experimental results for the highly elastic full scale HPH rotor at $(Z/R)_{Hub} = 0.2$

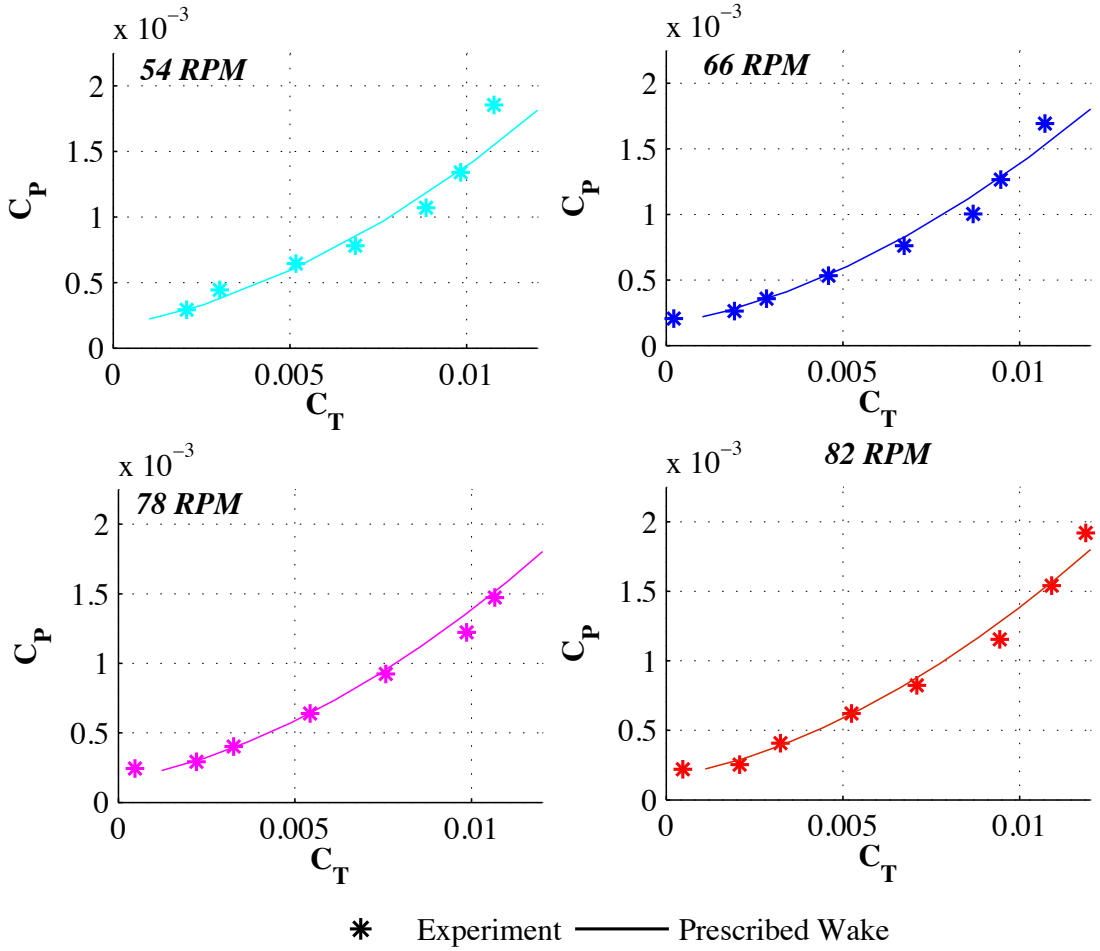

Figure 3.21: Prescribed wake vs experimental results for sub-scale test at $Z/R = 2$

(2.32). Presented in Fig. 3.21, this comparison shows good correlation.

The proposed prescribed wake trajectory model for extreme ground effect (detailed in Equations (2.44) - (2.45), was put to the test in a comparison using data from the sub-scale test set up. Computational results were compared to experimental results at RPM values as before at $Z/R = 0.1$. As seen in Fig. 3.22, the power prediction over the range of tested thrust cases showed an acceptable correlation, which is quite similar to the BEMT comparison in Fig. 3.15. Figures 3.23 and 3.24

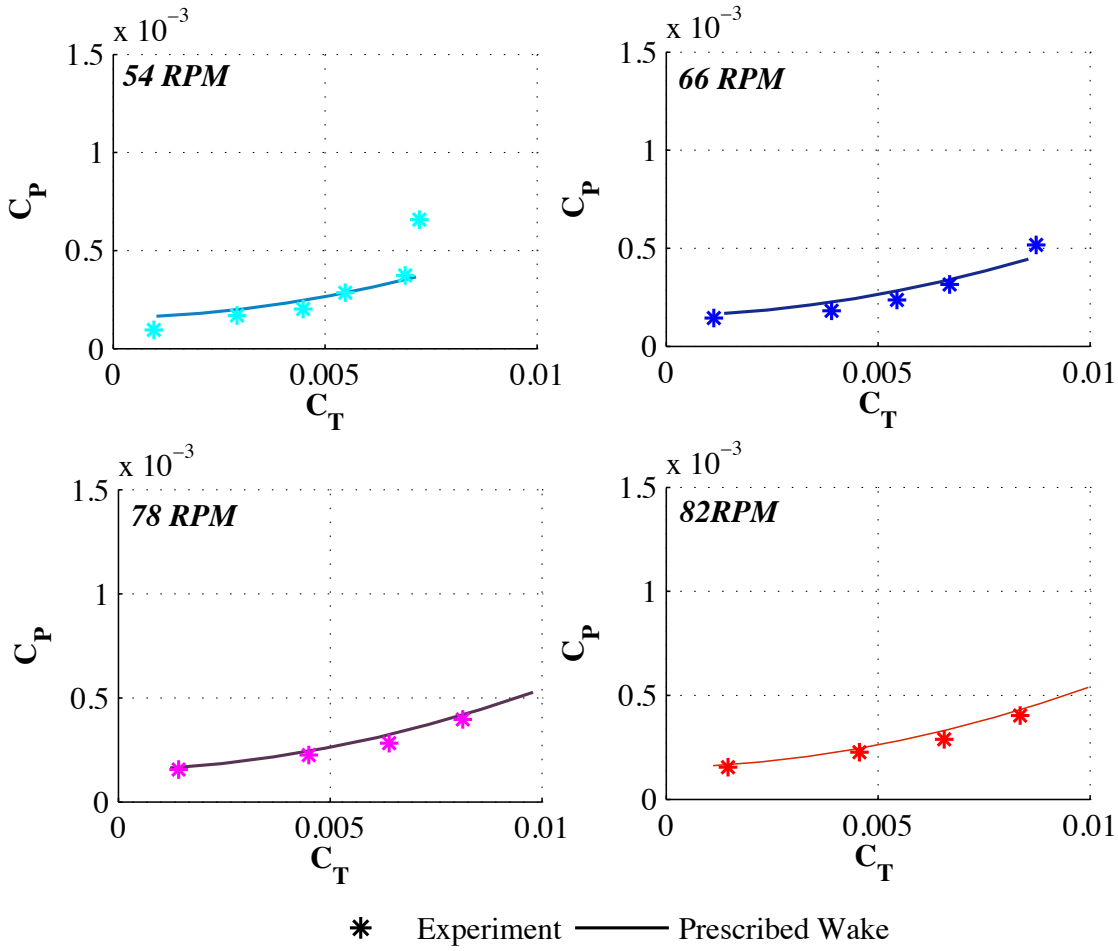

Figure 3.22: Prescribed wake vs experimental results IGE for the sub-scale test at $(Z/R)_{hub} = 0.1$

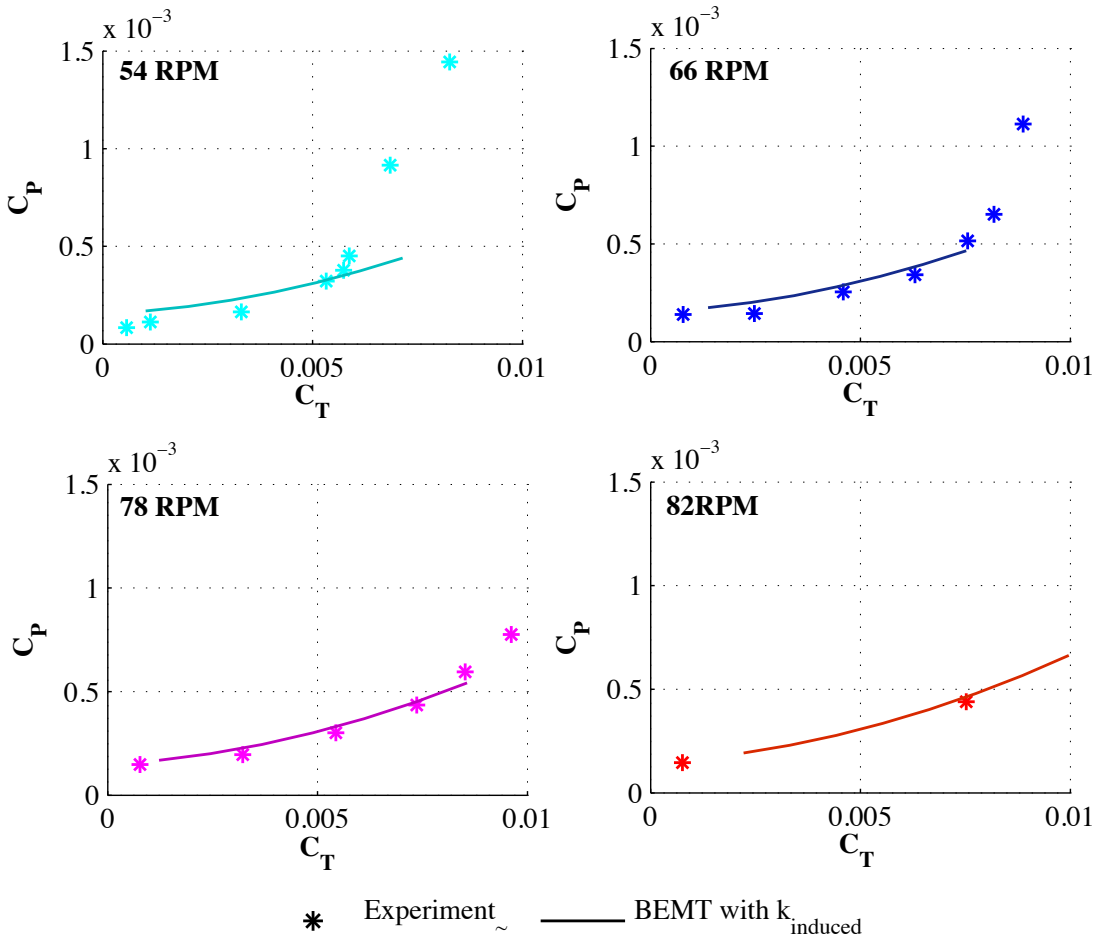

Figure 3.23: Prescribed wake vs experimental results IGE for the sub-scale test at $(Z/R)_{hub} = 0.2$

provide further validation of the prescribed wake in ground effect approach using the sub-scale experimental data at $Z/R = 0.2$ and $Z/R = 0.5$ respectively.

To provide a more general validation of the extreme ground effect wake trajectory at various Z/R settings, ratios of power in and out of ground effect, P_{IGE}/P_{OGE}, calculated using the prescribed wake IGE method, were examined within the range of $Z/R \leq 0.5$. Compared to experimental results by Fradenburgh [60] for $C_T/\sigma = 0.06$, and to the model extracted using the sub scale test set-up (fully shown in Fig. 3.11),

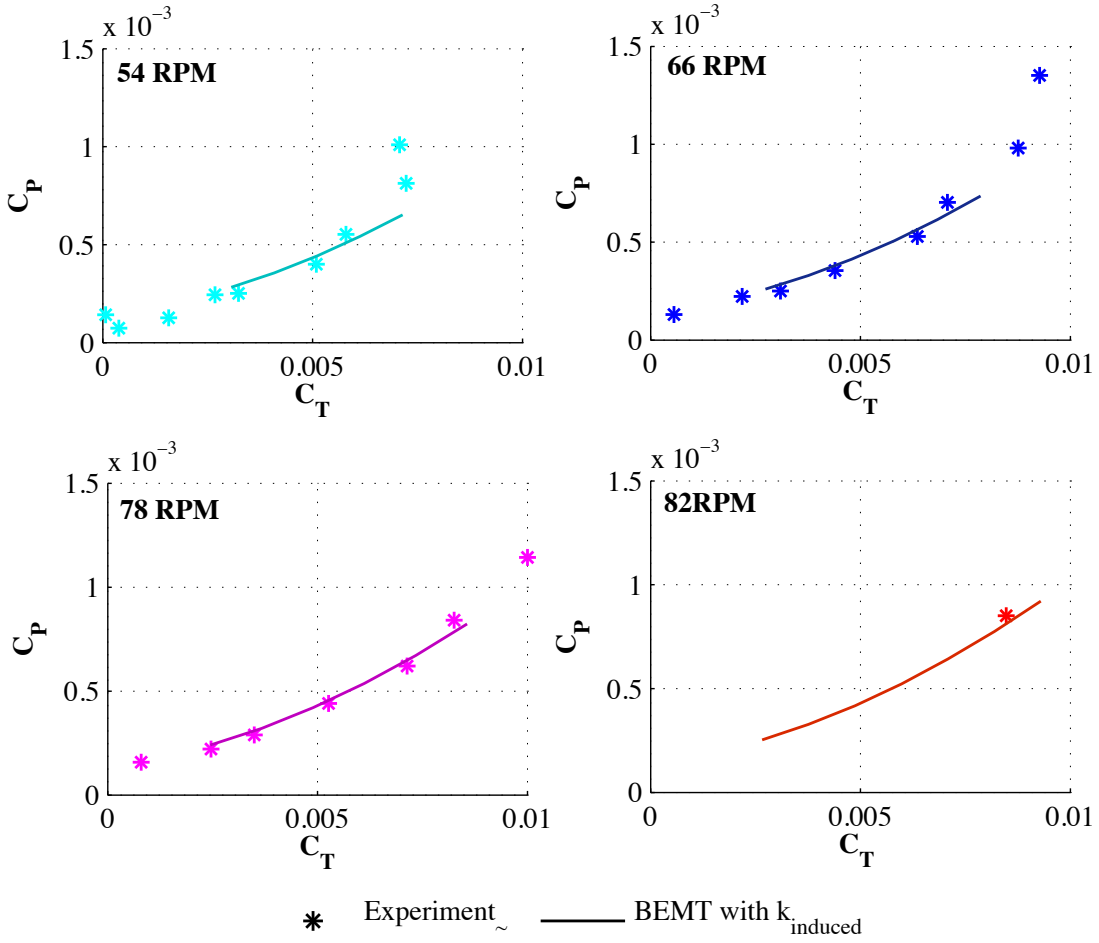

Figure 3.24: Prescribed wake vs experimental results IGE for the sub-scale test at $(Z/R)_{hub} = 0.5$

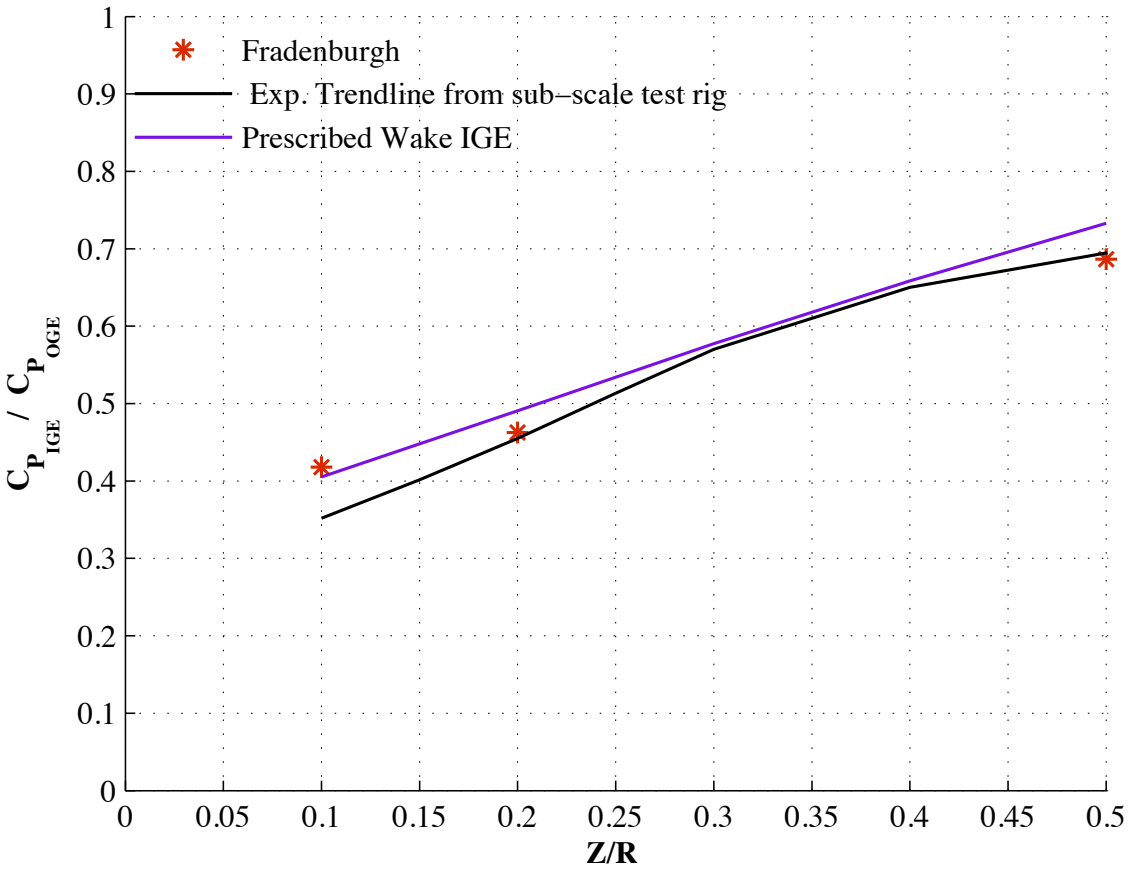

Figure 3.25: Total power ratio IGE for constant thrust - prescribed wake vs experimental results

the new in ground effect prescribed trajectory is shown to capture power savings due to ground vicinity quite well.

Further, validations of the extreme ground effect trajectory model, including effects of flexibility, were achieved when comparing them to experimental data from our full scale, highly flexible, rotor test set-up for two different heights off ground. Fig. 3.26 presents experimental results for $(Z/R)_{hub} = 0.1$ at 18 RPM against computational results for both rigid and flexible blade modeling assumptions. The

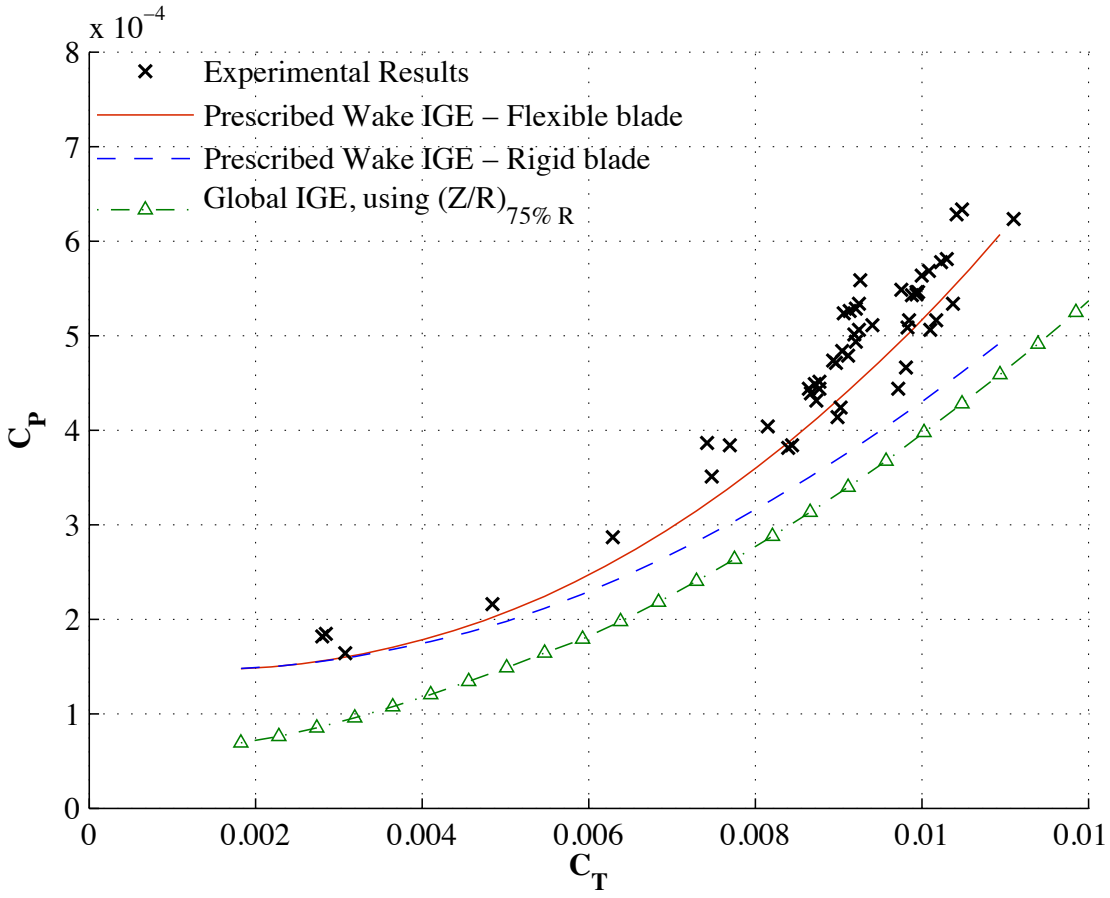

Figure 3.26: Prescribed wake vs experimental results IGE for the full scale rotor at $(Z/R)_{hub} = 0.1$

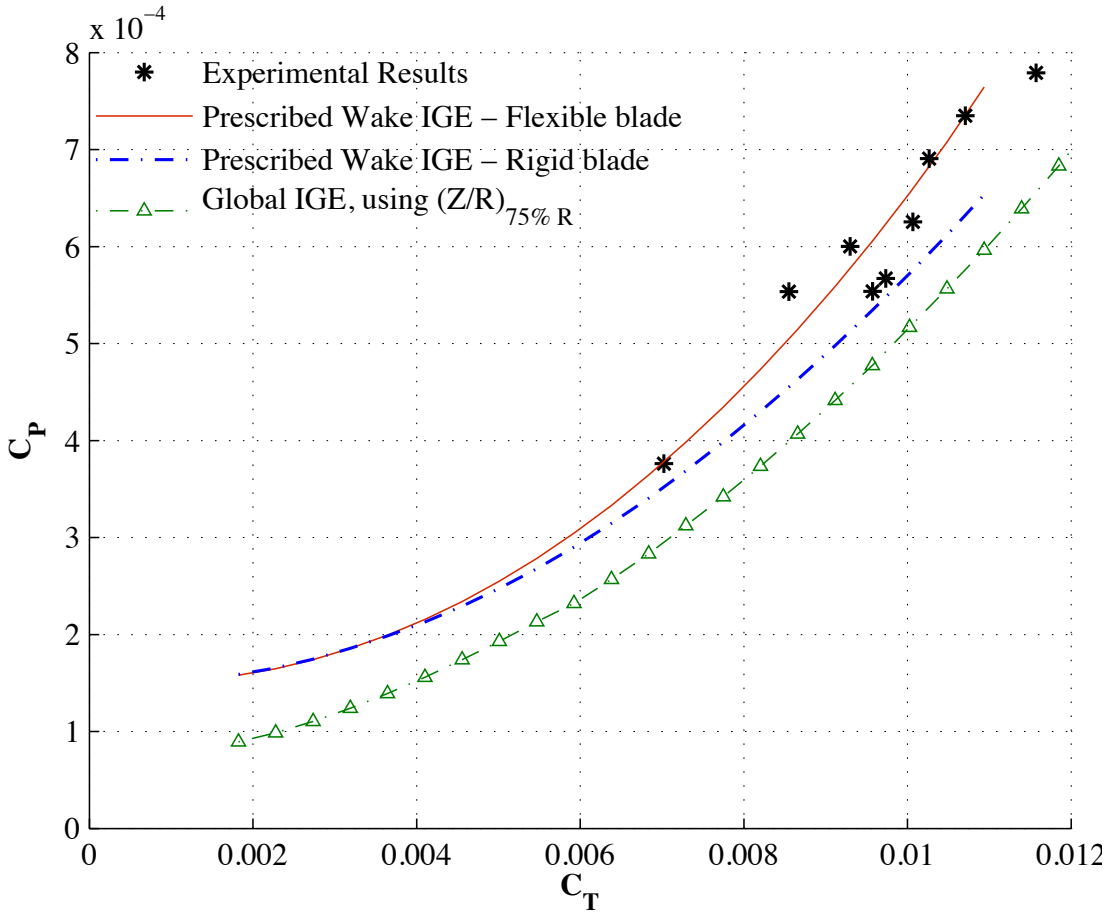

Figure 3.27: Prescribed wake vs experimental results IGE for the full scale rotor at $(Z/R)_{hub} = 0.2$

comparison clearly conveys an improved correlation to test results when accounting for blade flexibility, especially at high thrust levels. Fig. 3.26 also shows the global IGE curve, once again demonstrating substantial under-prediction of the experimental power data. It can be easily concluded from this comparison that predictive quality is significantly increased by considering the effect of $Z(\tilde{r})/R$ distribution caused by substantial blade deflections in ground effect.

A similar comparison between experimental results and the computational re-

sults is shown in Fig. 3.27 for the same experimental set up at the height of 130 cm ($(Z/R)_{hub} = 0.2$). Here too, a poor under-predicting correlation is observed when using global implementation of empirical power ratio factors. However, similarly to the previous case, a very good agreement is shown between the test data and the prescribed wake model, once again showing improved agreement using the flexible blade model. Since it is recognized that the new wake trajectory is of substantially different geometric behavior than the original out of ground effect trajectories, sensitivity to number of calculated wake revolutions was re-examined, ensuring that calculating for 10 rotor revolutions is definitely sufficient for a converged result.

Additionally, the wake sensitivity to trajectory shapes was examined, looking into two principle variations. The first variation considered, is a vertical displacement throughout the wake trajectory, causing the tip vortices to descend more towards the ground, relative to the baseline shape. The prescribed wake method in ground effect was showed relatively minor sensitivity to this variation in trajectory, resulting in an approximate 7% difference in required power. The second variation is a change in curvature only, while keeping the final vortex trajectory height above ground similar to the baseline shape. This variation showed negligible effect on the resulting power requirements, which differed from the baseline trajectory results by less than 1%. Figure 3.28 shows examples for the wake shape variations, alongside the respective power differences, demonstrating the slight to negligible sensitivity to small changes in wake geometry.

Finally, the resulting effect of the prescribed wake on the trailed tip vortex was studied, in an attempt to verify that the induced velocities at the trailed wake

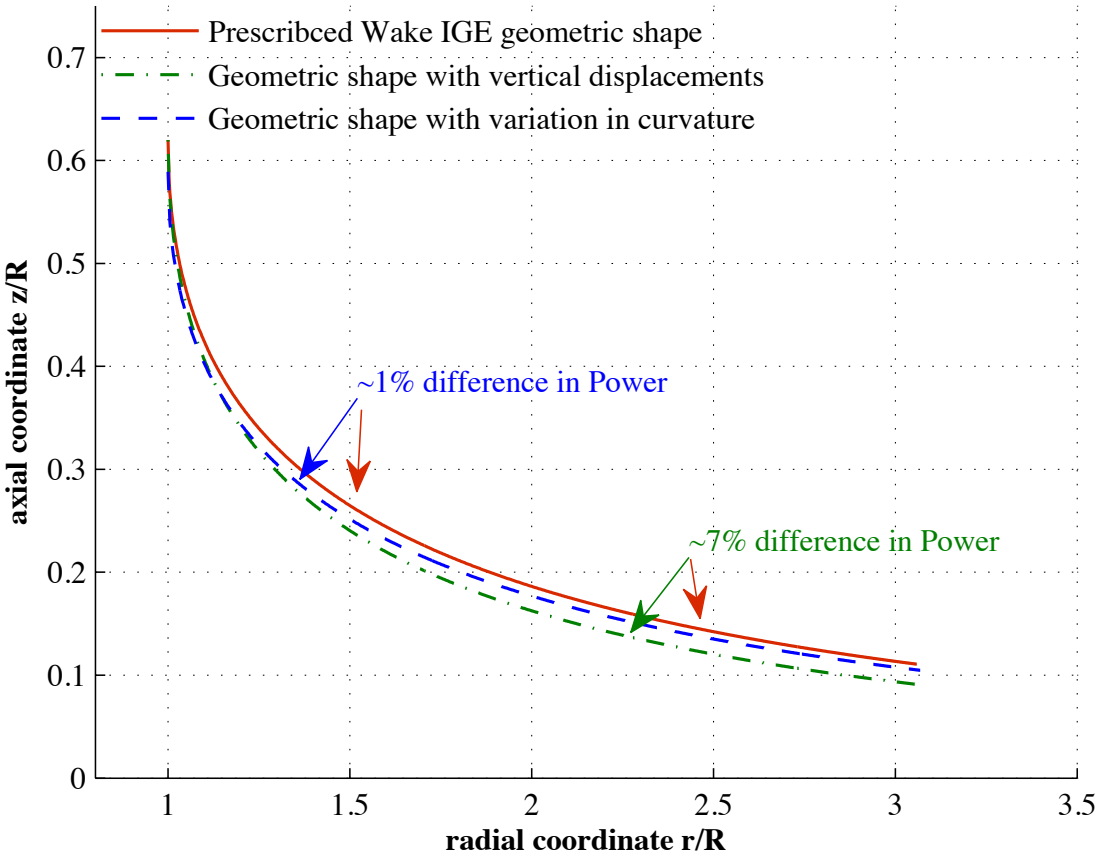

Figure 3.28: Variation in trajectory shapes and their effect on power at $Z/R = 0.62$

vortices immediately below the rotor plane are indeed mostly in the vertical direction. This behavior, known to be true for a common rotor hovering out of ground effect, was assumed to also be valid for this unique case of a highly flexible rotor in extreme ground effect, as discussed in Section 2.3.2). To address this matter, induced velocities were calculated at circular cross sections of the prescribed wake geometry - at various heights below the tip path plane. The radial coordinates defining the circle radius correlate with the trailed tip vortex coordinates at each height. The resulting velocity distributions were averaged around the azimuth for each height, and normalized by blade tip speed ΩR, obtaining a value for average radial inflow and average vertical inflow at each trajectory cross section. As can be seen in Fig. 3.29 for the reference case of $(Z/R)_{hub} = 0.1$, $18RPM$, and $T = 50lbs$, the average vertical inflow is substantially larger than the average radial inflow for all examined heights, validating said assumption. Furthermore, this examination supports the assumption that prescribed wake results should not differ largely from results calculated using a free vortex methodology, and therefore the prescribed wake method provides a sufficient approximation in describing the rotor wake.

3.3 Detailed Comparison of the BEMT and Prescribed Wake Methods In Extreme Ground Effect

Both proposed approaches for prediction of rotor performance in extreme ground effect have demonstrated very good correlation with the same sets of experimental results for global power in extreme ground effect, for both the rigid rotor

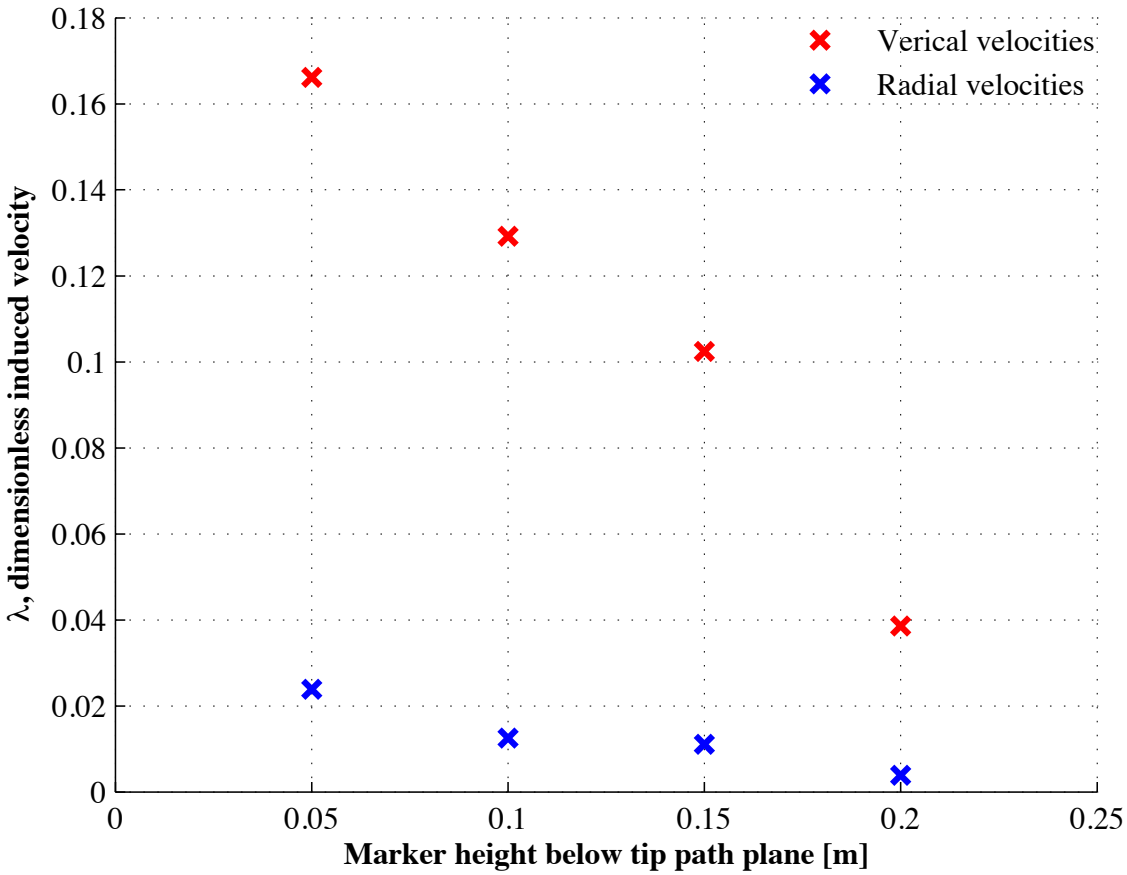

Figure 3.29: Induced velocities at various cross sections of trailed wake below tip path plane, full scale flexible rotor at $(Z/R)_{hub} = 0.1$

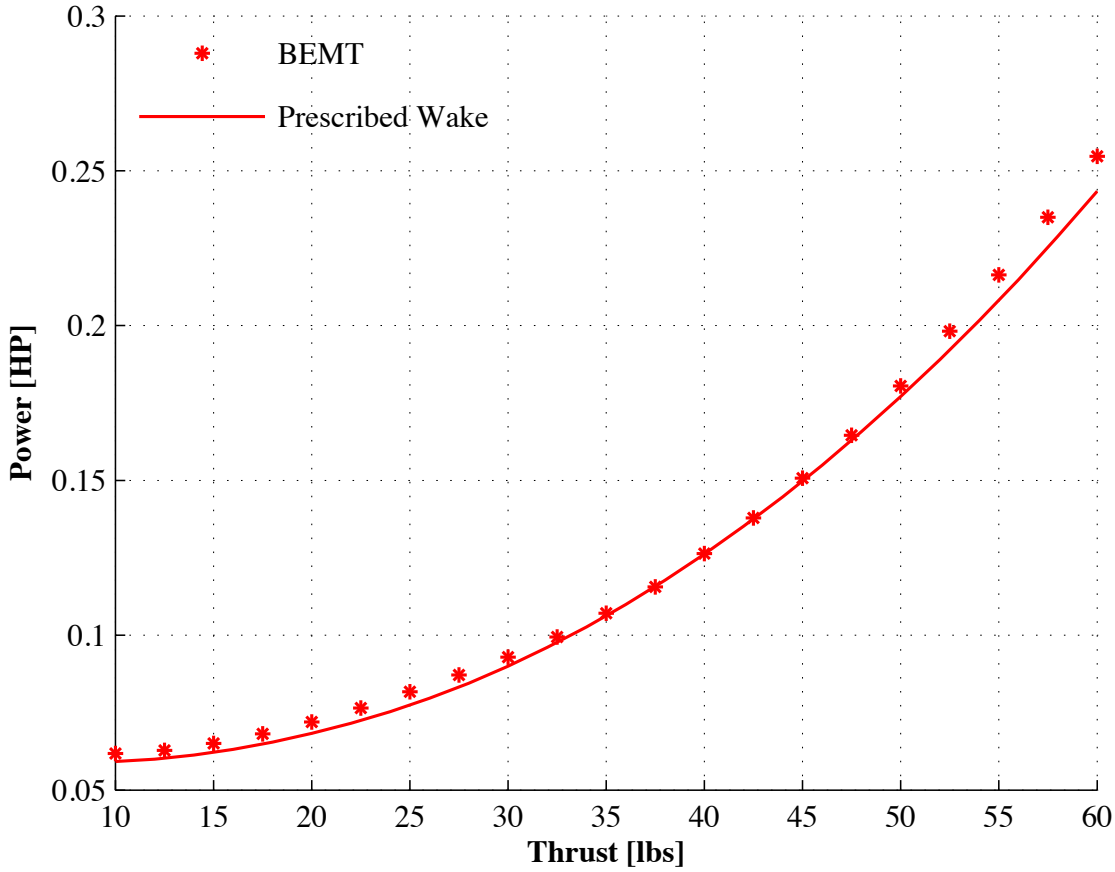

Figure 3.30: Power vs Thrust, full scale rotor at $(Z/R)_{hub} = 0.1$ and $18RPM$

cases (Figures 3.15- 3.16, and 3.22- 3.23), and the flexible HPH rotor cases (Figures 3.18, 3.20, and 3.26- 3.27), and therefore are expected to show correlation of the same quality when compared with each other. Fig. 3.30 shows the expected correspondence in predicted power results at varying thrust, for the flexible HPH rotor model operating at $(Z/R)_{hub} = 0.1$ and $18RPM$.

For further understanding of the successful correlation between results using the two inherently different inflow models, radial distributions of various properties

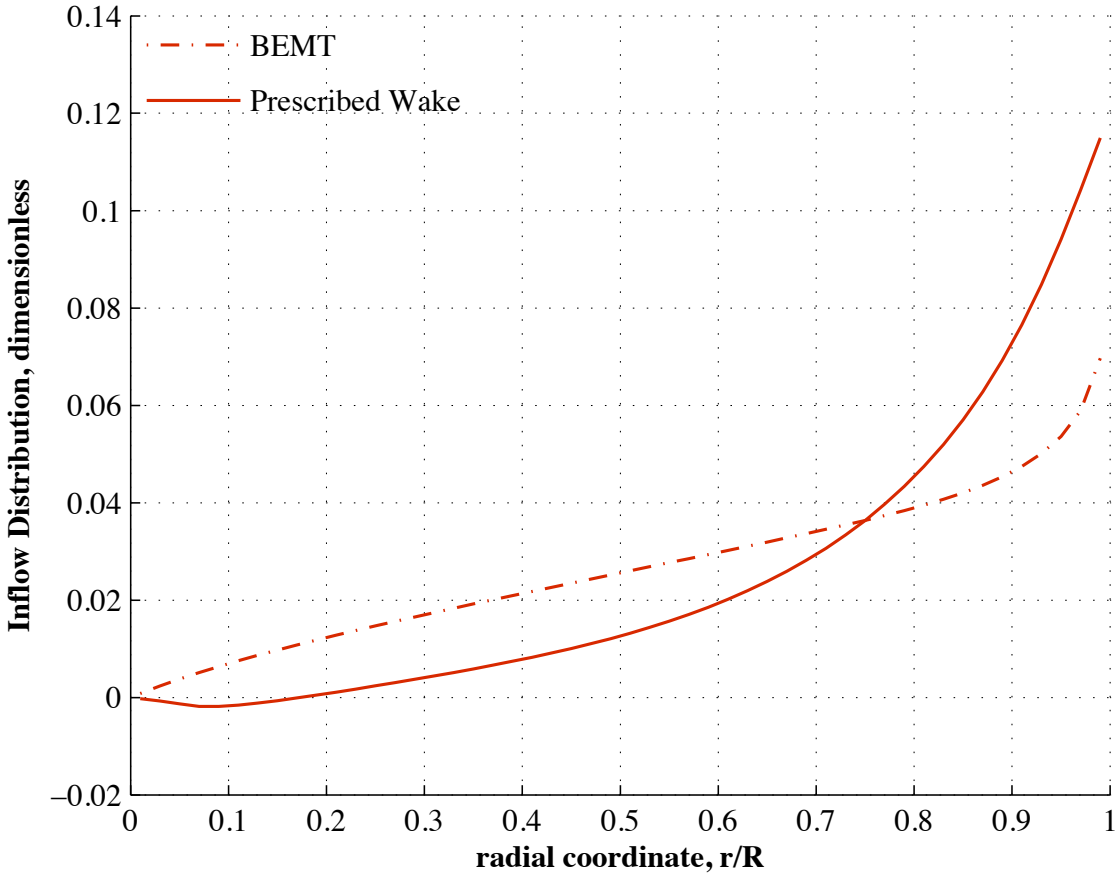

Figure 3.31: Inflow distribution along blade, full scale rotor at $T = 50lbs$, $(Z/R)_{hub} = 0.1$ and $18RPM$.

were examined, at the reference operational point of $T = 50lbs$. Shown in Fig. 3.31 are inflow distributions using both the BEMT IGE inflow model and the prescribed wake IGE model coupled with a mirror image wake representing ground conditions. The two distributions, although within a similar range of values, show different trends stemming from the two very different inflow models, ground models, and calculation processes. These, in turn, are expected to lead to a difference in thrust loading distributions along the blade. Fig. 3.32 confirms said expectation, compar-

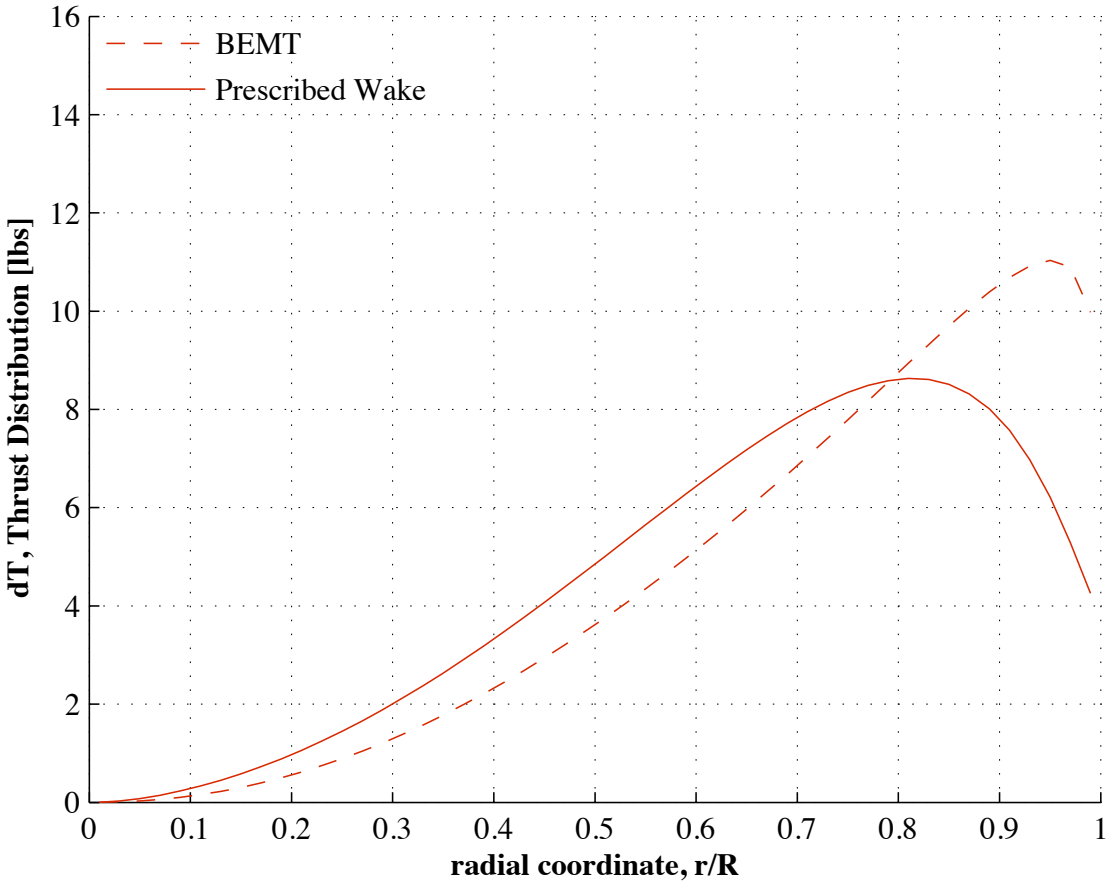

Figure 3.32: Thrust distribution along blade, full scale rotor at $T = 50lbs$, $(Z/R)_{hub} = 0.1$ and $18RPM$.

ing the two resultant thrust distributions. However, as both methods are required to converge for the same total thrust value (trimmed for the same C_T), both distributions are forced to result in the same value when integrated along the blade. And so, as the prescribed wake thrust distribution holds higher values for most inner sections of the blade, the BEMT distribution shows substantially higher values at the blade tip - evenning out the differences when integrating.

Further noting, the difference in the load distribution along the radius directly

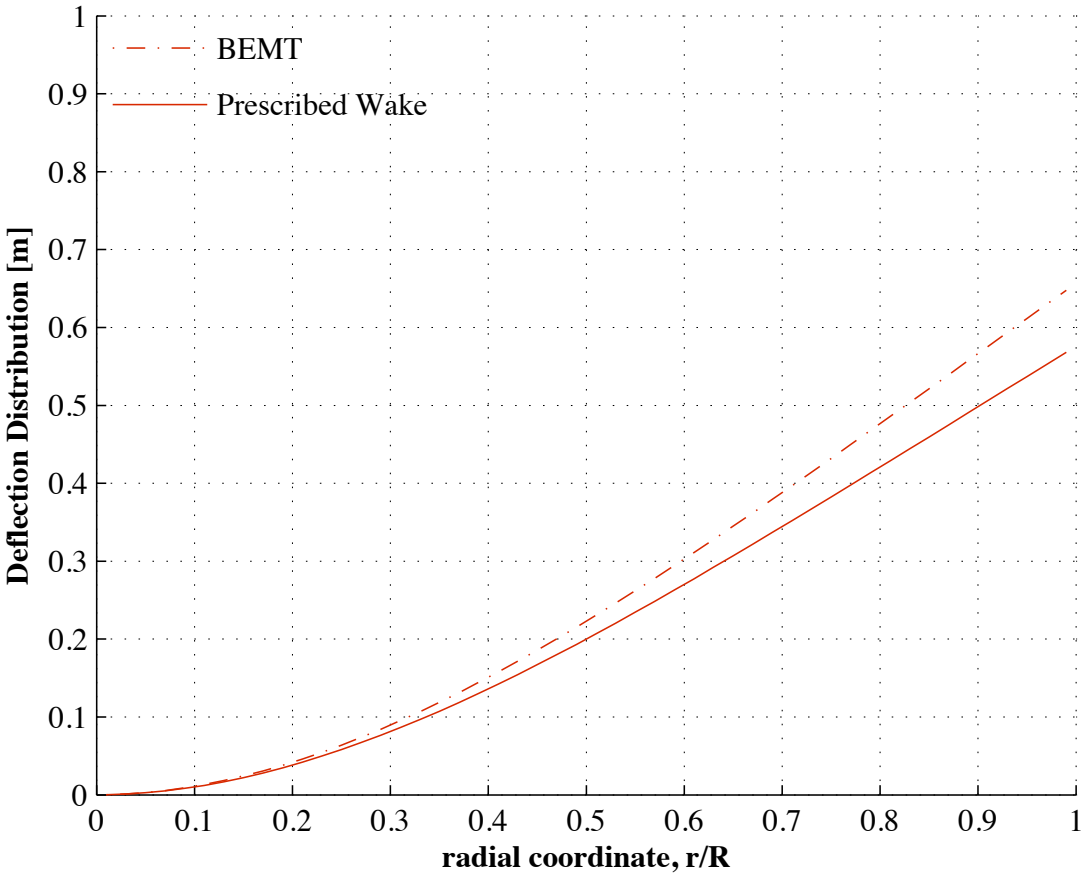

Figure 3.33: Deflection distribution along blade, full scale rotor at $T = 50lbs$, $(Z/R)_{hub} = 0.1$ and $18RPM$.

leads to differences in blade deflections, which, as shown in Fig. 3.33, are larger for the BEMT result due to the concentration of load at the blade tip producing larger bending moments. In the extreme ground effect case of interest differences in blade deflection distribution between the two methods are translated to differences in local height off the ground - $Z/R(\tilde{r})$ distribution. Since both methods are of an iterative nature, this will induce further differences in the calculated inflow results, thus effecting the thrust distributions and so on, until convergence is reached.

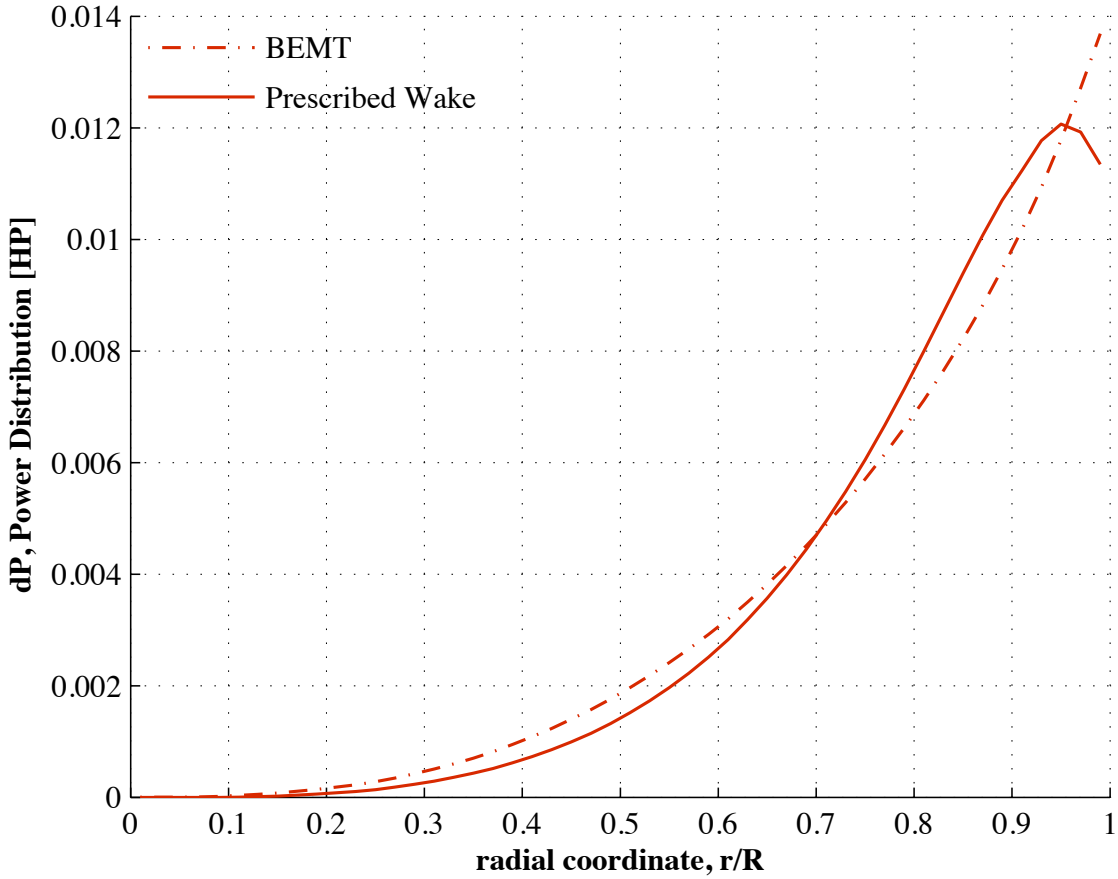

Figure 3.34: Power distribution along blade, full scale rotor at $T = 50lbs$, $(Z/R)_{hub} = 0.1$ and $18RPM$.

Finally, the resultant power distributions along the rotor radius were compared. A product of both the inflow and thrust distributions, the power distribution curves present closer agreement, which clarifies the source of the strong correlation between the total power values obtained when integrating over the blade (previously shown in Fig. 3.30).

Chapter 4

Calculated Results for Full Scale Flexible Rotor Performance in Extreme Ground Effect

4.1 Theoretical Parametric Study

The two proposed approaches to prediction of a flexible rotor's performance in extreme ground effect were validated in Sections 3.2.2 and 3.2.3. They were then used in a parametric study, examining the effect of various design parameters on the performance of the full-scale test rotor described in Section 3.2.1. The baseline rotor blade for this study was set as the 6.5 m radius, 1 m chord, untwisted, non-tapered full scale HPH blade shown in Fig. 3.12, using the *Eppler* 387 airfoil, and rotating at 18 RPM. Baseline stiffness values for both bending and torsion of the blades were obtained from static testing. The parametric study was carried out at the extreme ground effect operation height of 0.6 m from the ground corresponding to $(Z/R)_{hub} = 0.1$, the same height as the full scale test set-up in Fig. 3.12, to allow for easy comparison of potential experimental work.

The parametric study compares and discusses results from both rotor performance calculation methods under the varying parameters, noting unique trends and issues that should be considered when designing an optimized flexible rotor for operation in extreme ground effect.

It is understood that the prescribed wake method is of higher detail and is a better reflection of the physical behavior when describing the rotor wake, in the general out of ground effect case alongside this specific case of extreme ground effect. However, due to it's simplicity and low computational requirements, result using the BEMT formulation, corrected for ground effect, are also brought forth to establish trend similarities between predictions using the two methods. While it is clear that point design optimization should be done using the more elaborate prescribed wake model, this comparison will allow validation that the BEMT method is sufficient for preliminary studies of a flexible rotor in extreme ground effect.

For all the results shown hereafter, blade modeling utilized 50 elements, a constant value for both inflow methods . The prescribed wake model discretized each wake revolution into azimuthal segments in steps of 5°, following 10 rotor revolutions, with a near wake stretching 30° behind each rotor blade.

Note that the prescribed wake method did not converge for some extremity cases, although the more simplified BEMT method did provide results for these cases. The reason is attributed to the difference in the implementation of aerodynamic table use in the vortex method, described in Section 2.3.1 compared to the more common implementation used for BEMT Section 2.2.1.

4.1.1 Effect of Blade Bending Stiffness

Fig. 4.1 shows power vs thrust for the rotor at $Z/R_{hub} = 0.1$, calculated for the baseline flexible blades (100% stiffness), 200%, and 50% of baseline bending stiffness,

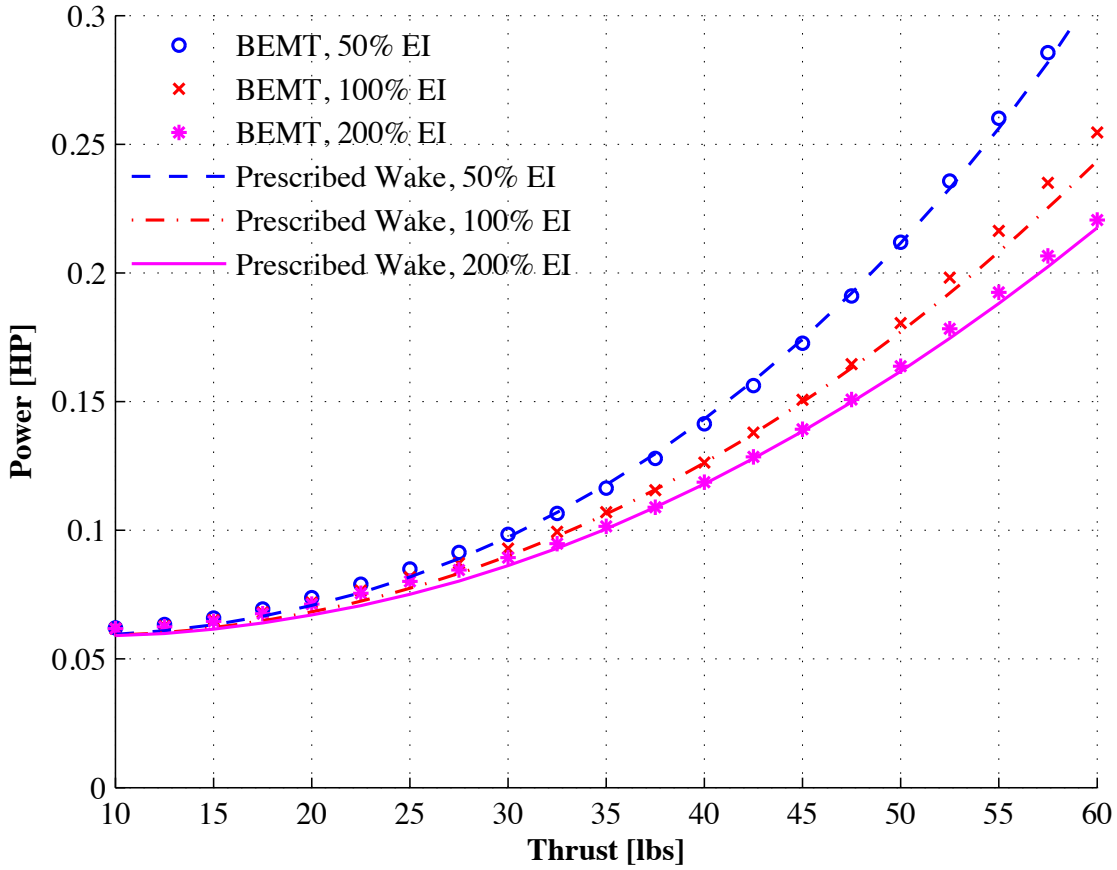

Figure 4.1: Effect of bending stiffness on full scale rotor performance IGE at $(Z/R)_{hub} = 0.1$ and 18 RPM

using both modeling approaches. The results show very good agreement between the two models. Operating this close to the ground with decreased bending stiffness allowing for substantially larger blade deflections, results in the outer blade sections operating higher off the ground. This decreases ground effect benefits and thereby increases power requirements (as previously demonstrated in Figures 3.18 and 3.26). This clearly demonstrates that in extreme ground effect conditions, reduced bending stiffness will result in higher power requirements, compared to it's effect out of

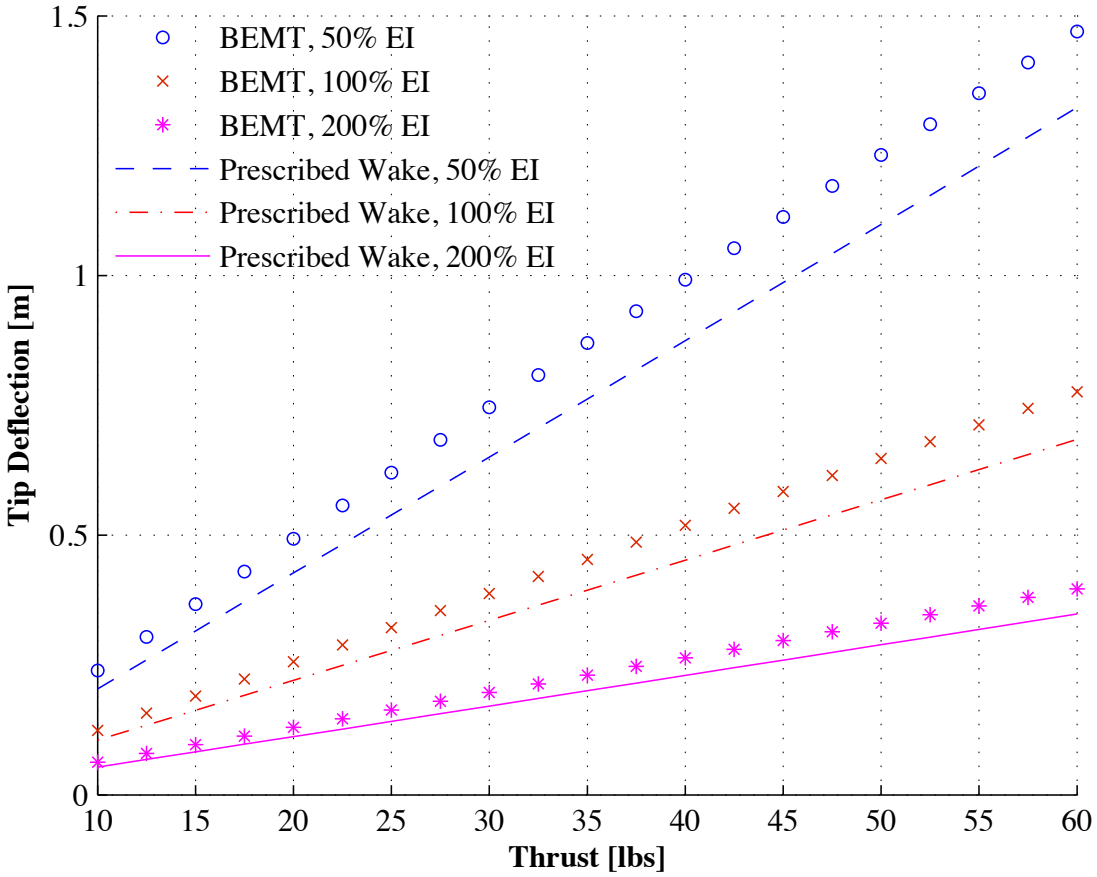

Figure 4.2: Effect of bending stiffness on full scale rotor tip deflection IGE at $(Z/R)_{hub} = 0.1$ and 18 RPM

ground effect demonstrated in Fig. 2.2(c) . This effect on performance characteristics becomes more substantial with increasing thrust, which in turn increases bending deflections even more as seen in Fig. 4.2. The tip deflections predicted by the two methods slightly differ for each given thrust as a result of the difference in thrust distributions, as discussed in Section 3.3 (Fig. 3.32), resulting from the two modeling approaches. The BEMT resultant thrust distribution, weighing more towards the blade tip, would create a stronger bending moment resulting in slightly

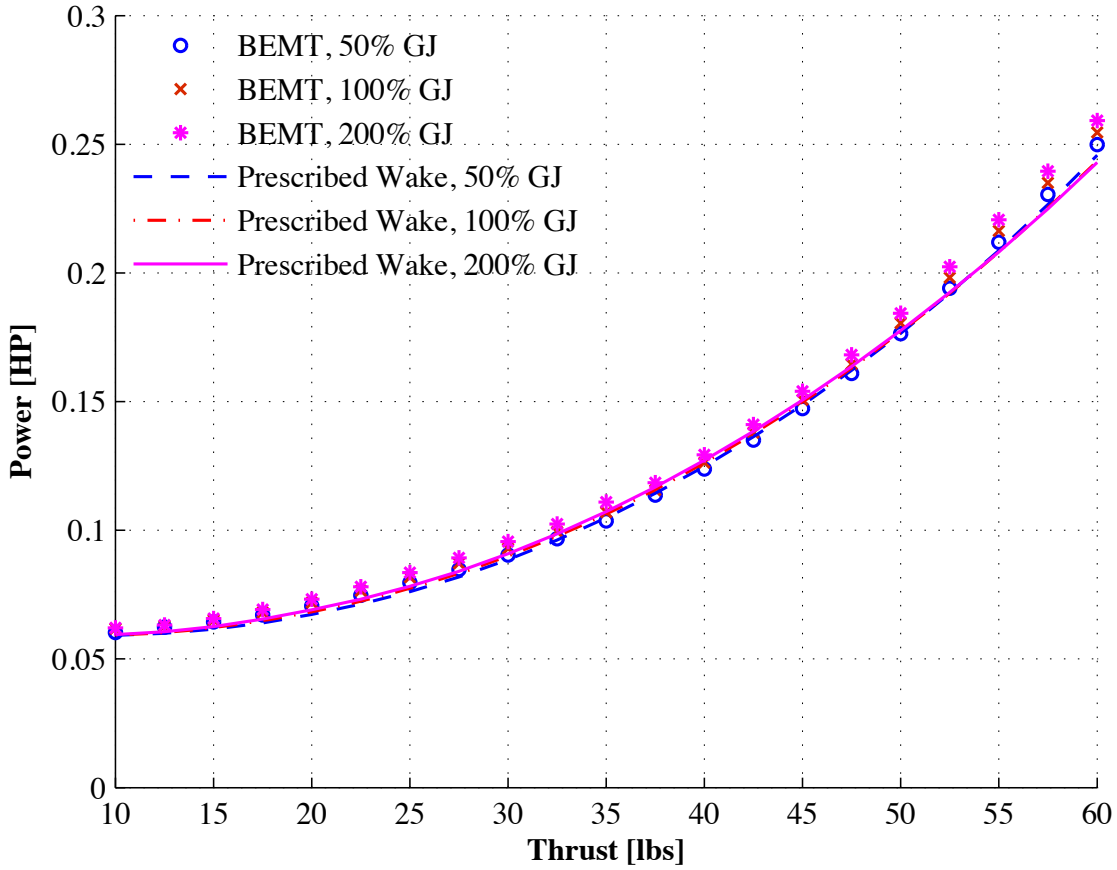

Figure 4.3: Effect of torsional stiffness on full scale rotor performance IGE at $(Z/R)_{hub} = 0.1$ and 18 RPM

higher deflections when compared the the more centered, prescribed wake method, thrust distribution.

4.1.2 Effect of Torsional Stiffness

Fig. 4.3 shows a similar power vs thrust study for the baseline, 200% and 50% torsional stiffness, using both approaches. The agreement between the two models remains, showing negligible effect of varying torsional stiffness on rotor per-

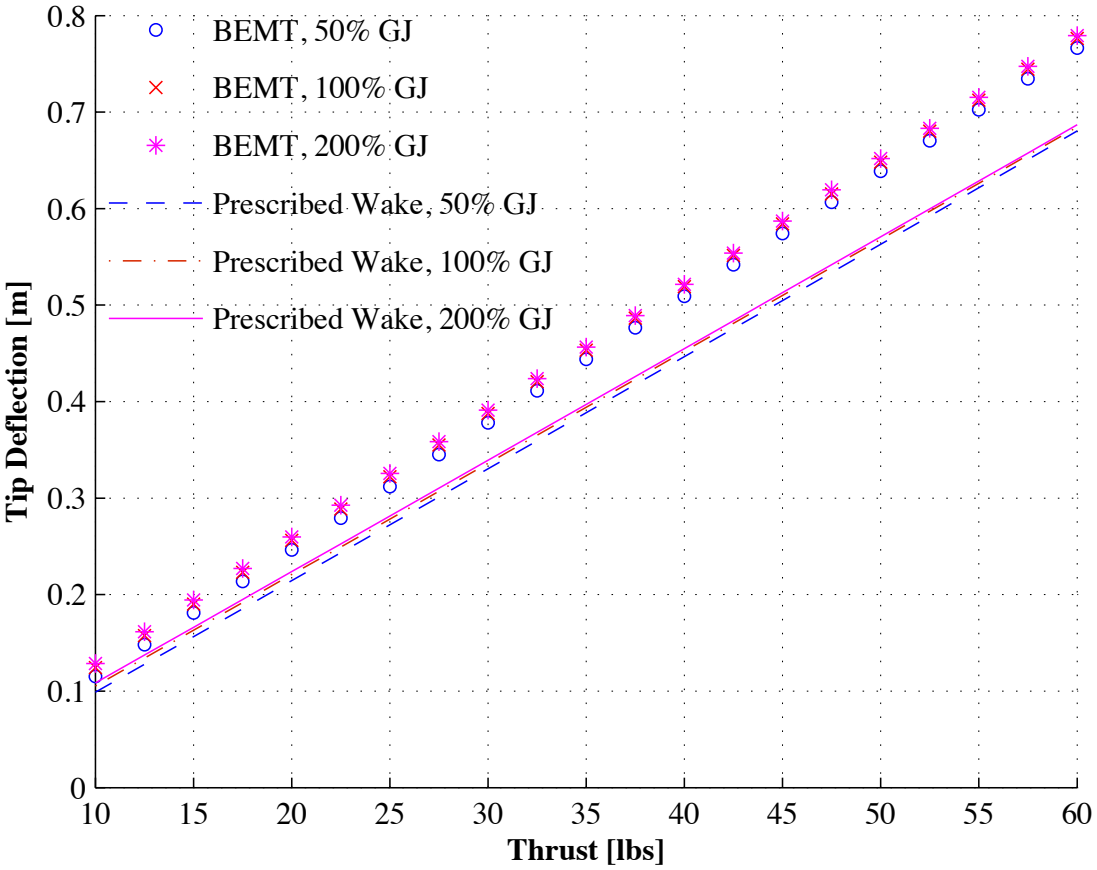

Figure 4.4: Effect of torsional stiffness on full scale rotor tip deflection IGE at $(Z/R)_{hub} = 0.1$ and 18 RPM

formance. The torsion stiffness variation, does not substantially affect the blade tip deflections, as shown in Fig. 4.4. There seems to be a slightly lower deflection, in both approaches, for the torsionally softer blade, which would also result in variation of loading distribution along the blade, under the variation in angle of attack. These differences are, however, relatively mild and do not account as a concern in the design problem.

4.1.3 Effect of Rotor RPM

Power variation with rotor RPM was examined over the range of $12 \leq RPM \leq 24$, at three thrust levels of 30 lbs, 40 lbs, and 50 lbs per rotor, representing C_T of 0.0055, 0.0073, and 0.0091, or rather C_T/σ of 0.056, 0.075, and 0.093 respectively.

In general, rotating at higher RPM values (higher Ω values) inherently increases profile drag throughout the blade, as:

$$dD = \frac{1}{2}\rho U^2 C_d c dr \approx \frac{1}{2}\rho U_T^2 C_d c dr = \frac{1}{2}\rho(\Omega r)^2 C_d c dr \tag{4.1}$$

while lift values remain relatively unchanged (so as to maintain the same total thrust), thus decreasing the local lift to drag ratio - L/D. On the other hand, lower RPM values (for the same thrust) would require higher lift coefficients, attained by higher angles of attack, to maintain the same total lift as:

$$dL = \frac{1}{2}\rho U^2 C_l c dr \approx \frac{1}{2}\rho U_T^2 C_l c dr = \frac{1}{2}\rho(\Omega r)^2 C_l c dr \tag{4.2}$$

This would also result in increased drag as higher angles of attack are associated with higher drag coefficients (closer to stall), again resulting in a decrease of the local L/D value.

Assuming the lift distribution remains fairly constant with variation in RPM (as the rotor is trimmed to the same total thrust), a connection between L/D and power required, dominated by variation in drag values, can be established. Hence, higher local drag values, implying lower local L/D values, would result in higher power requirements for a given thrust.

Due to the contradicting effects described above, both increased and decreased rotor RPM may lead to a decrease in L/D. Therefore, a maximal L/D operation

point should exist for each thrust requirement, portraying an optimal RPM for minimum power.

Figure 4.5 displays said power vs RPM trend for the three different load cases at the operational height of $(Z/R)_{hub} = 0.1$. The RPM value for minimum power appears to increase with required thrust, as the optimal L/D conditions vary with load increase. In further detail, higher loading requires higher angles of attack, leading to increased C_d values, and decreased L/D for a sub-optimal RPM value. Therefore, there is an offset in the minimum power RPM point, requiring higher optimal RPM for higher loading, followed by the expected power increase due to increasing Ω. The figure shows results using both rotor wake models which portray good agreement, although, as expected, the prescribed wake model converged across a smaller range of lower RPM values due to it's higher sensitivity to stalled blade elements.

4.1.4 Effect of Rotor Radius

Figure 4.6 shows power results vs variation in rotor radius at a rotor RPM of 18, using both wake models, at the same three thrust levels of 30 lbs, 40 lbs, and 50 lbs. This study considers the full scale test rotor radius of 6.5 m (see Fig. 3.12) as a reference value. The results clearly convey a favorable rotor radius for minimum power at each thrust level.

For a given thrust and rotor RPM, a decrease in blade radius decreases rotor solidity σ and increases the thrust coefficient C_T (see Eq. (2.14)). Thus, the blade

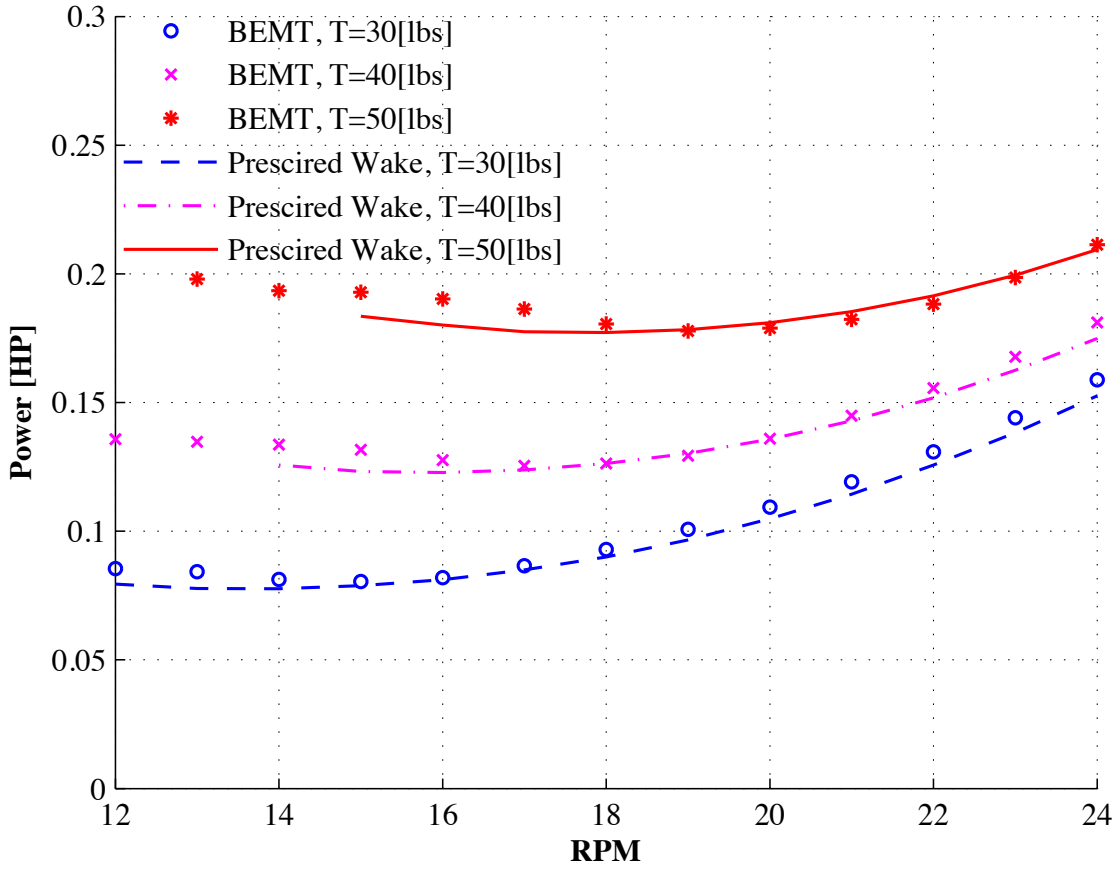

Figure 4.5: Effect of RPM on full scale rotor performance IGE at $(Z/R)_{hub} = 0.1$

loading coefficient $\frac{C_T}{\sigma}$ is increased, resulting in a higher average $\bar{C}_l$ (see Eq. (**??**)). Therefore, shorter blades, providing smaller lifting surfaces and thus requiring higher C_l values, therefore operating at higher angles of attack, which result in higher C_d values. Both in turn, as shown in Equations 2.12 and 2.13, increase F_x - resulting in higher torque, and thus higher power requirements. On the other hand - longer blades for the same given thrust and RPM, result in increased drag due to the blade tips operating at higher velocities, and increased torque due to larger moment arms. More importantly, in the case of flexible blades in extreme ground effect, longer blades under the same load result in higher tip deflections, that in turn reduce ground effect benefits at outboard blade sections, which carry the majority of the thrust load.

Also apparent from this study is that the optimal rotor radius increases with the thrust requirement. This is expected, as the blade sections would operate at higher angles of attack for higher thrust requirements. Thus, the effect associated with higher angle as described above would be more pronounced, shifting the optimal rotor radius point towards higher values.

The actual optimal radii vary slightly between the two methods. This is a result of the difference in the inflow modeling, resulting in different thrust distributions and ultimately different blade deflections, which in turn affect power requirements.

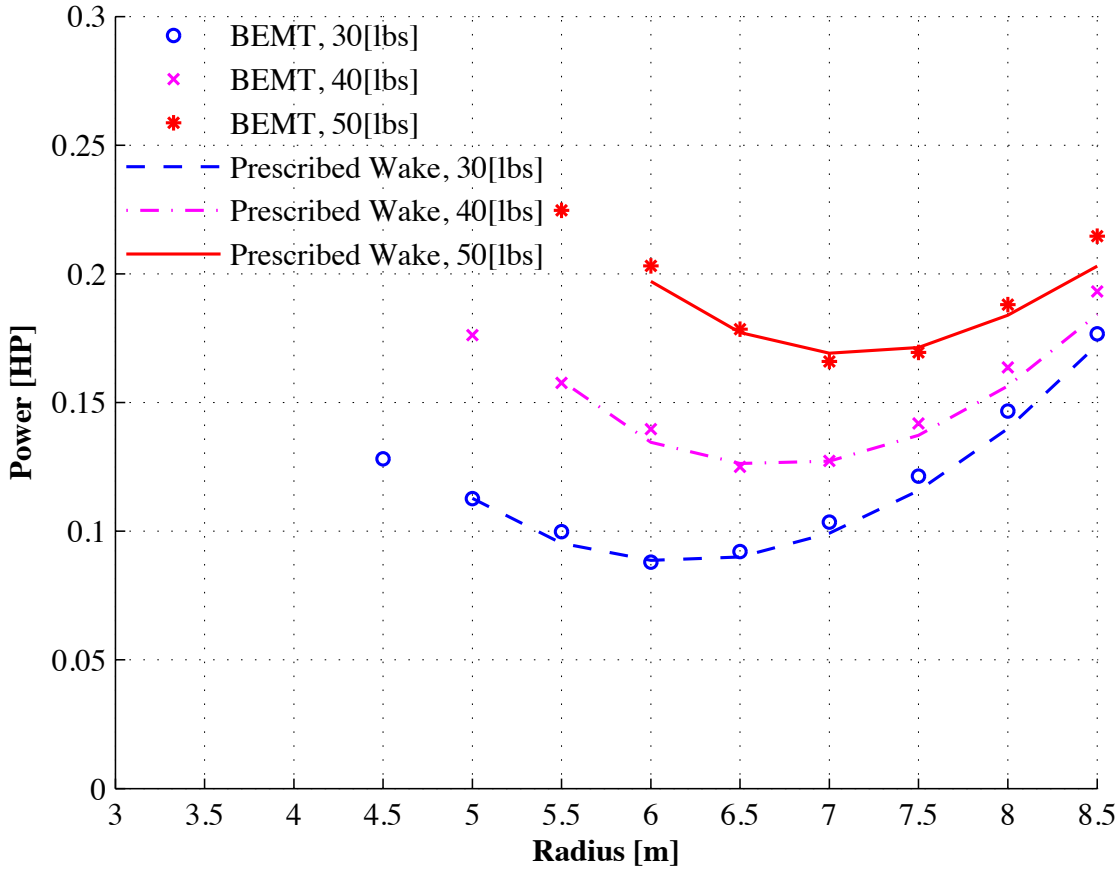

Figure 4.6: Effect of rotor radius on full scale rotor performance IGE at $(Z/R)_{hub} = 0.1$ and 18 RPM

4.1.5 Effect of Blade Chord

The effect of variation in blade chord c was also studied at the rotor RPM of 18, at the three thrust level power requirements, using both BEMT and the prescribed wake model. This study, shown in Fig. 4.7, considers the full scale test rotor blade chord measuring 1 m (see Fig. 3.12) as a reference value. Here too, the results display an optimal chord value for minimum power, increasing with the thrust requirement. However, the variation in power is of a milder nature compared to the effect of variation in rotor radius shown in Section 4.1.4. A smaller blade chord means the blade sections will operate at lower Reynolds numbers, which are associated with higher drag penalties (see Fig. 4.8 for an example, based on data from Selig and McGranahan [7]). Also, a smaller blade chord reduces the lifting surface, requiring higher angles of attack for a given thrust (see Eq. (**??**)), similarly to the effect of smaller radii. This causes an increase power requirements, eventually making very small chord values less beneficial as the onset of stall approaches. On the other hand, as power requirements are derived from the shaft torque, which is dependent on dimensional drag (see Eq. (4.1) for drag, Eq. (2.12) for torque and Eq. (2.13) for power), large blade chord values might result in higher power requirements although they might be characterized with lower C_d values.

In this case, as well as the previous, the two prediction models show qualitative agreement, portraying a minimum power chord value. The differences in the quantitative results calculated by the two methods increase with the thrust level due to the increasing deflections, as explained above for varying radius (Section 4.1.4).

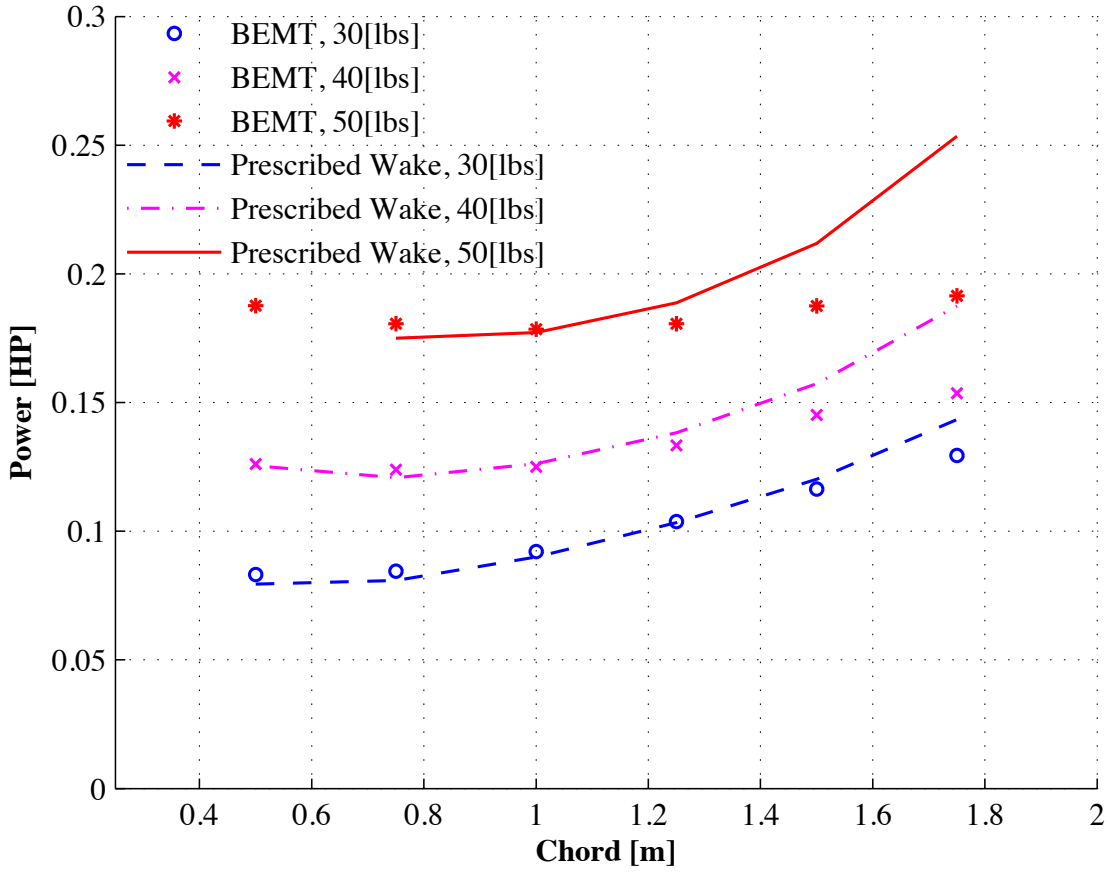

Figure 4.7: Effect of chord length on full scale rotor performance IGE at $(Z/R)_{hub} = 0.1$ and 18 RPM

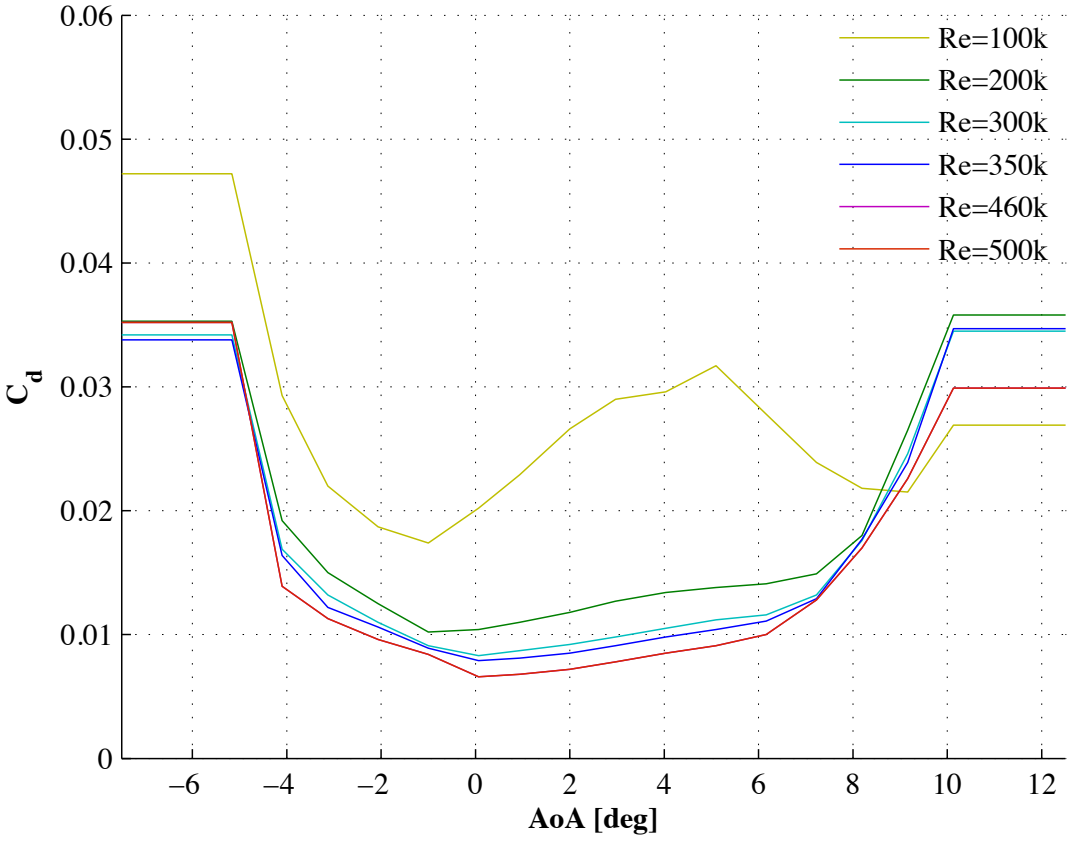

Figure 4.8: Effect of Reynolds number on drag coefficients for *Eppler* 387 airfoil. Based on Selig and McGranahan [7]

4.1.6 Effect of Linear Planform Taper

The effect of linear planform taper was studied as the chord distribution was varied while maintaining a constant thrust weighted solidity, using the full scale test rotor (Fig. 3.12) solidity of $\sigma = 0.098$ as a reference value. The taper ratio (root chord over tip chord) was increased from a rectangular planform up to a taper ratio of $5:1$, example planforms show in Fig. 4.9. Shown in Fig. 4.10 are power vs taper ratio results at the three thrust levels of 30 *lbs*, 40 *lbs*, and 50 *lbs*, for both inflow models. The results show power reductions as taper ratio increases, slightly more pronounced when using the prescribed wake model.

Accounting for taper in the BEMT model results in a thrust distribution peaking at a slightly lower value as more thrust is distributed towards the inboard sections, as seen in Fig. 4.11, which in turn results in reduced bending moments and slightly smaller deflections. The smaller tip deflections allow for more beneficial ground effect and subsequently a slight decrease in power.

The calculated prescribed wake results are explained via the extraction of lift coefficient as described in Eq. (2.41). The wake geometry is barely influenced by the planform taper, the only effect being the slight geometric variations in the three-quarter chord positions and trailing vortices points of origin. Therefore, the circulation distribution along the blade span remains mostly unchanged. For a similar circulation distribution, the lift coefficient is inversely dependent on blade chord, and is calculated as follows:

$$\bar{C}_l(\tilde{r}) = \frac{2\overline{\Gamma}(\tilde{r})}{U \cdot \bar{c}(\tilde{r})} \tag{4.3}$$

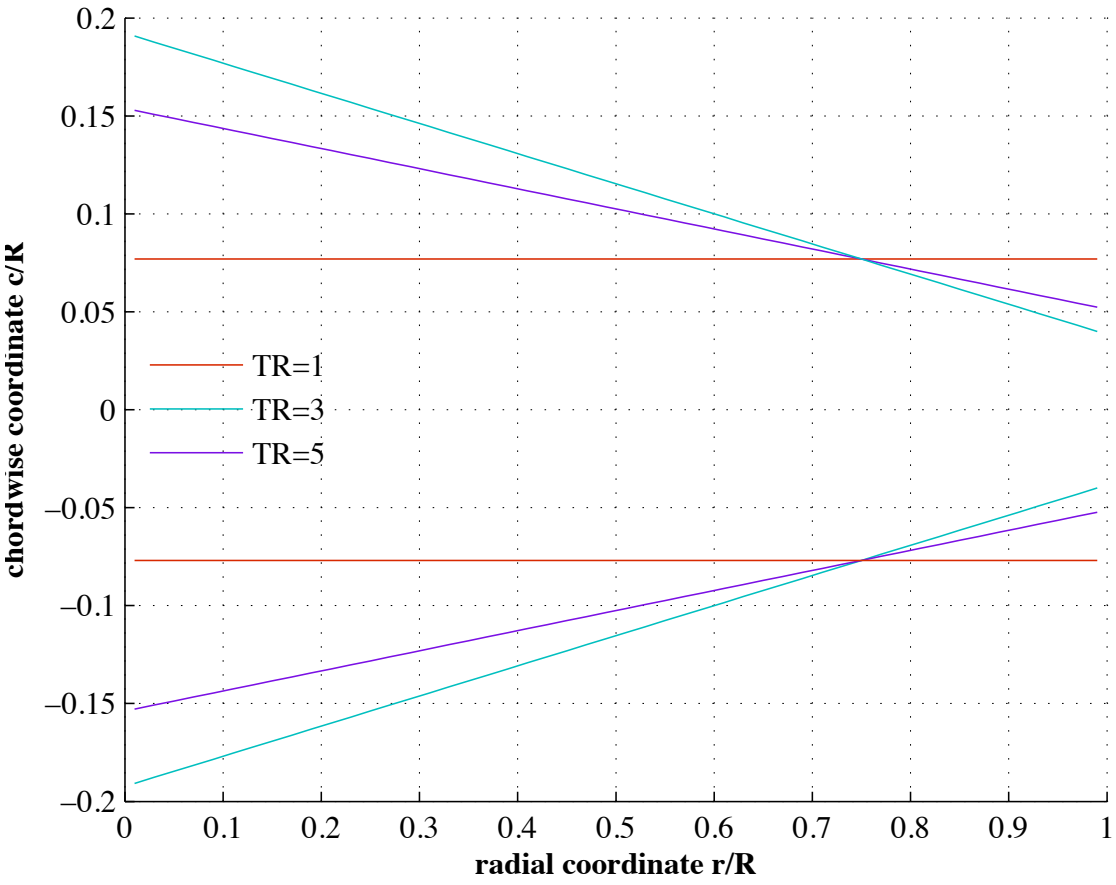

Figure 4.9: Blade planform using various thrust weighted solidity taper ratios

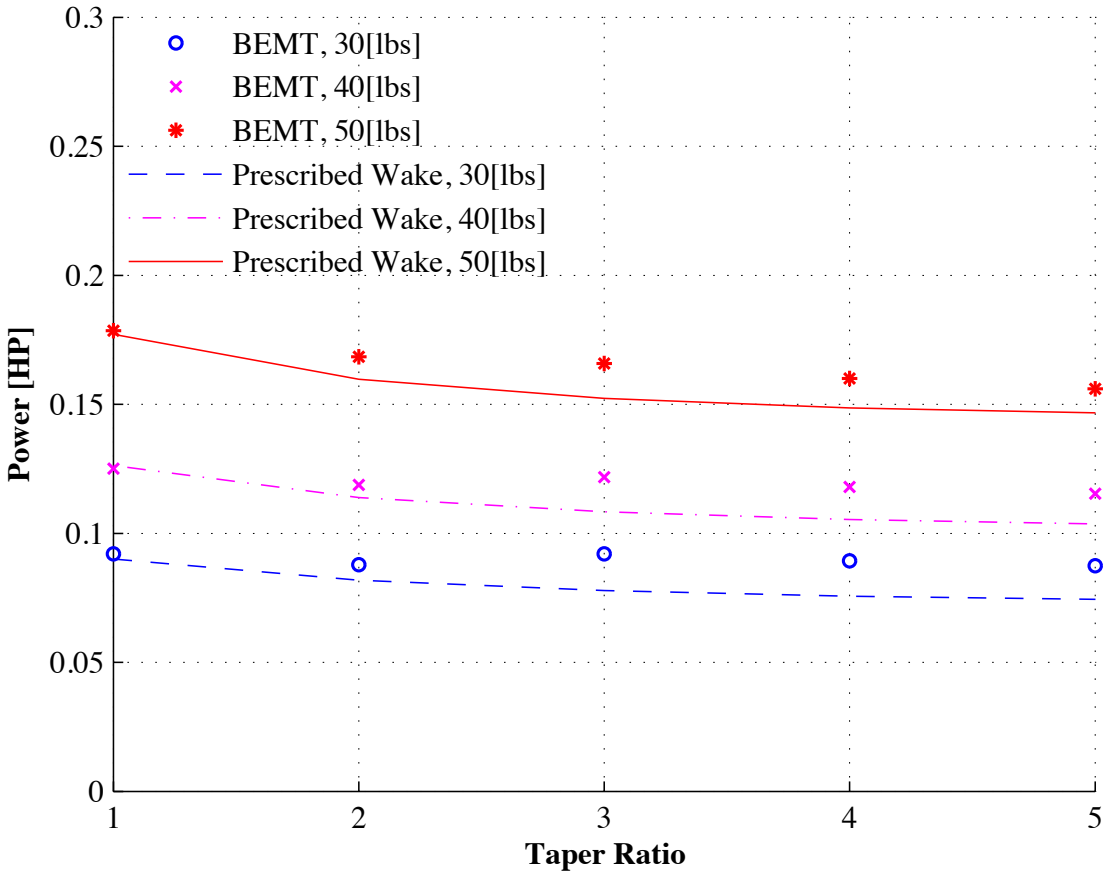

Figure 4.10: Effect of planform taper on full scale rotor performance IGE at $(Z/R)_{hub} = 0.1$ and 18 RPM

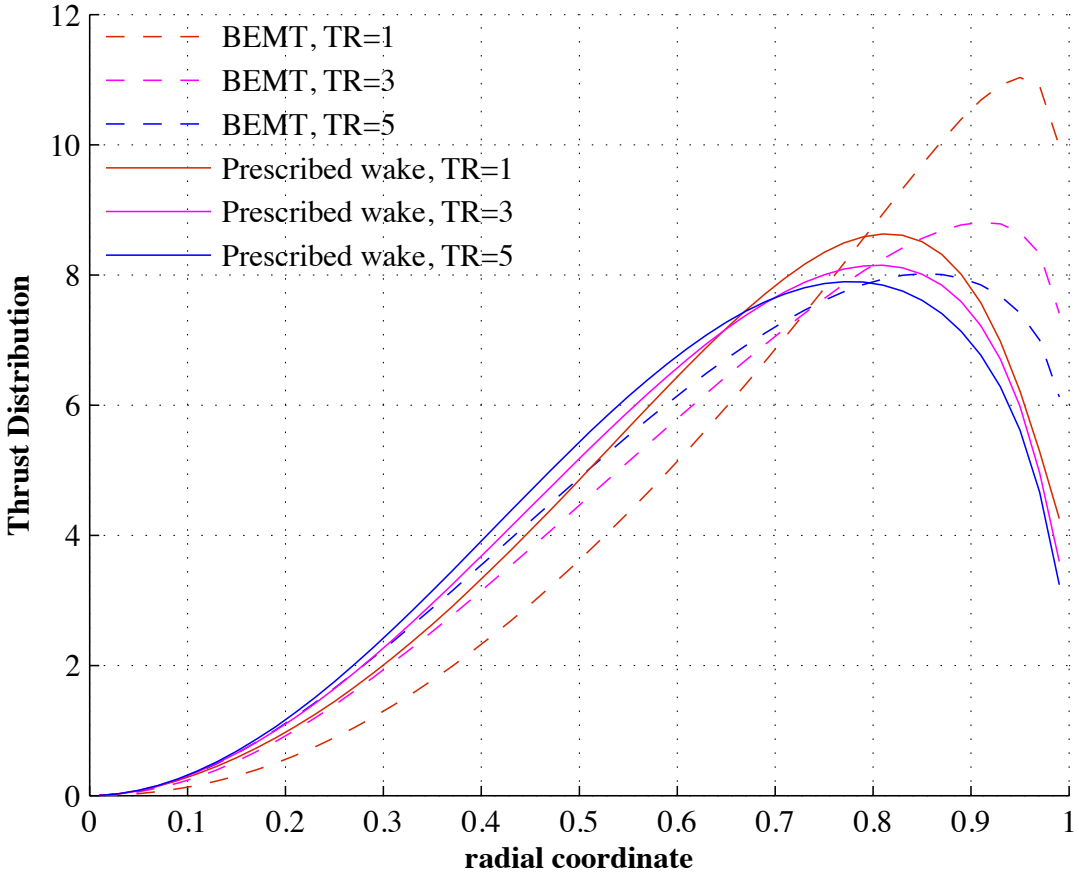

Figure 4.11: Effect of planform taper on full scale rotor thrust distribution IGE at $(Z/R)_{hub} = 0.1$, 18 RPM, and 50 lbs

As a result, the lift distribution along the blade approaches a slightly more uniform distribution, offloading the outboard blade elements. This results in a similarly slightly shallower thrust distribution, demonstrated in Fig. 4.11, and ultimately in decreased power. Within airfoil stall limits, as a stronger taper ratio is applied, the loading on the blade becomes more uniform which decreases torque, and thus power.

The effect of taper appears to be more pronounced in extreme ground effect reaching up to a $10\% - 15\%$ decrease in power, relative to the expected few percentages $(2\% - 4\%)$ of power savings for conventional rotors hovering out of ground effect [3]. Since as discussed above, induced power decreases significantly with inflow in extreme ground effect, the relative part of profile power in total power becomes larger. Thus savings in profile power as a result of blade taper are substantially more pronounced in this case.

4.1.7 Effect of Linear Planform Twist

The influence of linear blade twist on rotor performance was investigated next, and is shown in Fig. 4.12 for the same three thrust levels of 30 lbs, 40 lbs, and 50 lbs, at a rotor RPM of 18. This study considers the untwisted full scale test rotor blades (see Fig. 3.12) as a reference case. The results indicate a minor effect of blade twist on power requirements, diminishing with increasing thrust (where on average the resulting angles of attack become closer to stall).

Also apparent in Fig. 4.12 are the differences in the modeled effect of blade twist between the two methods. The two rotor model approaches show good agree-

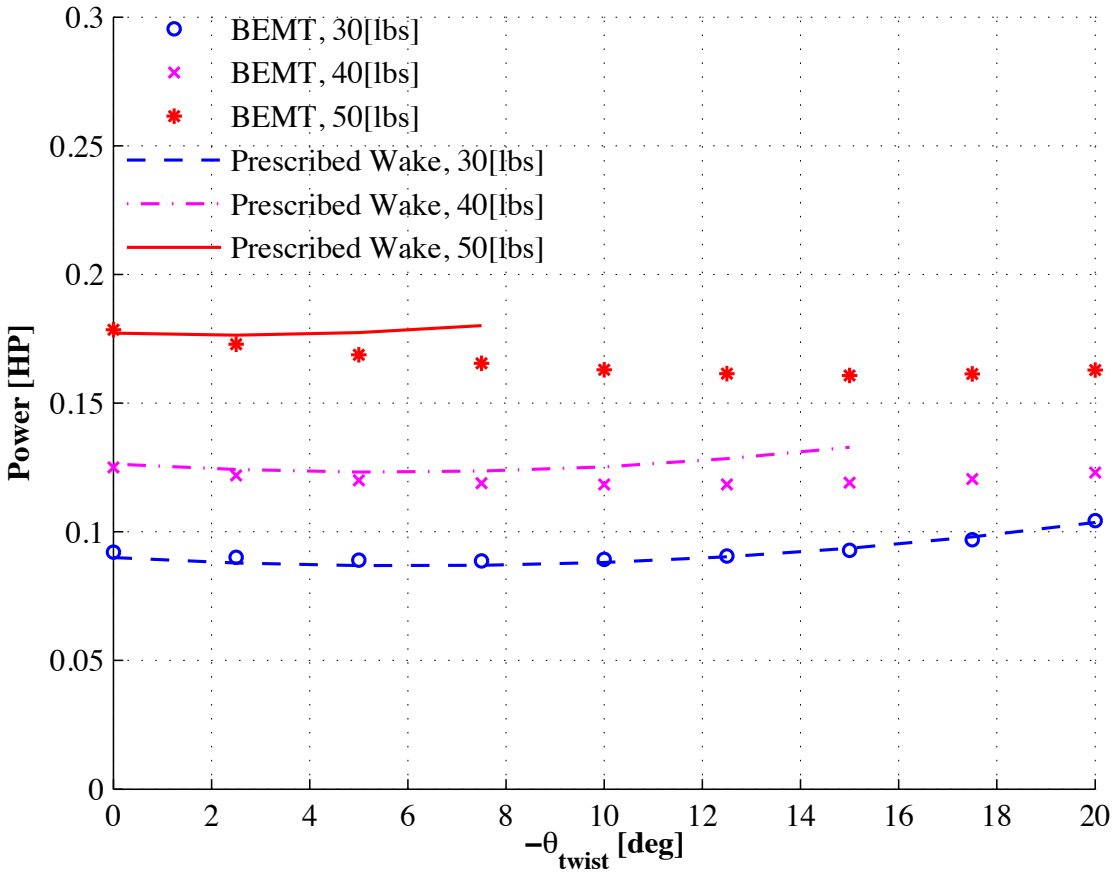

Figure 4.12: Effect of linear twist on full scale rotor performance IGE at $(Z/R)_{hub} = 0.1$ and 18 RPM

ment for the lower thrust level, but differ in their prediction as the thrust level increases. This may result from the differences in the thrust distributions predicted by the two methods, causing differences in blade deflections. These differences become more pronounced with higher thrust and increased loading on the rotor blades.

However, it should be noted that the in ground effect prescribed wake model proposed in this work does not include the change of the wake shape coordinates as a result of blade twist, unlike the common out of ground effect prescribed wake models such as [46] and [6] (see Eq. (2.32)). Therefore the only effect of blade twist is via the geometric twist of the blade and subsequently a slight change in the position of the trailing vortices along the blade. Inclusion of this effect requires experimental work examining wake shapes of rotors with twisted and untwisted blades in extreme ground effect.

4.2 UMD Human Powered Helicopter Flight

In the spring of 2011 a fully assembled quad-rotor human powered helicopter, weighing in at 105 *lbs* (shown in Figures 4.13 and 4.14), was ready for flight testing at UMD - operated by a 107 *lbs* female cyclist, totaling at 212 *lbs*. Based on experimental studies using the full scale flexible test rotor (see Fig. 3.12), the vehicle rotors were set to rotate at 18 RPM. The predictive methods were employed towards examining the performance of the HPH rotors at the designed operational height of 30cm ($(Z/R)_{hub} = 0.046$), the lowest reasonable height above ground that would not jeopardize the delicate blades structure in operation. The predictions for power

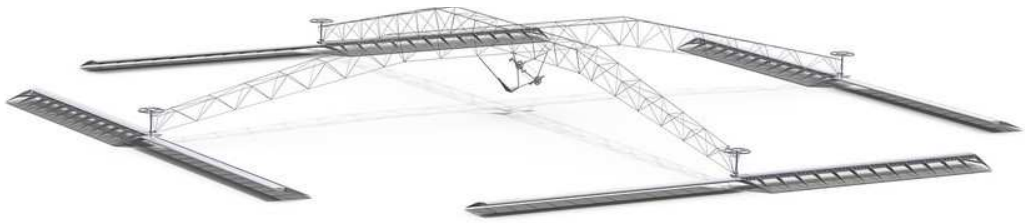

Figure 4.13: Illustration of UMD Human powered helicopter design, summer 2011

Figure 4.14: UMD Human powered helicopter in flight, summer 2011

requirements from both methods, at the required thrust of 53 *lbs* per rotor ($C_T = 0.0097$), are shown in Fig. 4.15. The BEMT results show the required power for HPH hover to be approximately 0.182 HP per rotor - for a total human power requirement of 0.72 HP, while the prescribed wake method predicts 0.173 HP per rotor - totaling at a 0.69 HP pilot output requirement. These requirements were within top limit of the female pilot's measured sprinting capabilities, and the first hover of the human powered helicopter was indeed accomplished for 4.2 seconds in May of 2011, a record broken shortly after by a successful 12.4 second flight in July of 2011.

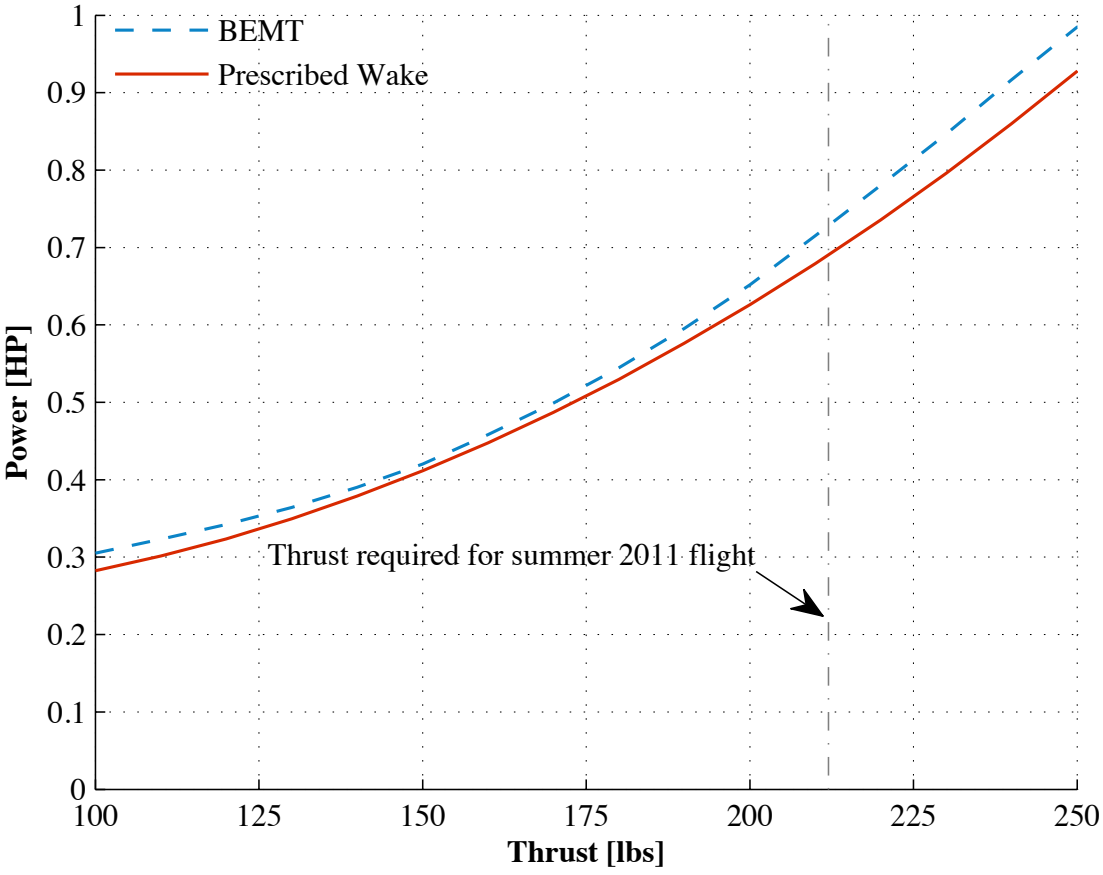

Figure 4.15: Predictions for UMD HPH performance at $(Z/R)_{hub} = 0.046$ and $18RPM$

It is firmly believed that alongside attempts to reduce structural weight, careful optimization of the rotor blades, using the proposed tools, can substantially enhance the vehicle hover capabilities by reducing the total human power requirement, thus increase the project's success in attempting the Sikorsky Challenge.

Chapter 5

Summary and Conclusions

5.1 Summary

Motivated by the attempt at the Sikorsky human powered helicopter challenge, this work was conducted towards understanding the effect of various design parameters on the performance of a flexible rotor in extreme ground effect conditions. The challenge calls for a design of an ultra-lightweight, and therefore highly elastic rotor blades, operating in extreme ground effect to minimize power requirements due to limited human power capabilities. Two new approaches for performance prediction of a highly flexible rotor in extreme ground effect are developed in this work.

The first approach is a correction for classical BEMT, accounting for ground effect, applied at each element of the deformed blade relative to it's local height off the ground. For this method, a ground effect model was extracted using experimental data obtained from a dedicated in-house sub-scale test with a focus on extreme ground effect.

The second approach is based on the prescribed wake vortex method. Utilizing a new prescribed wake model representing geometric tip vortex trajectories in ground effect, based on experimental wake measurements, this method employs a mirror image rotor to represent the ground no-penetration boundary condition on the rotor wake flow.

Two new sets of experimental results for rotor performance in extreme ground effect were presented. The first setup includes a rigid sub-scale rotor ($R = 1.26\ m$) operating in the regime of $0.06 \leq Z/R \leq 2.0$. The second experiment uses the full-scale HPH rotor ($R = 6.5\ m$) , tested at $(Z/R)_{hub} = 0.1$ and $(Z/R)_{hub} = 0.2$.

Both computational methods were extensively validated for both rigid and highly elastic rotor cases, in and out of ground effect, using the new experimental data alongside experimental data from literature.

A parametric study was then carried out, examining the effects of various rotor design parameters on a flexible rotor performance in extreme ground effect. This study displays calculated results using both methods, showing a general agreement in behavioral trends.

5.2 Conclusions

The main conclusion from this study is that elastic blade bending deformations are of key importance in terms of power requirements, for a rotor hovering in extreme ground effect. For a flexible rotor, allowing for substantial tip deflections, the outboard blade segments operate higher off the ground thereby reducing the benefits from ground effect. This effect is of high importance because the majority of the thrust is provided by outboard blade sections, which in turn are associated with most of the required power. For the same reason, for a flexible rotor, ground effect benefits rapidly diminish as the blade deflection increases.

This work has clearly shown that careful consideration of blade deflections as

part of the elemental inflow modeling in ground effect, is key to satisfactory performance predictions when modeling flexible rotor performance in extreme ground effect, that are successfully validated against multiple experimental cases.

It is clearly shown that blade bending stiffness has an important effect on performance in these operational conditions. When hovering in extreme ground effect, a highly flexible rotor requires substantially more power. For example, when compared at a thrust level of 50 lbs, for the baseline bending stiffness case, the elastic rotor would require 15% more power than that of a rigid rotor. It was also shown that the loss of ground effect increases as bending stiffness decreases.

Additionally, when studying the effect of various design parameters on rotor performance in ground effect, it was concluded that the parameters that change thrust distribution have an increased effect on performance, compared to their known effects out of ground effect.

The effects of varying rotor radius, blade chord, RPM, were studied, showing that for all three parameters, an optimal value for minimum power exists. The optimal value was shown increases with required thrust . The effect of rotor radius was found to be more pronounced. Larger radii, resulting in higher blade deflections for a given load, were shown to result in increased power due to losses in ground effect.

Studying the effect of linear planform taper for the full scale flexible rotor resulted in significant power savings as well, as a result of changes in thrust distributions. For example, 15% savings in required power were demonstrated for the 50 lbs thrust level when implementing a 3:1 planform taper ratio, while maintain-

ing the same thrust weighted solidity. The relative effect of linear blade twist on the flexible blades was shown to have a negligible effect on power. The effect of torsional stiffness on performance was also shown to result in negligible changes to power requirements. Throughout the parametric studies, the effect of blade deflections (resulting from variances in thrust distribution shapes), were shown to increase with thrust requirements. This is due to the loss of ground effect associated with higher deflections at higher loads.

The BEMT based method and the prescribed wake based approach presented in this work, show very good agreement in prediction of flexible rotor performance in these conditions, both supporting the conclusion that accounting for the local Z/R at each blade element plays a key role in these results. However, the optimal parameter values slightly differ between the methods, due to differences in thrust distributions along the blade (originating from the different inflow models). Therefore, due to the principle agreement, it is concluded that the simpler, faster, BEMT approach is sufficient for use in preliminary studies of flexible rotor behavior in extreme ground effect, while the higher quality prescribed wake method may be used for a more comprehensive point design optimization.

Bibliography

[1] J.G. Leishman. *Principles of Helicopter Aerodynamics*. Cambridge University Press, 1932.

[2] R. B. Gray. An aerodynamic analysis of a single-bladed rotor in hovering and low speed forward flight as determined from smoke studies of the vorticity distribution in the wake. Princeton University Aeronautical Engineering Report no. 356, Princeton, New Jersey, 1956.

[3] W. Johnson. *Helicopter Theory*. Princeton University Press, Princeton, NJ, 1980.

[4] R. W. Prouty. *More Helicopter Aerodynamics*. Phillips Business Information, 1999.

[5] W. Z. Stepniewski and C. N. Keys. *Rotary-Wing Aerodynamics Volume II*. Dover Publications, New York, NY, 1984.

[6] J. D. Kocurek and J. L. Tangler. A Prescribed Wake Lifting Surface Hover Performance Analysis. *Journal of the American Helicopter Society*, 21 (1):24–35, 1976.

[7] M. S. Selig and B. D. McGranahan. Wind tunnel aerodynamics tests of six airfoils for use on small wind turbines. NREL/SR-500-34515 , 2004.

[8] AHS International. Igor i. sikorsky human-powered helicopter competition. www.vtol.org/awards/hph, 1980.

[9] A. Filippone. On the possibility of human-powered vertical flight. *Journal of the American Helicopter Society*, 52 (4), 2007.

[10] S. Larwood and N. Saiki. Aerodynamic design of the cal poly da vinci human-powered helicopter. American Helicopter Society Vertical Lift Aircraft Design Conference, CA, 1990.

[11] H. Goto, D. Kato, K. Abe, T. Kawasima, T. Motohashi, and A. Naito. Power measurements of yuri i. Nihon University, Japan, 1994.

[12] W. J. M. Rankine. On the mechanical principles of the action of propellers. *Transactions of the Institute of Naval Architects*, 6:13–39, 1865.

[13] R. E. Froude. On the part played in propulsion by differences of fluid pressure. *Transactions of the Institute of Naval Architects*, 20:390, 1889.

[14] A. Betz. Development of the inflow theory of the propeller. NACA TN 24, 1920.

[15] A. Betz. Z. flugtech. u motorluftschiffahrt, 1920.

[16] A. Betz. The theory of the screw propeller. NACA TN 83, 1922.

[17] H. Glauert. Airplane Propellers, *In Division L of Aerodynamic Theory ed W.F. Durand*. Springer Verlag, Berlin, Germany, 1935.

[18] S. Drzewiecki. Bulletin de l'association technique maritime, 1892.

[19] S. Drzewiecki. Thórie générale de l'hélice. Paris, 1920.

[20] H. Reissner. Z. flugtech. u motorluftschiffahrt. 1, pp.257-309, 1910.

[21] H. Reissner. On the vortex theory of the screw propeller. *Journal Aeronaut. Sciences*, 5 (1):1–6, 1937.

[22] H. Reissner. A generalized vortex theory of the screw propeller and its application. NACA TN 750, 1940.

[23] G. de Bothezat. The general theory of blade screws. NACA TR 29, 1919.

[24] A.F. Gustafson and A. Gessow. Effect of rotor tip speed on helicopter rotor performance and maximum forward speed. NACA ARR No. L6A16, 1946.

[25] A. Gessow. Effect of rotor-blade twist and plan-form taper on helicopter hovering performance. NACA TN 1542, 1948.

[26] Tangler J. and Kocurek J. D. Wind turbine post-stall airfoil performance characteristics guidelines for blade-element momentum methods. 43rd AIAA Aerospace Sciences Meeting and Exhibit Reno, Nevada , 2005.

[27] C. Crawford. Re-examining the precepts of the blade element momentum theory for coning rotors. *Wind Energy*, 9:457–478, 2006.

[28] N. Tenguria, N. D. Mittal, and S. Ahmed. Investigation of blade performance of horizontal axis wind turbine based on blade element momentum theory (bemt) using naca airfoils. *International Journal of Engineering, Science and Technology*, 2 (12):25–35, 2010.

[29] F. Bohorquez, D. Pines, and Samuel P. D. Small rotor design optimization using blade element momentum theory and hover tests. *Journal of aircraft*, 47 (1):268–283, 2010.

[30] H.A. Madsen, C. Bak, M. Døssing, R. Mikkelsen, and S. Øye. Validation and modification of the Blade Element Momentum theory based on comparisons with actuator disc simulations. *Wind Energy*, 13:373–389, 2010.

[31] I. Masters, J Chapman, J. Orme, and M. Willis. A robust blade element momentum theory model for tidal stream turbines including tip and hub loss corrections. *Journal of Marine Engineering and Technology*, 10 (1):25–35, 2011.

[32] A. J. Landgrebe. The Wake Geometry of a Hovering Helicopter Rotor and Its Influence on Rotor Performance. *Journal of the American Helicopter Society*, 17 (4), 1972.

[33] J. G. Leishman and A. Bagai. Challenges in Understanding the Vortex Dynamics of Helicopter Rotor Wakes. *AIAA Journal*, 36 (7):1130–1140, 1998.

[34] A. J. Landgrebe. Overview of helicopter wake and airloads technology. 2nd International Conference on Rotorcraft Basic Research, College Park, MD, 1988.

[35] W. J. McCroskey. Vortex wakes of rotorcraft. 33rd AIAA Aerospace Sciences Meeting and Exhibit, 1995.

[36] H. Lamb. *Hydrodynamics*. Cambridge University Press, Cambridge, UK, 1932.

[37] D. R. Clark and A. C. Leiper. The free wake analysis, a method for the prediction of helicopter rotor hovering performance. *Journal of the American Helicopter Society*, 15 (1), 1970.

[38] S. G. Sadler. A method for predicting helicopter wake geometry, wake induced flow, and wake effects on blade airloads. 27th Annual National V/STOL Forum of the American Helicopter Society, 1971.

[39] S. G. Sadler. Development and application of a method for predicting free wake positions and resulting rotor blade airloads. NASA CR 1911 ad CR 1912, 1971.

[40] M. P. Scully. Computation of helicopter wake geometry and it's influence on rotor harmonic loads. ASRL TR 178-1, 1975.

[41] T. R. Quackenbush, D. B. Bliss, and D. A. Wachspress. Computational analysis of hover performance using a new free wake method. 2nd International Conference on Rotorcraft Basic Research, College Park, MD, 1988.

[42] D. A. Wachspress, T. R. Quackenbush, and A. H. Boschitisch. First-principles free-vortex wake analysis for helicopters and tiltrotors. American Helicopter Society 59th Annual Forum , 2003.

[43] G. K. Batchelor. *Introduction to Fluid Dynamics*. Cambridge University Press, Cambridge, UK, 1967.

[44] L. Goldstein. On the vortex theory of screw propellers. *Proceedings of the Royal Society*, 123(792):440–465, 1929.

[45] C. N. H. Lock. The application of goldstein's theory to the practical design of airscrews. British ARC R&M 1377, 1930.

[46] A. J. Landgrebe. An analytical and experimental investigation of helicopter rotor hover performance and wake geometry characteristics. USAAMRDL TR 71-24, 1971.

[47] D. C. Gilmore and I. S. Gartshore. The development of an efficient hovering propeller-rotor performance prediction method. In: AGARD CP-111, 1972.

[48] J. D. Kocurek and L. F. Berkowitz. Velocity coupling: A new concept for hover and axial flow wake analysis and design. In: AGARD CP-334, 1982.

[49] W. Johnson. A comprehensive analytical model of rotorcraft aerodynamics and dynamics, part i: Analystical development. NASA TM 81182, 1980.

[50] A. Ananthan. The role of filament stretching in the free-vortex modeling of rotor wakes. Master's thesis, University of Maryland, 2002.

[51] F. X. Caradonna. The application of cfd to rotary wing problems. *Aerodynamics of Rotorcraft*, pages In: AGARD–R–781, 1990.

[52] A. T. Conlisk. Modern helicopter rotor aerodynamics. *Progress in Aerospace Sciences*, 37:419–476, 2002.

[53] T. S. Kalra, V. K. Lakshminarayan, and J. D. Baeder. Cfd validation of micro hovering rotor in ground effect. American Helicopter Society 66th Annual Forum Proceedings, 2010.

[54] J. Lighthill. A simple fluid-flow model of ground effect on hovering. *Journal of Fluid Mechanics*, 93 (4), 1979.

[55] H. G. Küssner. Helicopter problems. NACA TM 827, 1937.

[56] H. G. Küssner. Untersuchung des bodeneinflusses bei hub- schrauben. AVA-Bericht B.44/J/8, Göttingen, Germany, 1944.

[57] A. Betz. The ground effect on lifting propellers. NACA TM 836, 1937.

[58] M. Knight and R. A. Hefner. Analysis of ground effect on the lifting airscrew. NACA TM 835, 1941.

[59] J. Zbrozek. Ground effect on the lifting rotor. British ARC R & M 2347, 1947.

[60] E. A. Fradenburgh. The helicopter and the ground effect machine. *Journal of the American Helicopter Society*, 5 (4):26–28, 1960.

[61] J. Koo and T. Oka. Experimental study on the ground effect of a model helicopter rotor in hovering. NASA TT F-13938, 1972.

[62] D. E. Bellinger. Experimental investigation of effects of blade section camber and planform taper on rotor hover performance. UARL TR724, 1972.

[63] J. S. Hayden. The effect of the ground on helicopter hovering power required. American Helicopter Society 32nd Annual National V/STOL Forum Proceedings, Washington D.C., 1976.

[64] T. E. Lee, J. G. Leishman, and M. Ramasamy. Fluid dynamics of interacting blade tip vortices with a ground plane. American Helicopter Society 64th Annual Forum Proceedings, 2008.

[65] I. C. Cheeseman and W. E. Bennett. The effect of the ground on a helicopter rotor in forward flight. British ARC R & M 3021, 1955.

[66] D. A. Griffiths and J. G. Leishman. A study of dual-rotor interference and ground effect using a free-vortex wake model. American Helicopter Society 58th Annual Forum Proceedings, 2002.

[67] D. A. Griffiths, S. Ananthan, and J. G. Leishman. Predictions of Rotor Performance in Ground Effect Using a Free-Vortex Wake Model. *Journal of the American Helicopter Society*, 49:302–314, October 2005.

[68] A. Ananthan. *Analysis Of Rotor Wake Aerodynamics During Maneuvering Flight Using a Free-Vortex Wake Methodology*. PhD thesis, University of Maryland, 2006.

[69] V. Khromov and O. Rand. Ground effect modeling for rotary-wing simulation. 26th International Congress of the Aeronautical Sciences, 2008.

[70] T. J. Hawkins. Aerodynamic and power considerations for human powered helicopter in vertical flight. Master's thesis, Stanford University, 1996.

[71] O. Rand. A Phenomenological Modification for Glauert's Classical Induced Velocity Equation. *Journal of the American Helicopter Society*, 51(3), 2006.

[72] L. A. Young. Vortex core size in the rotor near-wake. NASA TM-2003-212275, 2003.

[73] M. J. Bhagwat. *Mathematical Modeling of the Transient Dynamics of Helicopter Rotor Wakes Using a Time-Accurate Free-Vortex Method*. PhD thesis, University of Maryland, 2001.

[74] J. S. Light. Tip vortex geometry of a hovering helicopter rotor in ground effect. American Helicopter Society 45th Annual Forum Proceedings, Boston, MA, 1989.

[75] R. D. Harrington. Full-scale-tunnel investigation of the static-thrust performance of a coaxial helicopter rotor. NACA TN 2318, 1951.

[76] P. D. Talbot, B. E. Tinling, W. A. Decker, and R. T. N. Chen. A mathematical model of a single main rotor helicopter for piloted simulation. NASA TM 84281, 1982.